Static and dynamic haptic feedback using time reversal and electrovibration stimulations

Harald Zophoniasson

NNT : 2017SACLX035

Thèse de doctorat de l'Université Paris-Saclay préparée à l'École Polytechnique

Ecole doctorale n°573
Interfaces : approches interdisciplinaires / fondements, applications et innovation
Spécialité de doctorat : sciences et technologies industrielles

par

M. Harald Zophoniasson

Retour tactile statique et dynamique utilisant le retournement temporel et l'electrovibration

Thèse présentée et soutenue à Palaiseau, le 26 juin 2017.

Composition du Jury :

Mme.	Adriana Tapus	Professeur ENSTA-ParisTech	(Examinatrice)
M.	Medhi Ammi	Maître de conférence, HDR Université Paris-Sud, LIMSI	(Examinateur)
M.	Thomas Sidler	Group Leader EPFL	(Examinateur)
M.	Nazih Mechbal	Maître de conférence, HDR ENSAM	(Rapporteur)
M.	Fernando Vidal-Verdú	Professeur Université de Malaga	(Rapporteur)
M.	Christian Bolzmacher	Ingénieur chercheur CEA LIST, LISA	(Co-encadrant)
M.	Moustapha Hafez	Directeur de recherche CEA LIST, LISA	(Directeur de thèse)

Résumé

Le retour haptique disponible dans les produits grand public est d'un intérêt limité pour les interactions tactiles. Il a été démontré, par exemple, qu'il est moins efficace que l'utilisation d'un clavier physique pour la saisie de texte. La plupart des utilisateurs sont habitués au retour haptique rudimentaire des smartphones. Relativement simple, celui-ci ne peut néanmoins donner que peu d'informations : signaler silencieusement un appel, notifier les messages entrants ou confirmer la frappe de touche sur clavier virtuel. Bien que des améliorations aient été apportées aux technologies haptiques existantes, comme des actionneurs plus performants et des gammes de vibrations plus larges afin de simuler des boutons ou des textures, elles restent limitées à un retour tactile unique. Ceci contrevient à tout usage multi-doigts ou multi-utilisateurs en simultanés.

Ce travail vise à développer un retour tactile statique et dynamique sur grande surface (format A4). Les interactions avec les écrans tactiles nécessitant un retour tactile plus riche et plus performant, deux types de retour complémentaires ont été identifiés afin de les enrichir. Le retournement temporel des ondes de flexions dans les plaques, retour statique, est étudié afin de simuler l'appui sur un bouton et l'électrovibration, retour dynamique, est analysée afin de simuler des textures ou de différencier des zones d'interactions.

L'équation de Kirchhoff décrivant la propagation des ondes acoustiques dans un matériau a permis de développer un modèle analytique de la résolution spatiale du retournement temporel. Des mesures expérimentales sont confrontées au modèle afin de procéder à sa validation. Des règles de conception prenant en compte les spécifications de l'application tactiles envisagée sont élaborées et utilisées pour le développement d'un nouveau prototype avec une électronique améliorée sur une plaque en verre de 1,1 mm d'épaisseur. Différents types de signaux de commande sont étudiés, avec différentes méthodes de quantification (sur un bit ou par modulation sigma-delta) et filtrage ou non des fréquences audibles. La quantification sur un bit avec filtrage des fréquences audibles est l'alternative la plus efficiente en terme d'amplitude de déplacement générée et de réduction des émissions sonores. Des problématiques d'intégration, comme le placement des actionneurs et l'homogénéité de la résolution spatiale et de l'amplitude de déplacement sont analysées. Les appuis parasites de doigts sur la plaque constitue des perturbations pour la propagation des ondes de flexions, que ce soit en terme de diffraction ou d'amortissement. L'effet de la force d'appui du doigt sur l'amplitude de déplacement est donc étudiée. 6% de perte d'amplitude due à une force d'appui du doigt de 2 N sur une localisation autre que le point de focalisation, et jusqu'à 30% pour la même force d'appui sur le

point de focalisation, ont été mesurés.

Le seuil de détection d'une focalisation par retournement temporel mesuré sur 10 utilisateurs à été mesuré à environ 10 μm. Il n'est pas influencé par la force d'appui de l'utilisateur sur l'écran. Bien qu'une unique focalisation démontre la faisabilité du retournement temporel appliqué au retour tactile, elle est jugé brève et non plaisante selon les utilisateurs. Une répétition de focalisations modulées en amplitude offre la possibilité de générer un retour tactile enrichi, comme le clic d'un bouton. Des motifs avec des fréquences de répétition et des enveloppes différentes sont comparés. Il apparaît qu'une fréquence de 200 Hz et une enveloppe en sinus cardinal sont les plus plaisants.

D'un autre côté, l'électrovibration produit des stimuli capables de reproduire une sensation de texture, en modifiant le coefficient de friction entre le doigt et la surface à explorer. Sachant que la force électrostatique générée par l'électrovibration dépend de l'épaisseur de peau du bout du doigt et que les méchanorecepteurs ont des seuils de détection dépendants de la fréquence, une étude utilisateur a été conduite dans le but de déterminer l'influence de la force d'appui sur le seuil de détection d'une stimulation par électrovibration. Les seuils minimaux ont été observés pour une fréquence de 240 Hz. La force d'appui, analysée par ANOVA, semble avoir une influence limitée sur les seuils de détection. De légères différences sont observées dans les seuils de détection pour des fréquences supérieurs à 240 Hz. Il semble que ceux-ci diminuent avec l'augmentation de la force d'appui.

La combinaison des deux approches de stimulations (retournement temporel et électrovibration) sur une même surface offrira un retour tactile riche et multi-point pour des boutons et des textures.

Remerciements

Je voudrais exprimer mes sincères remerciements à mes encadrants, collègues et amis qui ont contribué à l'accomplissement de ce travail.

Tout d'abord je tiens à remercier vivement Moustapha Hafez, pour m'avoir accueilli au Laboratoire des Interfaces Sensorielles et Ambiantes du CEA, d'abord en tant qu'ingénieur, puis en tant que doctorant. Comme Directeur de thèse, il m'a patiemment guidé au cours de ces années de thèse. Je voudrais aussi remercier chaleureusement Christian Bolzmacher, qui a co-encadré mon travail au CEA, pour avoir aiguillé mon travail tout au long de cette thèse, avec beaucoup de disponibilité et d'intérêt.

Je suis très honoré que M. Nazih Mechbal, Maître de conférence HDR à l'ENSAM et M. Fernando Vidal-verdu, Professeur à l'Université de Malaga aient accepté d'être rapporteurs de ma thèse. Je remercie également Adriana Tapus, Professeure à l'ENSTA-ParisTech et M. Medhi Ammi, Maître de conférence HDR à l'Université Paris-Sud, pour avoir accepté de l'examiner.

Je voudrais ensuite remercier mes collègues doctorants du LISA, en particulier Cédric Knibbe et ses moults remarques aiguisées, Valentin Le Guelvouit et Terence Thomas, aux talents pléthoriques, Charles Hudin, pour son support théorique, Sabrina Panëels et Margarita Anastassova, pour m'avoir guidé dans le monde de l'ergonomie et des tests utilisateurs, Alexandre Patarot et Adrien Jaegy, pour leur bonne humeur communicative, Carlos Rossa, Fanny Le Morellec et Tobias Pössinger, pour leurs conseils avisés de thésards, Steven Strachan, pour ses critiques constructives et le restant de l'équipe Florent Souvestre, Gwénaël Changeon, Annick Latare, Gérard Chalubert, Sylvain Bouchigny, Medhi Boukallel et Michel pour la convivialité.

Je suis en outre, extrêmement reconnaissant à Alain Truong, maître d'arts martiaux à l'École Polytechnique, ainsi qu'a toute l'équipe sportive du Lam Son Vo Dao de m'avoir fait découvrir ces enseignements, physiques et mentaux. Merci à Pierre Rizzo et sa soif de convivialité, Rivo Ramodiharilafy et ses encouragements, Thanh Liêm Nguyên et sa profonde gentillesse, Catherine Nguyen et sa bonne humeur communicative, Christophe Gorsy et son talent de comédien, Antigoni Alexandrou, Marine Guémas, Jean-Luc Moncel et Marcel Rheinhart.

Enfin, merci à Inès.

Contents

List of Figures

List of Tables

List of symbols

A	Amplitude of displacement at the focus point
B	Bandwidth of the driving signals
C	Contrast
C_{max}	Maximum achievable contrast
$\hat{C}$	Effective contrast
D	Bending rigidity
E	Mechanical Energy needed to deform the plate
η	thickness of the plate
f_{mean}	Mean frequency of the driving signals
f_{min}	Minimum frequency of the driving signals
f_{max}	Maximum frequency of the driving signals
f_r	Repetition frequency of time reversal
H	Impulse response
h_{aq}	Impulse response between a transducer q and a point a
λ_{mean}	Mean wavelength of the driving signals
λ_{min}	Minimum wavelength of the driving signals
λ_{max}	Maximum wavelength of the driving signals
ν	Poisson's ratio
Q	Transducer's number
q	Transducer's location
R_s	Spatial resolution
ρ	density
ρ_s	area density
S	Area of the plate
T	Reversal time
T_c	Characteristic time
T_r	Repetition time
τ	Attenuation constant of the plate
u	Displacement of a point
v	Velocity of a point
V	Voltage of the driving signals
Y	Young's modulus

Table 1: Symbols.

Chapter 1

Introduction

The huge success of smartphones is a sign of multimodal interfaces' acceptance in our society. Multimodality refers to the usage of different communication channels between a user and a machine. Typing on a physical keyboard is a long used channel and tends to be replaced by tactile input. The visual channel is widely used through screens and other types of visual displays. The co-location of input and display, on a smartphone's touchscreen for example, created a multimodal interaction : typing on a virtual keyboard and getting a visual feedback as to which key was registered. The auditory channel can also be used, and in this particular case, also supplements the interaction with a clicking sound, serving as auditory feedback. Haptics, referring to the sense of touch, is a more recently explored channel. It is promising in terms of controllability, transparency and flexibility for interactions with touchscreen based devices. A vibrating smartphone signalling an incoming call or a pressed key is commonly implemented in nowadays hand-held devices. But haptic interfaces are in fact still relatively constrained to moderately sized devices, such as smartphones and tablets. Multimodality is however rapidly extending to larger interfaces, such as windows or modern interactive blackboards. Haptics, as opposed to visual or auditory feedback, is more complex to integrate. Multimodality is not only supplementing existing ways of interactions with those devices but might also create new interaction paradigms.

Since 2007, smartphones with touchscreen interfaces gained popularity and touch interaction has become the main interaction modality with most mobile devices. Smartphones emerged by dropping the physical keyboard of regular mobile phones and increasing the screen size in addition to enhancing the computing power and adding internet connectivity. A larger screen size improves comfort for viewing videos or Web pages. Touch input allowed the on-demand display of a keyboard, or any suitable form of inputs. Other form of interaction appeared, such as the famous pinch-to-zoom gesture. Although the keyboards used on smartphones look like the original physical keyboards, an important feature is missing: the buttons cannot provide the tactile feedback that physical buttons do when touched or clicked. Without tactile feedback, users rely on audio and visual cues to notice if the device registered the input. Rapidly, tactile feedback was added to touchscreen devices. But the current tactile feedback in commercially available products provides limited tactile feedback and has also been proven to be less efficient than physical keyboards for typing activities [35]. As it is very crude and simple, it can only convey little information: silently signalling a phone call, notification of an incoming message or

acknowledging touch inputs when typing on a virtual keyboard. The challenge is to make one feel as if a button was pressed, even though the interaction surface has not moved, by providing the specific key-click sensation of a physical keyboard. But simulating a key click is not the only possibility of enriching tactile interactions. Simulating different textures could add a new level of interactions to smart devices. For example, the car's radio has been transformed into a feature-rich infotainement device with a touchscreen at its center. For the driver, changing the music's volume while keeping the road in sight is hardly possible with a touchscreen. Therefore, different texture feedback could provide him with some reference points to distinguish different buttons or sliders just by touch. Simulating different textures can find other applications, such as online shopping. The user will not only be able to choose his furniture's colour but also the specific fabric material, directly on his smart device.

Along with the democratisation of touchscreens, devices tend to get larger and larger, which represents a second challenge. Nowadays premium smartphones hardly fit inside the palm of the hand and tablets also increased in size. Laptops and regular desktop screens are getting tactile. Even larger interactive screens are coming to the market, in the form of multimedia tables, blackboards or even shop windows. As the device increases in size, integration of haptic feedback technologies becomes a challenge. Actuators increase in size and number and consume more energy. In order to be practically feasible, the tactile feedback technology should be compatible with a screen without interfering with the transparency of the visual display.

Another need that has emerged with large displays is multitouch interaction. Some interactions require two simultaneous touch inputs, such as the pinch-to-zoom gesture. Other interactions on multimedia table with several users need to be carried out simultaneously. With commercially available haptic transducers, it is impossible to create two different haptic feedbacks on different locations at the same time. If one button is pressed, the whole surface vibrates and every user touching the table will feel the same vibration. Future challenges for haptic feedback are local stimulation and multi-point feedback.

1.1 Scope

This work aims to overcome the current limitations of haptic feedback by tackling the challenges of providing the user with a rich feedback on **large surfaces**. Two types of feedback are identified as necessary to enrich tactile interactions. On the one hand, a **button feedback**, or key-click, is needed to simulate an input acknowledgement. This type of interaction is defined as **static feedback**, as the finger remains static on the surface while clicking. On the other hand, a **texture feedback** is needed to simulate tactile textures or differentiate specific areas of interaction. This type of interaction is defined as **dynamic feedback**, as the finger perceives stimulation only when the finger is moving on the surface. Although advances are made to enrich existing technologies in hand-held devices, such as more capable actuators and broader ranges of vibrations to emulate buttons or textures, they remain limited to a single point feedback, preventing any simultaneous multi-user use-case scenarios. In this work the challenge of **muti-point haptic feedback** is addressed.

Thus, the main challenge faced by haptic feedback is the elaboration of better and richer feedback. This work tackles this challenge by combining static and dynamic

tactile feedback, with a multi-point feedback capability.

1.2 Thesis overview

The thesis is divided into 7 chapters. In this first chapter, the evolution of haptic feedback systems is introduced. The current limitations in terms of interaction are pointed out. The research objectives of this work are then defined.

In chapter 2, existing approaches to generate haptic feedback are presented. The shortcomings and perspectives of state of the art technologies are discussed. It is shown that standalone technologies are unable to address all the haptic challenges mentioned above. In the light of these facts, a study of two complementary technologies is proposed in this thesis and are based on: time reversal and electrovibration.

In chapter 3, theoretical basis of time reversal and design guidelines are presented. The spatial resolution of such a system is a crucial parameter in the design of a tactile feedback interface. An analytical model based on Kirchhoff's equation for wave propagation to compute the spatial resolution of time reversal of flexural waves applied to plates is presented. Measurements on an experimental set-up are then compared to the model's prediction.

In chapter 4, the development of a new time reversal enabled screen with improved driving electronics is presented. The active surface on which time reversal is applied is an A4 format made of 1.1 mm thick glass. The prototype is studied with different driving signals. Parameters such as the amplitude, the temporal and spatial resolution are discussed. Power consumption is then investigated. Lastly the noise emission in the audible frequency range are reported and compared.

In chapter 5, the performance of the prototype in terms of human perception is evaluated. First, the influence of the force with which the user presses on the screen on the generated impact is investigated. Then the relation between applied force and detection threshold is determined. Finally, a perceptual study on different tactile feedback patterns is carried out to compare them in terms of pleasantness and quality of the haptic feedback.

In chapter 6, the electrovibration technology is presented. Theoretical background is reported and optimisation strategies are explored. The effect of varying the applied force on the electrovibration's perception is investigated. An experiment to test the influence of the applied force on tactile perception thresholds for electrovibration stimuli is discussed.

Finally, chapter 7 highlights the major contributions of the thesis. The advances enriching haptic feedback are discussed for the two complimentary studied approaches. Future development perspectives of haptic feedback are proposed.

Chapter 2

State of the art

2.1 Introduction

Historically, haptic feedback has been developed for teleoperation devices. The word "haptics" refers to the capability of sensing an environment through touch. Haptic devices are used in hazardous environment, as handling nuclear material, or surgical tools, to give the surgeon the possibility of finer movements. In either of those cases the hand or the arm of the user is replaced or augmented with robotic parts. While the user gains in force, precision or amplitude of movement, he looses the ability of feeling what the end effector of the robot touches. Two different modalities are covered by haptic feedback: kinesthetic informations and tactile informations. Kinesthesia (or proprioception) is the ability to perceive one's body position, movement and weight. Force feedback can stimulate the kinesthetic sense used, as for example, in steer by wire. In those systems, the steering wheel is mechanically decoupled from the road, which necessitates to recreate through force feedback the drive feeling of a traditional mechanical steering system. Tactile informations concern the surface and material properties that our finger perceives by coming into contact with an object and/or sliding on the surface. Tactile perception includes perception of mechanical properties such as shapes, textures or stiffness through mechanoreceptors, perception of temperature through thermoreceptors and perception of pain through nociceptors. Tactile feedback, is used for example, in a grasping task for a robotic hand where the operator has to detect if the object is sliding out of the hand. Different studies focused on the sense of touch at the skin level, in particular the finger's skin, the fingertip being the end effector of many manipulation and exploration tasks of the hand [30].

In this work the focus is on tactile feedback stimulation. In particular, tactile feedback of buttons and textures on planar surfaces, compatible with visual displays, i.e. transparent. As previously mentioned in chapter 1, haptic stimulation in the form of tactile feedback has been added to smartphones in order to replace the missing sensation of pressing a key. While a key-click feedback is important in order to improve static interactions with a touchscreen, dynamic feedback is of interest to provide a texture feedback. In this chapter, a literature survey on tactile stimulation is presented. This survey does not aim to be exhaustive, but concentrates rather on a few approaches which could tackle the challenge of rich (key-click and/or texture) multi-point tactile feedback on large surfaces.

First section 2.2, aims to provide an understanding of the sense of touch, focusing on the perception of mechanical properties. The different mechanoreceptors embedded in the fingertip's skin are presented. Each one reacts differently to the skin's mechanical deformation and enables to recognise different kind of information, such as pressure or vibrations.

In section 2.3, quasi-static interfaces are presented. This category of interfaces includes Braille displays and out-of-plane pins. They are able to display discrete graphical information or contours. Other quasi-static interfaces include deformable surfaces that are able to display continuous shapes to the user.

In section 2.4, dynamic interfaces are presented. They can either apply a lateral force on the finger, stimulate it in the vibrotactile sensitivity range or even control the friction between the finger and the surface. Electrocutaneous interfaces are also considered to be part of this category.

In section 2.5, hybrid interfaces, which aim to combine several technologies in

order to display haptic feedback with enhanced performance, are presented.

Finally, in section 2.6 a summary and discussion of the advantages and drawbacks of each family is proposed.

2.2 The sense of touch

2.2.1 Mechanoreceptors

Tactile perception of mechanical properties of objects relies on four types of sensors, called mechanoreceptors, located in the glabrous skin of the fingerpad, as shown in Figure 2.1. Their role is to transform the mechanical deformations of the fingerpad into electrical impulses directed to the brain. Researchers discovered the individual roles of each receptors and how they react to the mechanical stimuli. The four types of mechanoreceptors are : the Meissner corpuscles, the Merkel cells, the Ruffini endings and the Pacinian corpuscles. These receptors are classified according to their adaptation capability to a stimulus (FA for Fast Adaptating, SA for Slow Adaptating) and to their sensitivity area (type I for small sensitivity area, type II for wide sensitivity area).

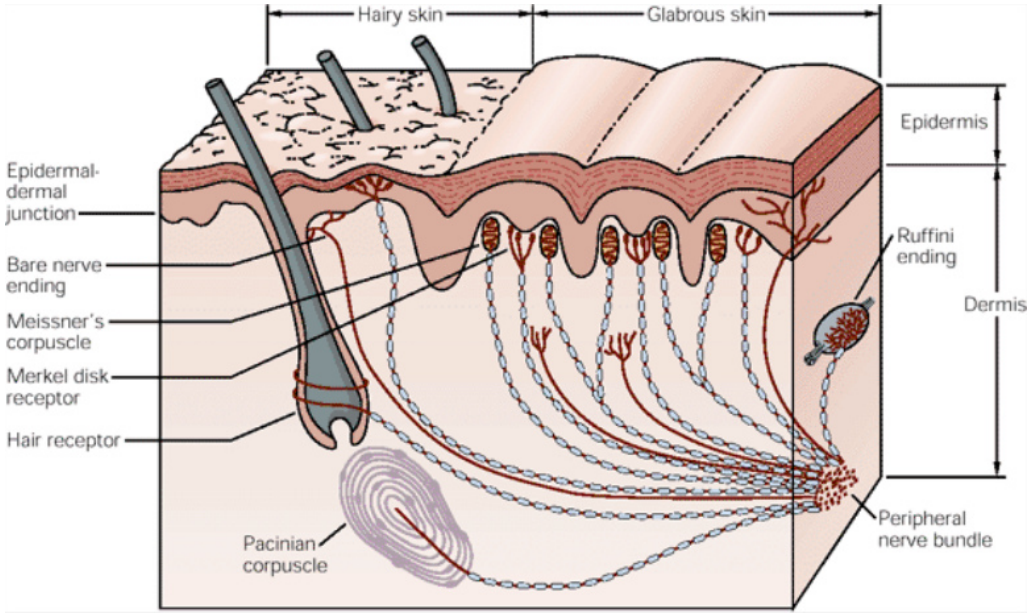

Figure 2.1: The location and morphology of mechanoreceptors in hairy and hairless (glabrous) skin of the human hand. Receptors are located in the superficial skin, at the junction of the dermis and epidermis, and more deeply in the dermis and subcutaneous tissue. The receptors of the glabrous skin are Meissner's corpuscles and Merkel disk receptors. The receptors of the hairy skin are hair receptors, Merkel disk receptors (slightly different from their counterparts in the glabrous skin), and bare nerve endings. Subcutaneous receptors, beneath both glabrous and hairy skin, include Pacinian corpuscles and Ruffini endings, from [25].

The Meissner corpuscles are located at the dermis and epidermis junction. They are the most numerous with a density of more than 100 corpuscles per square centimetre on the fingerpad. They are said to be Rapid Adapting (RA), meaning that

the electrical impulse generated by those corpuscles decays rapidly during a continuous mechanical stimulation. Their covered sensitivity area is small, between 3 mm and 5 mm, and are therefore classified as type I. Due to their small sensitivity area, they give a relatively precise location information concerning the sensed stimulus. Their fast adaptiveness makes them insensitive to very low frequencies of a few Hertz. One identified interpretation of those signals is the perception of vibrations generated by a sliding object, enabling grip pressure adjustment [47].

The Merkel disks are located at the same depth inside the finger's skin. Similarly to the Meissner corpuscles, they have a small sensitivity area and therefore are classified as type I. Their density is around 50 cells per square centimetre. They are however Slow Adapting (SA), which means that they fire electrical impulses as long as the mechanical stimulation is present. Those cells perceive low frequencies (0 to 3 Hz), which allows them to respond to pressure, coarse textures and shapes generating spatial variation of the contact pressure [46].

The Ruffini endings are located much deeper in the dermis and have the lowest density, with 10 endings per square centimetre. Slow Adapting (SA), they have a larger sensitivity area than the previously mentioned mechanoreceptors (type II). An identified role in the sense of touch is the detection of lateral stretch of the skin when grasping an object or sliding the finger along a surface.

The Pacinian corpuscles are located in the deep dermis at a density of 30 corpuscles per square centimetre. They have a large sensitivity area (type II) and are Rapid Adapting (RA). Their stimulus frequency response range goes from 50 Hz to 500 Hz and qualifies them as the principal receptor for vibration sensing. As a consequence of its very large sensitivity area, the perception of vibration is rather diffuse and not sharply localised [26].

The characteristics of the four mechanoreceptors are presented in Table 2.1.

	Merkel discs	Ruffini endings	Meissner corpuscles	Pacinian corpuscles
Property	SA Type I	SA Type II	RA Type I	RA Type II
Sensation	Pressure	Stretch	Vibration	Vibration
Frequency (Hz)	0-3	200-300	20-50	50-500
Sensitivity area	Small	Large	Small	Large
Adaptation	Slow	Slow	Rapid	Rapid

Table 2.1: Mechanoreceptors' characteristics, from [25].

2.2.2 Shape versus texture

The different mechanoreceptors involved in the sense of touch being known, there are still unknown mechanisms linking the response of the mechanoreceptors and the construction of a particular tactile sensation in the brain. Several works focus on the perception of texture, trying to determine the relation between the mechanoreceptors responses and the explored surface characteristics [45], [37], [36]. The duplex theory [37] proposes that beneath a certain roughness, textures are perceived by vibrations whereas above a certain roughness, indentation of the fingertip takes over. This threshold is most likely somewhere between 30 µm and 200 µm. This would mean that in order to reproduce textures of a spatial resolution under this threshold, an

induced vibration in the finger would be able to fulfil this task. However, if textures of lower spatial resolution are targeted, this would require a physical indentation of the finger.

2.3 Quasi-static interfaces

2.3.1 Pin-array interfaces

Braille displays are the most known devices in this category. Small stamped points are felt by the finger while exploring the display surface. Transposing a static Braille book to a refreshable Braille display (see Figure 2.2a) required the design of pin-array interfaces. To replicate a Braille character, small pins arranged in a rectangular fashion (2 x 4 = 8 pins, 2.54 mm distance between pins, see Figure 2.2b), repeated one or more times to display one or more characters at once, are moved vertically by piezoelectric actuators. Piezoelectric actuators use the reverse piezoelectric effect, which is the internal generation of a mechanical strain from an applied electric field, resulting in small changes in dimensions of the piezoelectric material. A piezoelectric actuator in a bender configuration is used in Braille cells, as shown in Figure 2.2c. The piezoelectric material bends when an electrical field is applied and raises the pin. Those systems tend to be rather bulky, expensive and incompatible with the transparency requirement of a touchscreen display.

(a) A Braille display, from [42].

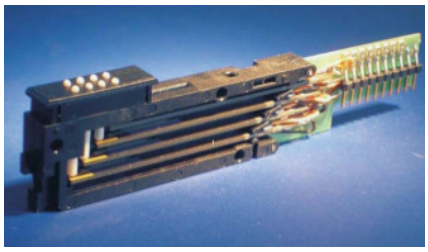

(b) A piezoelectrically actuated Braille cell.

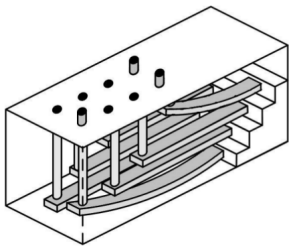

(c) Piezoelectric bender raising a pin.

Figure 2.2: Braille display, based on piezoelectric actuation.

To display more complex informations such as 2D graphical informations to the finger, arrays of greater pin number were developed, using piezoelectric, electromagnetic [24], shape memory alloy [6], thermopneumatic [81] actuation or motors [82]. [78] presents an 8 by 8 pin array display using Shape Memory Alloys (SMA) as the actuation technology (2.54 mm pitch), shown in Figure 2.3a. The actuator is 1.5 mm in diameter and consists of an antagonist pair of SMA springs to raise or

retract the pin at 1.5 Hz. When an SMA spring is electrically heated, its material changes phase from martensite to austenite and recovers its compressed memorised shape which actuates the pin (see Figure 2.3b. While this is a good alternative to piezoelectric actuation in Braille display, SMA has a slow reaction time as it is a thermomechanical actuation and cannot be transparently overlayed on a screen. Displaying complex graphical patterns is also limited by the low resolution, here 64 pins.

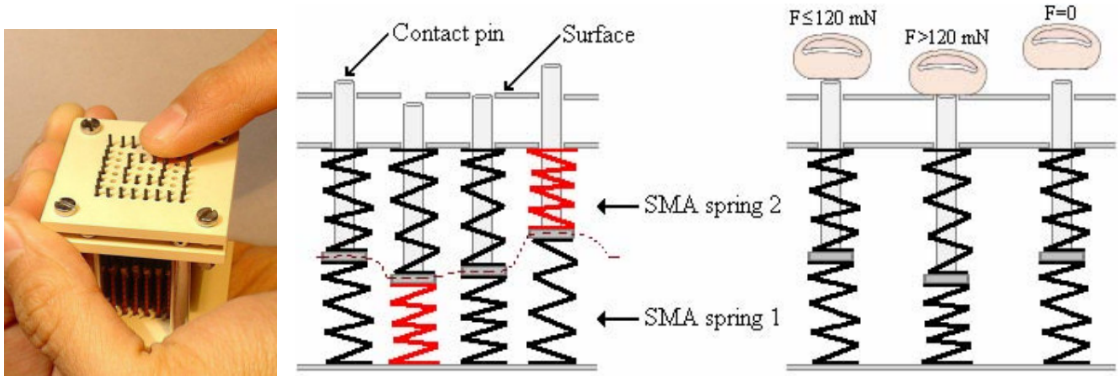

(a) Tactile display. (b) SMA actuators with an antagonistic spring design.

Figure 2.3: SMA-based tactile display, from [78].

Those types of displays have the great advantage of being capable to deform locally the fingerpad. This allows presentation of any 2D shape on the screen, either buttons or contours of specific areas of interaction.

A tactile interface with a higher resolution (30 by 30 pins) is proposed by [22]. The pins have large vertical strokes (100 mm) and are actuated with conventional motors (see Figure 2.4a). However the distance between two pins is large ($\approx$ 3.175 mm). The system is capable of interaction with heavier objects than a finger such as a ball, as shown in Figure 2.4b.

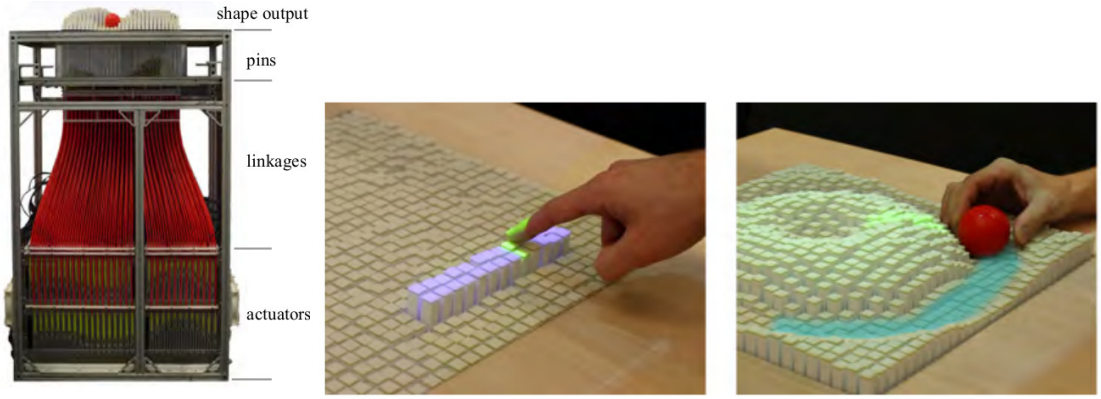

(a) InForm interface. (b) The shape display.

Figure 2.4: InForm interface, with 900 motorised white polystyrene pins, from [22].

Quasi-static interfaces are, by design, capable of multi-point feedback. Integration is however challenging. In terms of pin number and density, it is not possible to integrate such systems in a touchscreen device. Furthermore, transparency is

unlikely to be reached. The only possibility of superimposing visual information is a top-down projection, which is impractical for hand-held devices. Another drawback is the limited number of pins which limits the scope of their applications.

2.3.2 Deformable surfaces

Previous research focused on modifying the geometry of a screen to create different shapes or even physical buttons [76],[33],[73]. The deformable surface is made of a flexible material, such as rubber, which can be transparent. Different actuation methods have been experimented. In the case of Tactus [76], a deformable layer is superposed on a touchscreen, with small areas able to pop up to mimic buttons on the key locations, as shown in Figure 2.5. Fluid is pumped to inflate and deflate those areas on demand. By controlling the amount of fluid pumped, the buttons stiffness can be dynamically adjusted. Users can feel the buttons and press them.

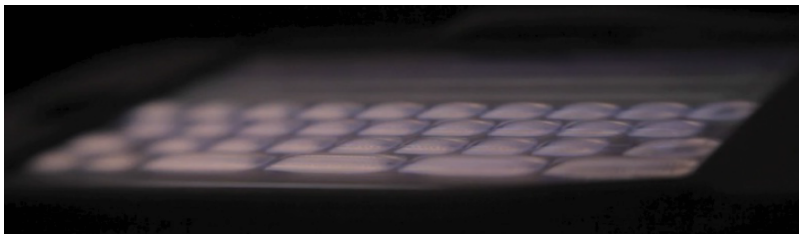

Figure 2.5: Inflatable keyboard overlay, from [76].

These interfaces are rather similar to pin arrays, as they are composed of a matrix of actuators. However, they can offer a continuous out-of-plane tactile information rather than the discrete tactile information provided by the pins. The integration in current touchscreen devices is potentially compatible on the long-term. However, this concept has some limitations. The buttons are not individually controlled. The tactile inflatable layer is not reconfigurable due to the predefined button pattern.

Other prototypes used pneumatic actuation, as in [33]. [73] added the ability of individually controlling the cells arranged in an hexagonal layout (2.54 cm distance between cells). The approach is more reconfigurable than the previous concept, at the expense of more actuation complexity (see Figure 2.6).

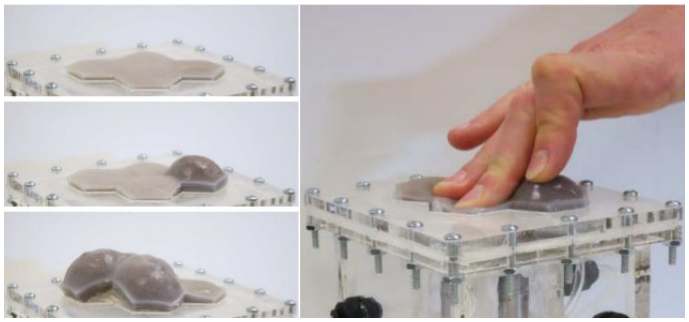

Figure 2.6: Haptic array prototype with four hexagonal cells, from [73].

While air or liquid are obvious choices, other fluids with specific characteristics can be used. [44] uses a magneto-rheological (MR) fluid and an array of 12 by 7 electromagnets on a 10” format (see Figure 2.7). MR fluid is composed of small

ferromagnetic micro particles. When a magnetic field is applied, the particles align and create chains along the magnetic field lines. This effect generates an apparent viscosity change which allows rendering different stiffnesses under the fingertip. High frequency vibrations (up to 600 Hz) attract the user's attention or quick on-off transitions, replicating a key-click. [77] uses the same architecture, but based on electro-rheological (ER) fluids. In this case, the magnetic field is replaced by the application of a high electric field.

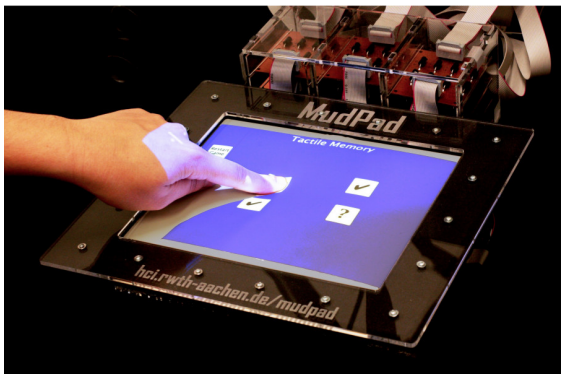

(a) Interface, with top-down visual projection

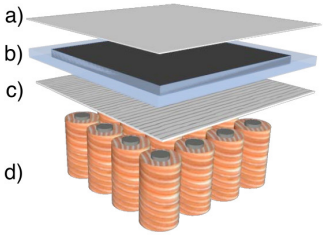

(b) Exploded view of system design: a) latex touch and projection surface, b) MR fluid pouch, c) resistive touch input pad, d) array of electromagnets.

Figure 2.7: MudPad interface, from [44].

The possibility of embedding a 3 by 3 Electro-Active Polymer (EAP) actuator array underneath a flexible display is explored in [57] (see Figure 2.8b). EAP are polymers that exhibit a change in size or shape when an electric field is applied. Two types exists: in the dielectric type, the actuation is caused by electrostatic forces between two electrodes which squeezes the polymer, whereas in the ionic type, actuation is caused by the displacement of ions inside the polymer. Here, the EAP cells are of the dielectric type and are designed to extend perpendicularly to the surface, deforming the display layer, as seen in Figure 2.8a. The cells interdistance is 10 mm.

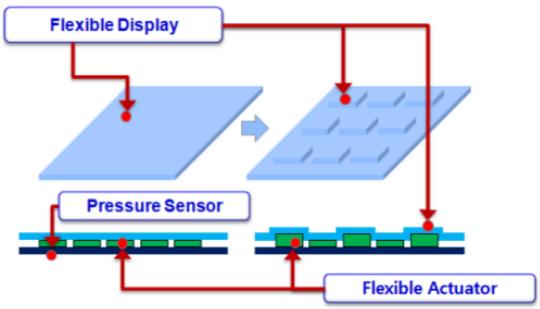

(a) EAP based actuator matrix.

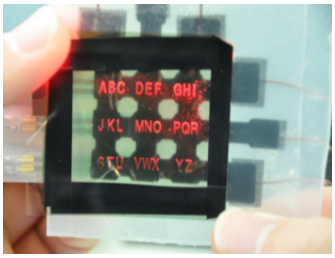

(b) Integrated Visio-Haptic Display Module.

Figure 2.8: EAP based actuator matrix, from [57].

While providing a shape changing surface and therefore, a button-type feedback, those types of interfaces are facing the same limitations as pin arrays. Most of the actuation principles cannot be easily integrated on a hand-held touchscreen

device.When a fluid is used, encapsulation is an issue to be accurately addressed. In the previous designs, the lowest achieved resolution is 10 mm.

As a response to those limitations, dynamic feedback interfaces have been proposed to try to overcome some of the limitations of quasi-static interfaces.

2.4 Dynamic interfaces

2.4.1 Lateral motion

Lateral skin deformation has been explored by different research teams. When sliding a finger across a bump, a force is opposed to the finger's movement with the force's direction and magnitude related to the bump's slope (see Figure 2.9b), [70] introduced a haptic feedback interface (see Figure 2.9a reproducing the force cues of a bump or hole while exploring a flat surface, as shown in Figure 2.9c. This haptic illusion enabled users to feel a bump or a hole on a flat interaction surface, and therefore would allow rendering of 3D features on a flat surface. This principle was adapted in several papers to tactile screens [71], [88].

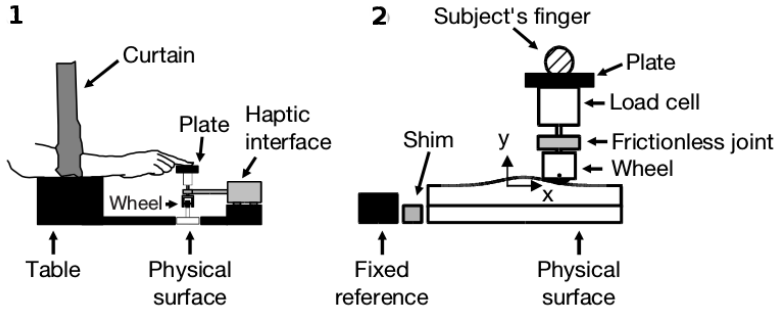

(a) Side (1) and front (2) views of the apparatus. Subjects pressed down on the interface's plate and roll it sideways (x-axis in 2) to explore the shape of an interchangeable physical surface.

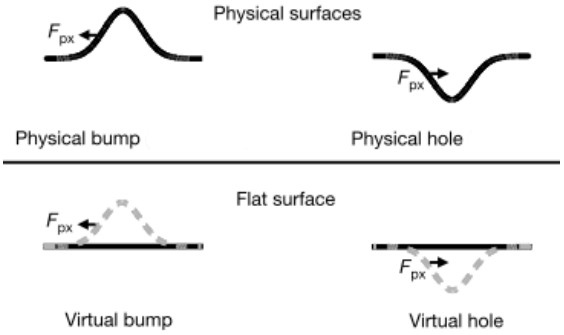

(b) Physical and virtual bumps and holes.

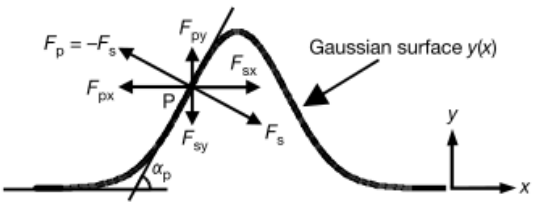

(c) Forces exerted by a bump on a finger.

Figure 2.9: While subjects explored a flat surface, the haptic interface provided forces cues (in dashed lines) equivalent to F_{px}, the horizontal component of the force exerted on the finger by moving across a physical bump or hole (in plain lines), from [70].

A display based on lateral force feedback and direction controlled mechanical vibrations is introduced in [71]. The lateral force feedback is generated through

a set of cables linked to a manipulation tool. Here, to explore the surface, the user applies its finger on a small pad, which is linked through four cables to four motors located on the corners of the screen, as shown in Figure 2.10. By controlling the motors, lateral force can be applied to the pad. The device is able to brake or accelerate the finger in any direction. [71] presents a method to display both macrogeometric (shapes) and microgeometric (texture) information based on lateral force and direction-controlled mechanical vibration (around 0-400 Hz).

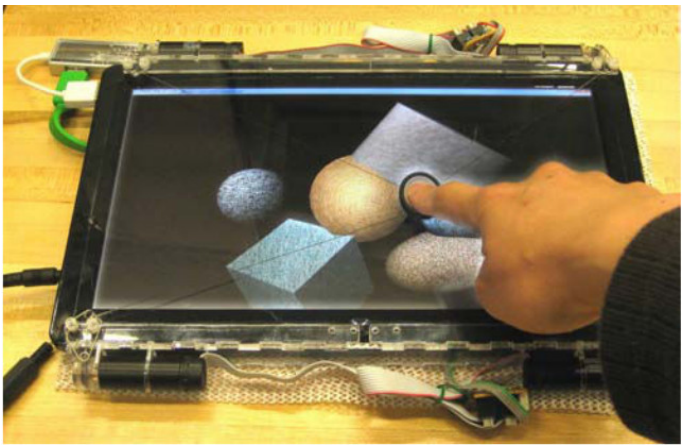

Figure 2.10: Lateral force feedback display for rendering haptic texture and geometry, from [71].

A set-up similar to [71] is presented in [88] with two thimbles allowing interaction with two fingers. This enables 3-DOF manipulation force feedback (two in-plane translation and a torque), as shown in Figure 2.11. The device allows the user to feel grasping forces and the torque of a virtual wrench.

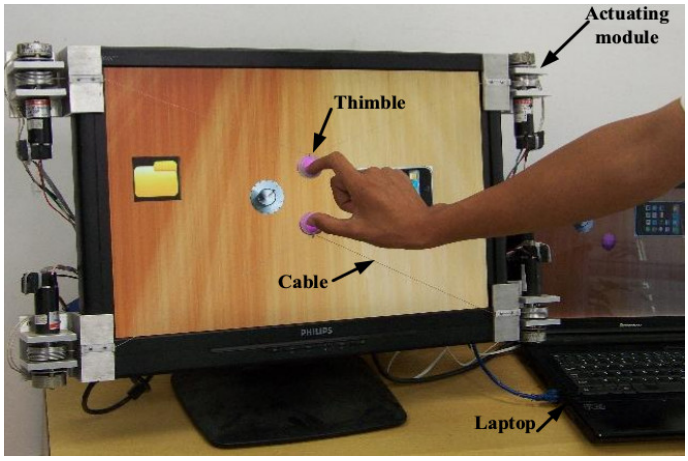

Figure 2.11: The FingViewer touch screen, from [88].

The proposed approach can apply high forces to the fingers which provides a rich user experience in haptic interaction. However, due to the size of the motors and to partial occlusion of the screen, the system cannot be integrated on mobile touchscreen devices.

2.4.2 Vibrotactile interfaces

As mentioned in subsection 2.2.1, Pacinian corpuscles' sensitivity to vibrations lie between 50 and 500 Hz with peak sensitivity at around 250 Hz [75]. Most handheld devices use this frequency range to silently inform users of calls, to notify and enhance visual and audio feedback on tactile keyboards. The vibration is transmitted to the whole device, thus generating a "global feedback". As opposed to this approach, the use of specific technologies such as time reversal allows to localise vibrations on a specific part of the interactive surface. This opened the possibility of multi-point haptic feedback and will be referred as "localised vibrations".

Global vibrations

The common way to generate haptic feedback is relying on the use of cost-effective, compact rotating motors with an eccentric mass. It is an easy way to produce vibrations inside a device. Because of the direct link between the rotation frequency and the input voltage, the quality of the generated feedback by such motors is rather poor and limited. In addition, the reaction time is low (tens of milliseconds), which generates a delay during the interaction.

Several technologies, such as electromagnetic actuators, voice-coils, and piezoelectric [67] actuators increase the controllability of the perceived vibrations. This greatly improves the key-click feedback, making it more realistic. Moreover, it is also possible to simulate simple textures with those actuators.

Figure 2.12: The TouchEngine, a 0.5 mm thick piezoelectric bender actuator, from [67].

The study of specific patterns in order to design and evaluate the most identifiable key-click signals for mobile devices is proposed in [11]. Different frequencies, amplitudes and repetition cycle are tested to identify the best haptically perceived signals.

Other experiments try to replicate force-displacement behaviour of real buttons with a haptic illusion based only on vibrations. A virtual button-type haptic feedback device built with a low-cost electromagnetic actuator and a pressure sensor is presented in [55], (see Figure 2.13a). The proposed method aims to provide haptic feedback, not only for key-clicks but also for the movement of the key before and after transition points in a force-displacement curve, with specific vibration patterns, as shown in Figure 2.13b. A user study concluded that six different virtual buttons were discriminated at a rate of 94.1%, and that the association of four virtual buttons with their physical counterparts was successful at a rate of 79.2%, showing that the resultant haptic feedback is realistic and distinctive.

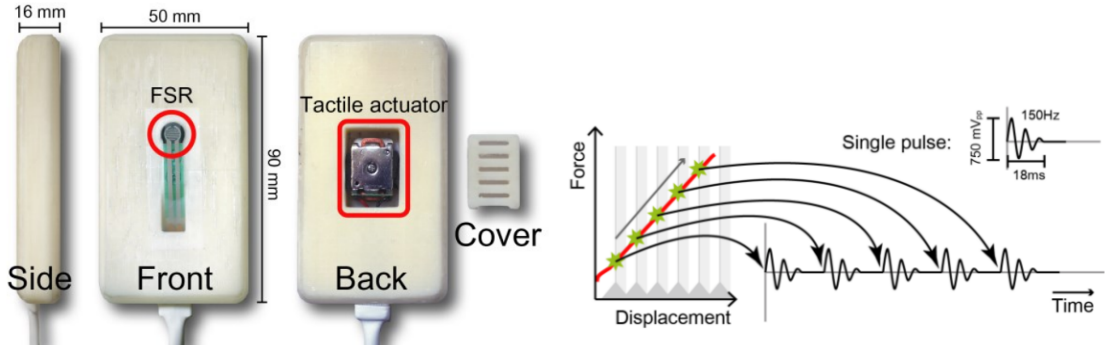

(a) Virtual button feedback device. (b) Force-displacement behaviour illusion.

Figure 2.13: Virtual buttons based on a vibrotactile haptic illusion, from [55].

By laterally vibrating the contact surface with the fingertip at a frequency within the vibrotactile frequency range ($50 - 500$ Hz), it is possible to simulate a texture. The set-up in [83] is able to measure the force of interaction while a finger explores a texture and replay it (see Figure 2.14). The samples were placed on the tray A. The finger D position was measured by a linear variable differential transformer sensor attached to the fingernail. The interaction forces induce flexural deformations of the leaf springs H along x and in the piezoelectric bender B (500 Hz bandwidth). The position of the finger, the net force, and the tangential force are measured by the transducer (see Figure 2.14a), giving a texture spectrogram, as shown in Figure 2.15 (spectrogram of a triangular grating of a 1 mm spatial period). The transducer is guided by a linear bearing E which is located by an encoder F. The fingertip rests on the tray A and the transducer tracked the position of the finger D resting in a cradle G, thus relieving the fingertip from lateral loads. As the slider moves with the finger, the transducer stimulated the fingertip, as shown in Figure 2.14b. The device was used to record and reproduce 5 different texture samples. 3 out of 5 real samples were presented to users, who had to identify and match them either with real comparison textures or with simulated ones. The success rate for simulated textures was high (75 %) but not as high as for comparison to real textures (93 %).

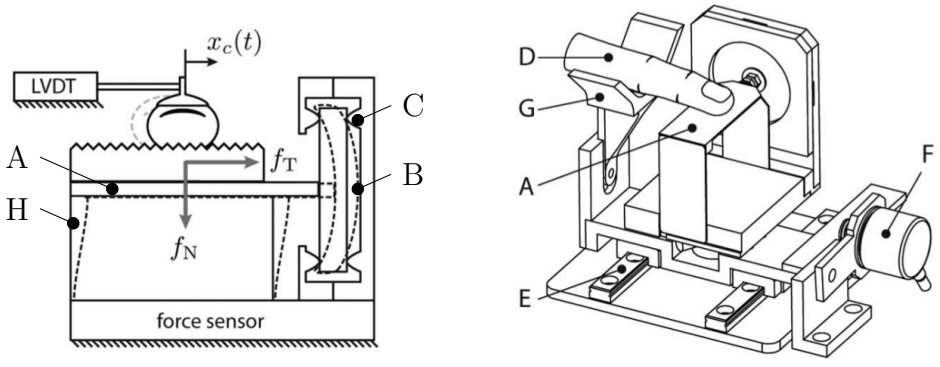

(a) Texture sensing. (b) Texture reproduction.

Figure 2.14: Lateral force stimulator. A) tray, B) piezoelectric bender, C) clamp, D) finger, E) linear bearing, F) encoder, G) cradle, H) leaf springs, from [83].

In this section a few illustrative examples of how to use a single large bandwidth actuator to display rich tactile informations are presented. It is possible to simulate

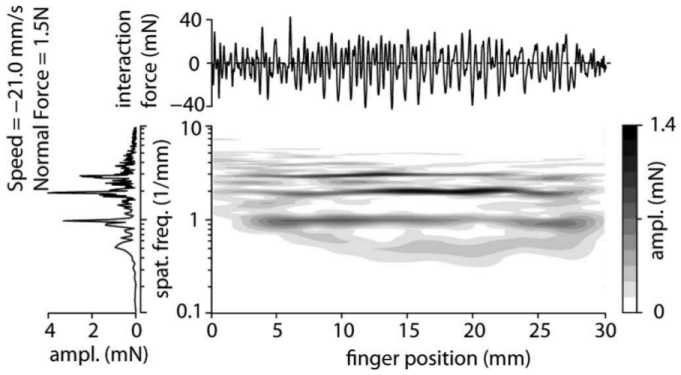

Figure 2.15: Spatial spectrogram of a texture, from [83].

key-clicks and to reproduce different surface roughnesses with only vibrations. However, a single actuator as used in the previous concepts will not be able to provide a multi-point feedback.

Localised vibrations

One way to achieve localised vibrations is to develop array designs of micro-actuators with high dynamics. VITAL, the interface proposed in [4], is a matrix of 8 by 8 electromagnetic actuators (5 mm inter-distance) able to produce up to 100 µm displacement from DC to 800 Hz, as shown in Figure 2.16. The amplitude and frequency of each actuator is independent, which enables to display dynamic patterns. One limitation of this design is spatial resolution that cannot go beyond a certain limit due to the crosstalk between the micro-actuators' magnetic field.

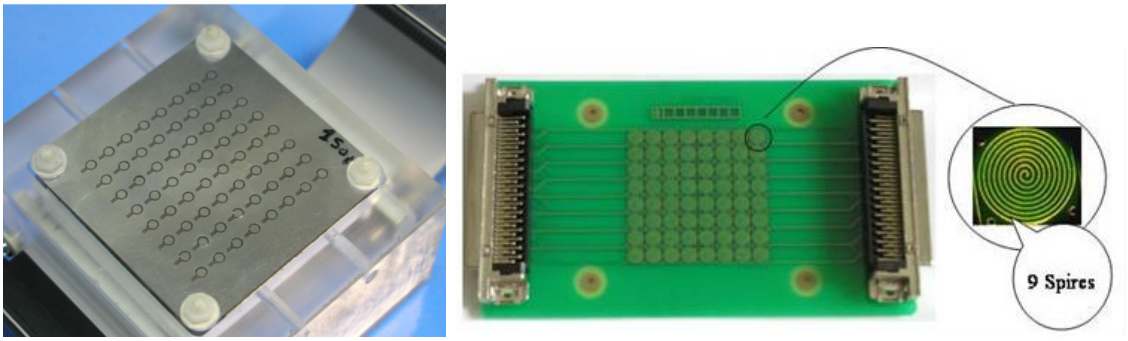

(a) The tactile display. (b) The pcb layer and the micro-coil actuators.

Figure 2.16: VITAL, an 8 by 8 vibrotactile display with an integrated laser-cut flexible membrane, from [4].

Lateral vibrations can also be localised with a 10 by 10 arrangement of piezoelectric benders [66] (see Figure 2.17a). The actuators' inter-distance is 1 mm, as shown in Figure 2.17b. The interaction is referred to as lateral skin stretch. A pair of adjacent actuators is activated to cause successive stretch and compression of a patch of skin. A progressive wave is created by time-overlapping strain changes in successive neighbouring patches. Most subjects described the pattern as one small raised dot sliding under the fingertip.

Integration of in-plane and out-of-plane localised vibrotactile feedback approaches in handheld devices is challenging due to their non transparent nature. This led to

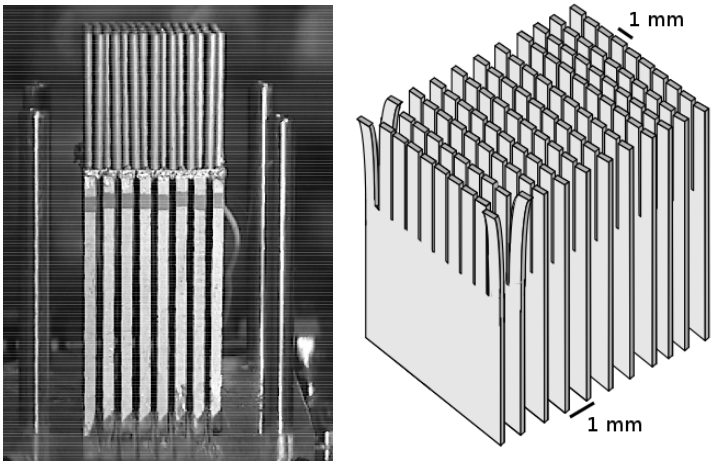

(a) The tactile display. (b) The piezoelectric combs.

Figure 2.17: STReSS device with piezoelectric benders, from [66].

the introduction of additive interference, which is an interesting approach to generate localised vibrotactile feedback. It consists of generating acoustic waves emitted from different positions on a given surface. The different impulses are synchronised, which allows the vibration flow to add up at a specific point of the surface. In [53] a simple device demonstrating the concept is presented. It is based on two rotating motors with an eccentric mass. Each motor generates a vibrotactile wave, that is below the detection threshold. Then the two waves interfere, their amplitudes are summed up and exceed the detection threshold of the finger (see Figure 2.18). To control the interference's location, the waves are generated with a time difference between both actuators. If the time difference is null, the interference is located at a position equidistant from both actuators.

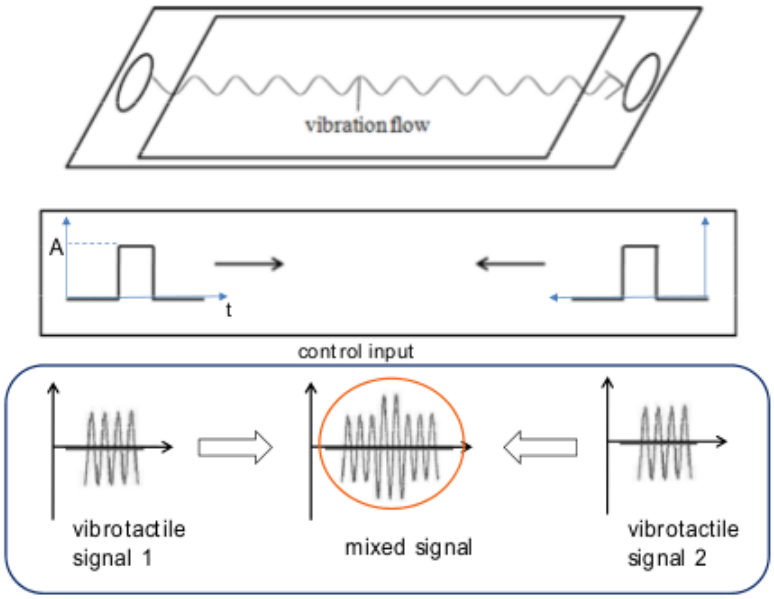

Figure 2.18: Additive interference relying on the synchronisation of two vibrotactile signals emitted by two distinct actuators, from [53].

Based on this first introduction of acoustic waves to produce additive interference, a novel approach, called Time Reversal, has been developed to improve the localisation of tactile feedback. Time reversal of flexural waves has been previously implemented on thin plates in [40], to address the multi-point feedback challenge. The process relies on focusing flexural waves in a solid material. It generates a constructive interference of flexural waves produced by actuators located on the borders of the surface, as presented in Figure 2.19. As this approach can take into account the reverberation of flexural waves, it is possible to generate a local vibration with just one transducer. However, the use of several transducers improves the total amplitude of the produced vibration. With 8 piezoelectric actuators driven at 30 V, a displacement amplitude of 10 µm can be generated. Due to a very short duration of the focalisation, the sensitivity threshold to detect a single focalisation was found to be between 10 and 15 µm of displacement's amplitude and the resolution (minimal distance between two vibration peaks) was found to be 10 mm. The required duration of focalisation varies from 2 to 5 ms [38]. This allows to repeat the focalisation at a frequency of 200 to 500 Hz which can be easily perceived by the finger. When a transparent material, such as glass or PMMA, is used as a plate in which acoustic waves are propagated, the integration of a visual display becomes possible. The principle is also compatible with simultaneous multiple local vibrations.

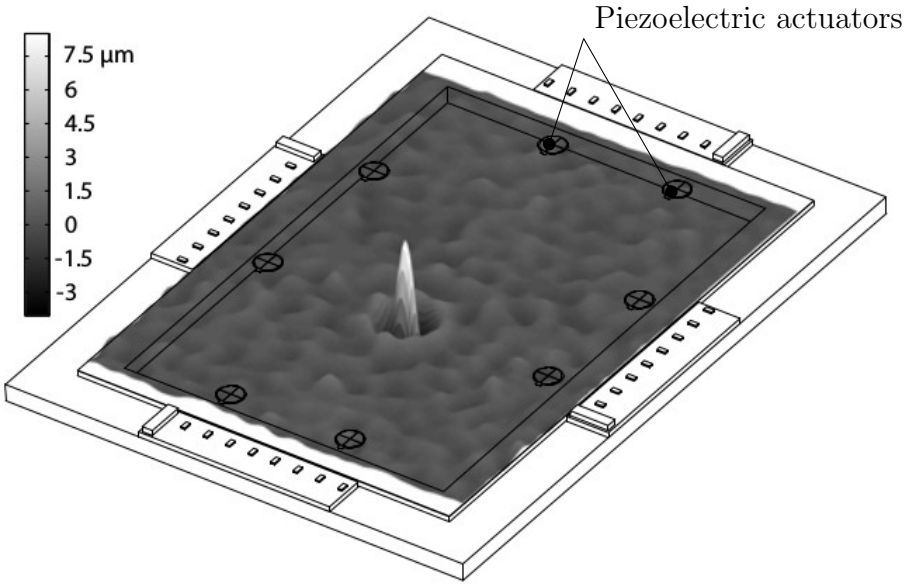

Figure 2.19: Localised normal displacement generated through time reversal. Displacement measured at focus instant (out-of-plane displacement scaled up for clarity), from [39].

2.4.3 Variable Friction

Another concept relies on varying friction coefficient between the finger and the explored surface. The user is able to perceive different surface roughnesses. Three different approaches can achieve variable friction: surface acoustic waves (SAWs), squeeze film and electrovibration. The first two rely on mechanical vibrations whereas the third one uses the attractive effect of electrostatic forces.

Surface Acoustic Waves (SAWs)

The device in [56] is composed of a glass substrate and two Inter Digital Transducers (IDTs) formed on a piezoelectric substrate (see Figure 2.20). The IDTs generate a vibration, which is transmitted to the vibrating plate through a coupling material. Both IDTs generate progressive waves, which are combined in a standing wave on the vibrating plate (see Figure 2.20a). An intermediate stiff object (an aluminium slider) is required to feel the effect in the finger (see Figure 2.20b). The standing wave reduces the friction between the slider and the plate. Friction coefficient is reduced from 0.2 to 0.1 with a standing wave's amplitude of 12 nm. The use of an intermediate part essential to feel the tactile effect limits however the scope of industrial applications for touchscreens.

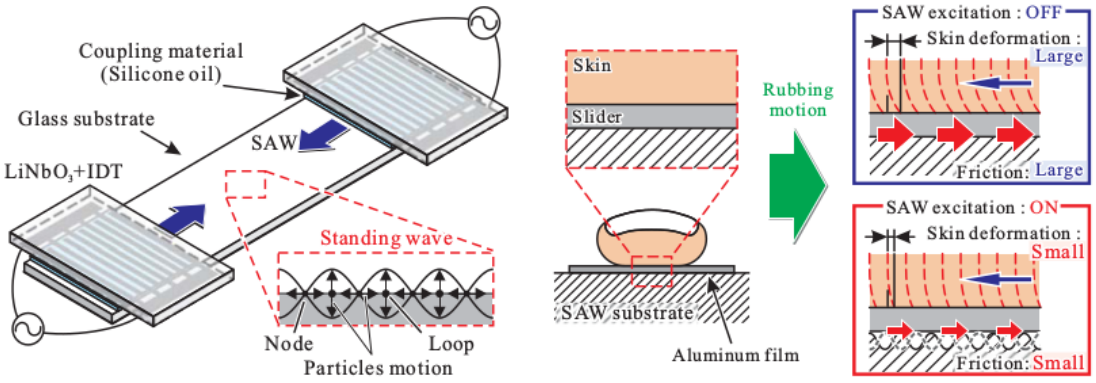

(a) Glass substrate and IDT transducers. (b) Friction shift by switching SAWs.

Figure 2.20: Variable friction interface with SAWs, from [56].

Squeeze film

While the previous device relies on vibration amplitudes in the nanometer range and an intermediate object, the squeeze film effect is able to display tactile textures directly to the fingertip through vibration amplitudes in the micrometer range. Squeeze film devices provide a constant stimulation all over the touched surface which is vibrating at a single specific frequency above 20 kHz and an amplitude above 1 µm. The high frequency vibrations induce an effect similar to air lubrication. A thin film of air is "squeezed" between the surface and the finger, as shown in Figure 2.21. The friction reduction can be explained using the squeeze film air bearing theory, which is detailed in [84].

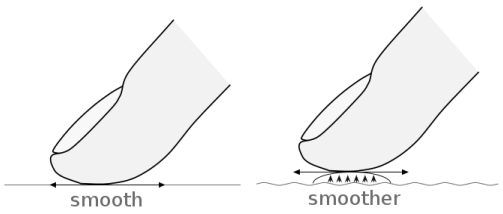

Figure 2.21: The squeeze film effect: controlled vibration of a surface creates an air film which reduces its friction coefficient, from [9].

The first studies on variable friction devices were carried out in 2007 [85]. The set-up consists of a ⌀25 mm circular glass plate glued on a piezoelectric ceramic disk of the same diameter. The piezoelectric actuator is driven at a resonant frequency of 33 kHz. At 40 V_{pp}, the friction coefficient is approximately reduced ten times. A sine wave pattern (spatial period of 1 cm) was generated on the plate and users were asked to describe the sensation perceived as they moved their finger across the plate. They described the sensation as "smooth bumps".

Another variable friction device is proposed in [60], using a piezoelectric disk (⌀16 mm) glued on the back of a glass plate of greater dimension (3 by 3 inches, see Figure 2.22a). It appears that the friction reduction is not uniform all over the surface. The friction does not drop on the nodal lines, which are depicted in Figure 2.22b for two different resonant frequencies. An attempt to overcome uneven friction reduction is to use different resonant frequencies according to the finger's position.

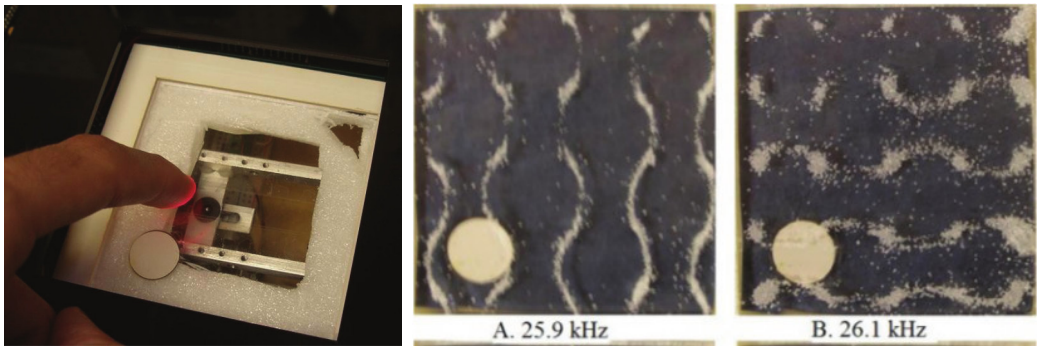

(a) Variable friction glass plate and piezoelectric transducer.

(b) Visualising nodal lines at different resonant frequencies with salt.

Figure 2.22: Variable friction tactile display, from [60].

An improved version of the device is presented in [58]. The piezoelectric actuated glass surface vibrates at 26 kHz which reduces the friction coefficient of the surface from 1.0 to 0.15. The surface lies on top of an LCD screen, as shown in Figure 2.23a. A 57 by 76 mm touchscreen is created with laser based measurement of finger position (see Figure 2.23b). In a study, participants were asked to slide their finger from a starting point to a target point. Friction was variable across the surface and high over the target. With friction reduced across the surface, it increased users' confidence in moving towards the target, allowing them to approach more quickly without compromising ability to stop abruptly on the target and select it accurately.

One of the latest versions of a device called STIMTAC is presented in [28]. It embeds an LCD screen to display different textures (see Figure 2.24). Guidelines are provided for an efficient squeeze film effect. A flexural vibration mode with a wavelength equal to twice the fingertip's width should be used, with a peak to peak vibration amplitude of at least 1 µm and a resonance frequency above 25 kHz. A flexural vibration mode at 31.2 kHz is selected for the presented device and two piezoelectric actuators are glued at the two opposite sides of the plate. Their width is designed in order to have the same resonant frequency as the glass plate. In order to easily detect the tactile display patterns, a vibration's amplitude of 1.6 µm, corresponding to an actuation voltage of 150 V is required.

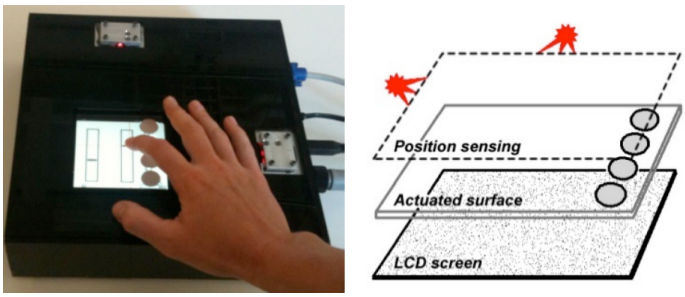

(a) (b)

Figure 2.23: a) Picture and b) structure of the variable friction device, from [60].

Figure 2.24: STIMTAC device, from [28].

The STIMTAC device has been used to simulate different fabrics such as velvet [8]. The friction modulation control signal is qualitatively designed from velvet's characteristics identified by a tribological study. Four tribological features were determined as characteristics to simulate: the friction coefficients in the sliding directions with and against the pile (higher when sliding against the pile than sliding along the pile main direction), the transient behaviour corresponding to the change of sliding direction from along to against the pile and a fiber tuft frequency of variation of the friction coefficient (see Figure 2.25). The influence of each tribological feature on the tactile rendering is studied via psychophysical studies comparing real and simulated fabrics. The results show the friction coefficient must vary in accordance with the sliding direction, and also the high variation frequency of the friction coefficient, simulating the fiber tuft frequency, is important for the tactile illusion.

A method to generate a squeeze film effect of two different intensities along a beam, pointing towards the possibility of a multi-point squeeze film device is presented [27]. A multi-modal approach is used, which consists of exciting two successive flexural modes of the beam, around the middle of their resonant frequency. Combining two successive bending modes enables to obtain two different vibration amplitudes in two points of the beam, because each vibration mode has a specific modal amplitude.

The squeeze film enables to generate subtle effects thanks to the variable friction. Texture simulation as previously mentioned is of prime importance, however it is inherently single touch. Recent developments are targeting multi-point feedback but it seems to be rather difficult to reach.

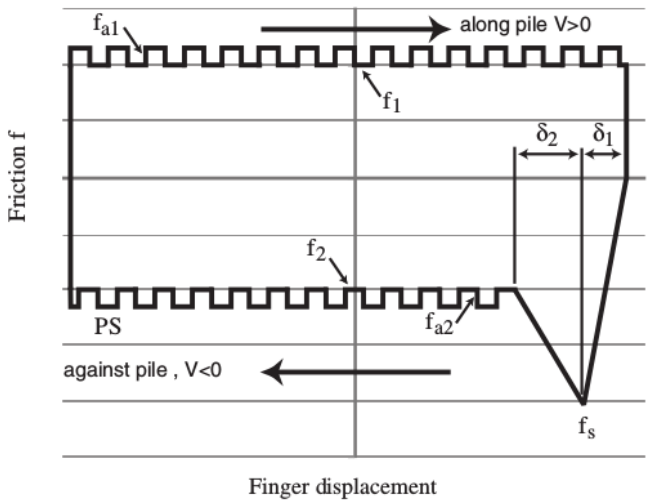

Figure 2.25: Model friction curve with the tribological features used for the STIMTAC signal control, from [8]. Different signals are used to reproduce the sensation of exploring velvet fabrics (an f1 friction level while exploring along the pile, an lower f2 friction level while exploring against the pile, fs the friction level while changing direction of exploration and a modulation fa1 and fa2 to reproduce the fiber tuft.

Electrovibration effect

Electrovibration was first reported by [59] in 1953, as a perceived effect resulting from tactile exploration of metallic surfaces covered by a thin layer of insulator and connected to an alternating voltage source. The effect induces an increase in the friction coefficient which makes the smooth metallic surface feel rougher. A sensation of vibration is perceived in the finger. The effect was later called electrovibration [31]. The insulating layer acts as the dielectric component of a capacitor. The two conductive plates are the metallic surface and the skin. If an alternating voltage is connected to the metallic surface, as shown in Figure 2.26, an intermittent electrostatic force is created between both plates of the capacitor, attracting the fingertip towards the surface. It was also noted that if the user was standing without shoes on a brick floor, the sensations were increased compared to a user wearing rubber-soled shoes. In order to maximise the effect, the user has to share a common ground with the stimulating device, which is depicted by a ground connection in Figure 2.26.

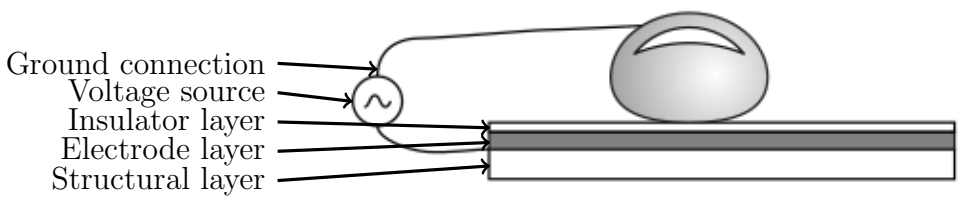

Figure 2.26: Principle of an electrovibration tactile device, with grounding wire, from [62].

As a result of the generated attractive electrostatic force, for which a model is

proposed in [61], [80], the apparent friction of the finger on the surface is increased. The variation in tangential force occurring during an exploratory motion generates an illusion of texture (see Figure 2.27). While the finger moves, the outer layer of skin adheres more to the surface, resulting in a shearing deformation on the fingertip's skin. On the other hand when the finger is stationary nothing is perceived. The electrovibration approach can only provide feedback during active exploration, which makes it suitable for simulating texture.

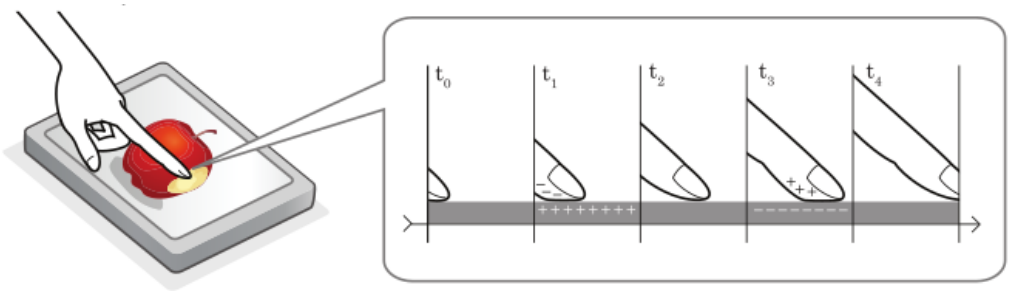

Figure 2.27: As the finger moves across the screen, the electrostatic force is varied according to the targeted texture feedback, from [3].

The use of this effect in a tactile display was demonstrated by [74] in 1970 with a small electrode array (10 by 18 electrodes) covered by a thin insulating layer. When the electrodes are powered with an AC voltage, a texture can be perceived by the user. The matrix-like structure allows rendering different shapes and patterns at fingers exploring the display. The opaque and bulky structure is nevertheless incompatible with a touch screen use.

More recently its integration with a touch input screen embedding a transparent electrode material (Indium Tin Oxyde, ITO) was demonstrated in [3]. Perceptive studies were carried out in an attempt to characterise the sensation produced by electrovibration. Low frequency stimuli (80 Hz) were rated as "sticky", whereas high frequency stimuli (400 Hz) were described as "smooth". An increase of the amplitude at 80 Hz and 400 Hz was perceived as rendering the sensation even "smoother". The variation of the signal's amplitude and the waveform are critical parameters that modify the displayed textures (see Figure 2.28).

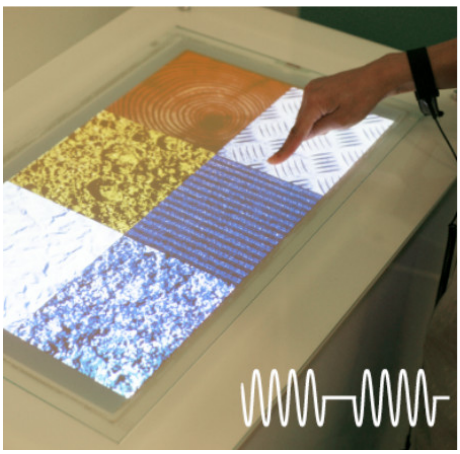

Figure 2.28: Different textures produce different sensations, e.g. simulated textured metal, from [3].

A rendering algorithm to produce tactile illusions of 3D geometric features on a flat transparent touchscreen is presented in [54] by controlling the friction between the fingertip and the touchscreen using electrovibration (see Figure 2.29a). To create the illusion of a bump, the algorithm relies on mapping the gradient of the virtual bump to lateral friction forces (see Figure 2.29b). The mapped friction force is then used as a control signal to generate the electrovibration stimulation. A user study concluded that participants are three times more likely to prefer gradient force profiles than other commonly used rendering profiles, such as a simple height profile.

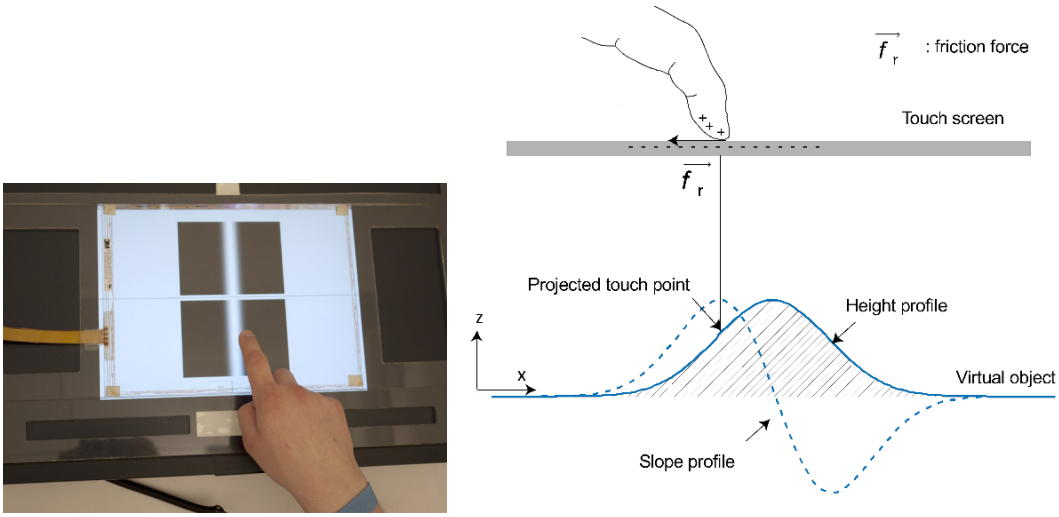

(a) Electrovibration display. (b) Slope and height profile of a bump.

Figure 2.29: 3D bump simulated by electrovibration friction control, from [54].

The previously mentioned work relied on ITO electrodes, which is a brittle material. An electrovibration set-up used graphene as new electrode material, which is flexible, for the insulated conductive surface [68]. This allows the system to be compliant with bendable devices.

Although electrovibration has great potential for texture reproduction [2] it suffers from several disadvantages. The sensation depends on the conductivity and the thickness of the user's skin [49]. Long rubbing of the finger on a surface triggers finger perspiration and humidity that degrade the strength of the electrovibration sensation. Screen cleanliness (grease or dust) has also an influence on the elicited sensation. One approach to overcome this problem is to use an intermediate pad of conductive material [86]. The electrostatic forces generated in this case are between the electrodes and the pad (see Figure 2.30). The forces exerted on the slider are then mechanically transmitted to the finger. The effect is therefore independent from the contact conditions, as opposed to the effect of sweat or variation in skin resistance [3]. This category of devices falls into the electrostatic type but lacks the direct natural interaction between the finger and the screen.

An electrovibration display relying on several sliders is presented by [64]. Instead of exciting the stator electrodes, several sliders are connected to signal generators and amplifiers (see Figure 2.31). The stator is connected to the ground. This configuration allows different stimuli on each finger, providing multi-point feedback, as shown in Figure 2.31a. Higher voltages and larger pads can be used to generate larger forces than systems using directly the fingertip. A bumpy surface and walls

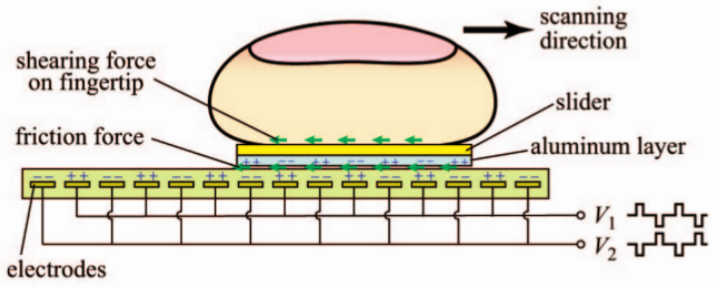

Figure 2.30: Principle of tactile simulation, with an intermediary slider, from [86].

were simulated (see Figure 2.31b). The pad motion is braked by the bumps and stopped by the wall. Although this approach overcomes the limitation of grounding the user, it can hardly be commercialised due to the wired mobile parts.

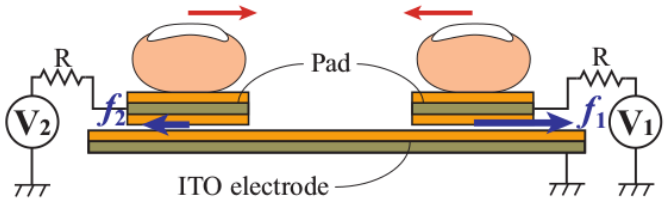

(a) Pads with different voltages stimulate fingers independently.

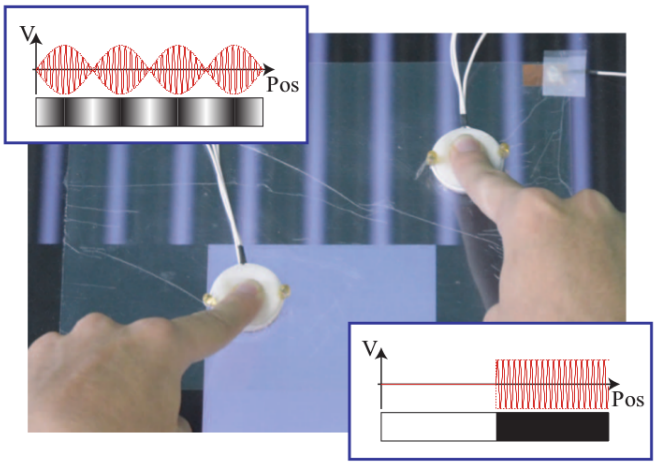

(b) Voltage profiles corresponding to grayscale image: bump (upper) and wall (lower).

Figure 2.31: A multi-finger electrostatic tactile display, from [64].

Both squeeze film and electrovibration rely on friction variation, which is perceivable only while dynamically exploring the surface. In terms of haptic feedback, they are able to simulate textures. However, they do not provide any feedback when the finger is static. Squeeze film seems to be limited to single point feedback as the whole interaction surface is vibrating whereas electrovibration can be extended to multi-point feedback, by using specific array-like electrodes arrangement, which are integrated on a transparent screen in [32].

2.4.4 Electrocutaneous stimulation

The previous devices focused on mechanical stimulations of the finger. Another alternative is to directly stimulate the nerve endings in the fingertip with an electric current. This process is called electrocutaneous stimulation. While [74] initially proposed an electrovibration device, the same electrode array was also tested without the insulating cover material. A current of a few mA is supplied to elicit a sensation on the finger. Compared to previous approaches, electrocutaneous stimulation has the advantage of being able to produce tactile feedback for both static and dynamic fingers. Fabrication of electrode arrays with a transparent conductive material such as ITO allows to use this approach on touchscreens (see Figure 2.32) [51].

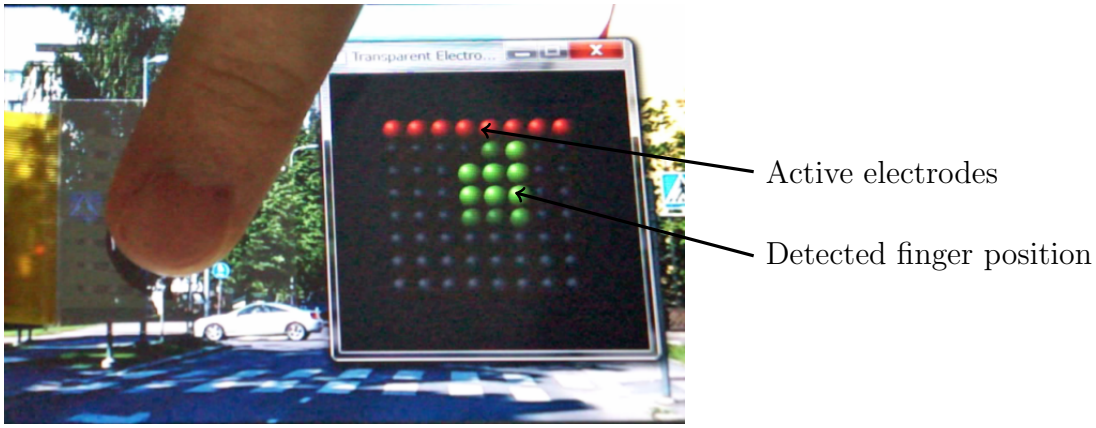

Figure 2.32: Transparent electrode array of an electrocutaneous display. Active electrodes and detected finger position, from [51].

On the other hand the difficulties of building an efficient electrocutaneous display are pointed out in [50]: Abrupt motion of the finger on the electrode array can cause an electric shock sensation. Furthermore, sweat alters the contact conditions and therefore the sensation's intensity (see Figure 2.33a). In addition, the two thresholds for tactile perception and pain are close to each other.Due to spatial variation of the perceived sensation, it is impossible to globally tune the intensity of the sensation without locally attaining the pain threshold (see Figure 2.33b). A real-time feedback of the contact impedance (1.45 µs feedback loop is achieved) to be able to adjust the sensation at each electrode individually is proposed in [50].

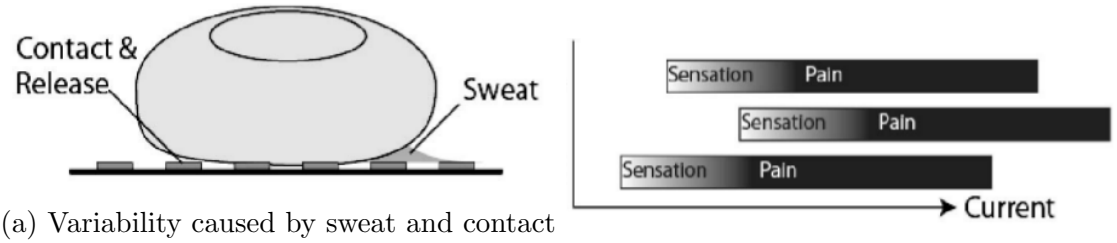

(a) Variability caused by sweat and contact conditions.

(b) Variation of tactile and pain thresholds.

Figure 2.33: Factors causing the sensation variability of electrotactile displays, from [50].

2.5 Hybrid interfaces

As noted from the previous sections, no single technology is able to fulfil all the challenges faced by haptic feedback on large surfaces: rich feedback such as key-click and texture stimulation, multi-point feedback, and ease of integration on touchscreens. Several research work, presented hereafter, propose to combine different tactile feedback technologies in order to enrich the haptic feedback.

A combination of a variable friction device based on squeeze film such as the one developed in [58] and key-click feedback relying on piezoelectric actuators is presented in [15] (see Figure 2.34). This enables the combination of texture feedback from variable friction (amplitude modulation of a 30 kHz squeeze film) and key-click feedback (500 Hz sine wave). However, the device is only providing global haptic feedback (same sensation for each finger).

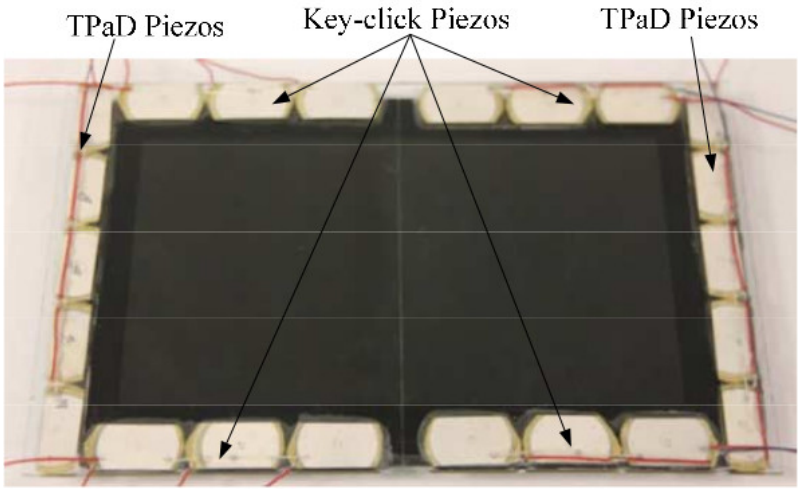

Figure 2.34: Friction control and vibrotactile feedback system, from [15].

A haptic display combining both lateral and normal vibrations is presented in [16], in order to generate lateral forces on the fingertip (see Figure 2.35). Both transducers are synchronised at the same ultrasonic resonant frequency ($\approx$ 22.3 KHz). The phase difference between these vibrational modes is used to control the magnitude and direction of the lateral force generated on the finger (maximum lateral force around 70 mN). A slope profile can be applied to the lateral force generation, in order to create a bump illusion.

While the previous device produced lateral vibration along only one axis, [63] combines a variable friction device with a mechanism capable of motion along two axes. This allows to apply forces in any in-plane direction on the fingertip while controlling the surface's friction (see Figure 2.36).

Although the generation of a lateral force on the fingertip by those devices is of interest, they are inherently single point feedback devices.

Variable friction approaches can also be combined. [29] presents the merging of squeeze film and electrovibration on a flat, non-transparent surface (see Figure 2.37). Squeeze film, controlled by a square signal at 5 Hz, W(t), is used to decrease the friction between the sliding finger and the surface. Electrovibration, controlled by pulses at 20 Hz V(t), is used to increase the friction. The dynamic forces are measured while combining both effects. The normal force of the finger on the surface

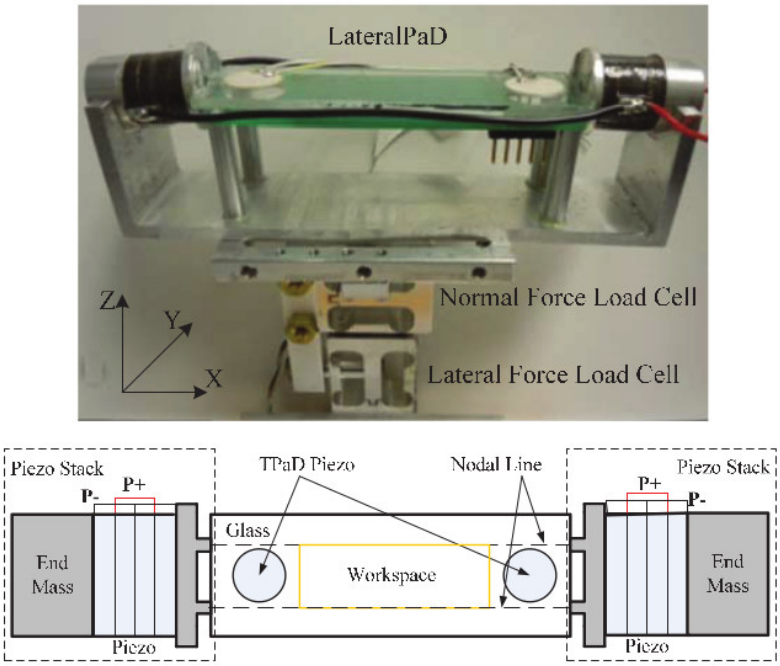

Figure 2.35: LateralPad, friction control and lateral force feedback system, from [15].

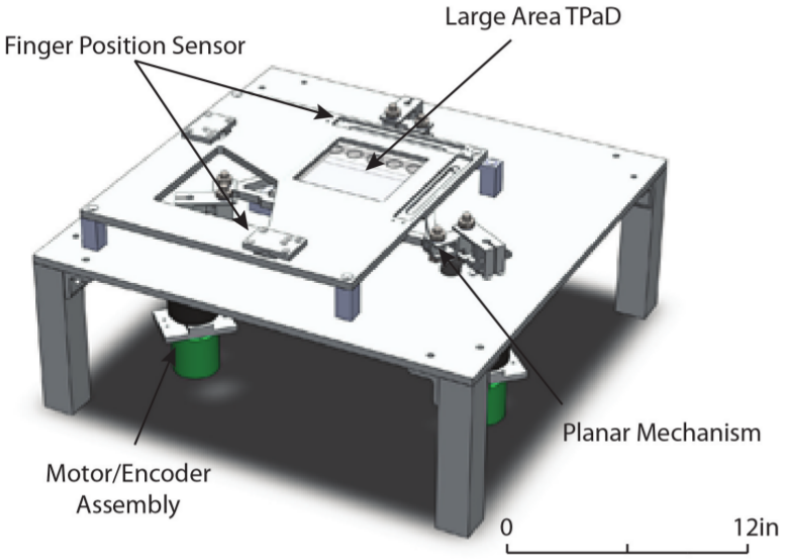

Figure 2.36: ActivePad, friction control and lateral force feedback system, from [63].

is constant at 0.6 N. When only electrovibration is activated, the lateral force Ft resulting from the friction variation shows pulses at around 0.3 N. Squeeze film alone decreases the lateral force from 0.25 to 0.2 N. When both effects are activated, the electrovibration induced lateral force pulses are decreased from 0.3 to 0.25 N. A model of the lateral force generation is proposed. Combining both approaches allows a broader friction coefficient variation range.

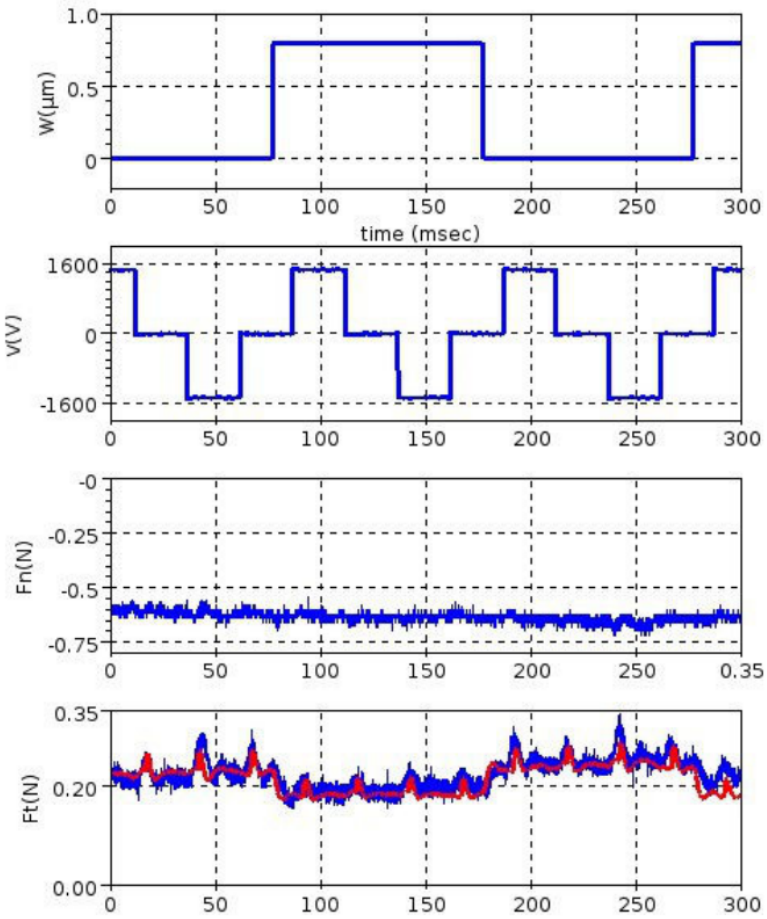

Figure 2.37: Combination of squeeze film effect modulated at 5 Hz (W) and electrovibration at 20 Hz (V). Lateral force Ft (measurements in blue, model in red), from [29].

2.6 Discussion and motivation of this work

Currently, there is no technology that is able to cover the whole range of haptic feedback. It is for example possible to generate physical buttons through surface deformation. Low frequency vibrations can produce a key-click feedback and high frequency vibrations, or better friction control, are able to display different textures while exploring a surface.

A comparative study is proposed based on the following four characteristics: ease of integration, multi-point feedback capability, key-click feedback, texture feedback (see Table 2.2).

Each technology relies on different actuators. Motors or electromagnets are for example bulky and integration becomes really challenging for large screen application. Piezoelectric actuators are relatively easier to integrate on touchscreen. Approaches based on mobile parts add mechanical complexity, while fixed vibrating parts are simpler to integrate. These characteristics are denoted in the **integration** criterion.

The localised or non localised character of the haptic feedback is also of interest. This results in the **multi-point** feedback capability of the device. A comparative criterion would be the spatial resolution of the tactile feedback.

The type of tactile feedback generated by each approach is of course of particular interest. **Buttons** enable to convey a key-click feeling to the user and **textures** enable to modify the surface roughness and to differentiate specific areas.

	Integration	Multi-point	Button	Texture
Pin array	–	++	+	-
Deformable surfaces	–	++	++	-
Lateral motion	–	-	-	+
Vibrotactile	++	-	+	+
Time Reversal	+	++	+	+
Squeeze Film	+	-	-	++
Electrovibration	+	+	-	++
Electrocutaneous	-	++	-	-

Table 2.2: Comparative study of the different haptic stimulation approaches.

Best suited for button feedback are deformable surfaces, then vibrators and time reversal. Deformable surfaces are however difficult to integrate in a touchscreen-based device, leaving vibrators and time-reversal as candidates.

Simple vibrators lack the multi-point feedback capability. However, this makes the time reversal of acoustic waves the first choice for key-click feedback.

For textures reproduction, squeeze film and electrovibration are the most interesting candidates. It is however difficult to localise squeeze film, which was demonstrated on beams [27]. Adapting electrovibration to local feedback is mainly technical challenge. Instead of having a single electrode on the screen, as in [3], several work proposed electrode arrangements to enable localised feedback [13] [52].

This comparative study strengthened our choice to study the complementarity between time reversal of acoustic waves, for its localised vibrotactile feedback, and electrovibration, for its friction based texture rendering.

Chapter 3

Time Reversal : theory and modelling

3.1 Introduction

Time reversal of flexural waves has been previously implemented on thin plates, to address the multi-point haptic feedback challenge [38]. The process relies on the focusing of flexural waves in a solid material. A constructive interference of flexural waves is generated at one or several points using actuators located on the perimeter of the surface. This allows the production of multiple localised vibrations simultaneously. The choice of a transparent material makes time reversal compatible with visual displays.

First, in section 3.2, the theory behind the time reversal approach is detailed. The general equation as well as practical implementation considerations are presented.

The main parameters influencing the process, such as the contrast ratio, the amplitude deformation or the number of actuators are then presented in section 3.3. The links between the different parameters are studied in detail and engineering trade-offs are proposed and discussed.

An analytical model based on Kirchhoff's equation for wave propagation to compute the spatial resolution of time reversal of flexural waves applied to plates is presented in section 3.4. A method to estimate the material characteristics of the plate is introduced to tune the model. Experimental measurements are then compared to the proposed model. Finally, the displacement amplitude of the focus point is measured and the relation between the amplitude and frequency band used is analysed.

The different considerations on the design parameters are then summarised in section 3.5 in order to reach design guidelines for devices integrating time reversal.

3.2 Theory of Time Reversal

3.2.1 Principle

Time reversal is a computational technique that takes advantage of the wave propagation's reversibility. The wave propagation equation in thin plates is described by the Kirchhoff-Love theory: $\rho\partial^2 u/\partial t^2 + D\nabla^4 u = 0$, with ρ the surface density, u the material displacement, t the time and D the plate's bending rigidity. This equation has a special behaviour with respect to the temporal variable: it contains only a second order time derivative operator. Any solution of this equation including initial and boundary conditions is symmetrical. This observation is the starting point of the time reversal approach. If $u(t)$ is a solution of the propagation equation, then $u(-t)$ is also a valid solution. t can be substituted by $-t$, meaning that if the waves produced by an impact are recorded and played backwards, they will focus at the original impact's location.

It is shown in [21] that it is possible to measure the temporal evolution of a wave-field inside a bounded propagation medium at discrete locations to be able to reconstruct the wave-field's initial state. Driving transducers at the same discrete locations with the previous measurements in a time-reversed configuration enables to reconstruct the whole wave-field at a given instant (see Figure 3.1).

Time reversal therefore enables the spatial and temporal focusing of mechanical waves using a set of remote transducers in a reverberating, dispersive, and even scattering medium, as long as it is stationary.

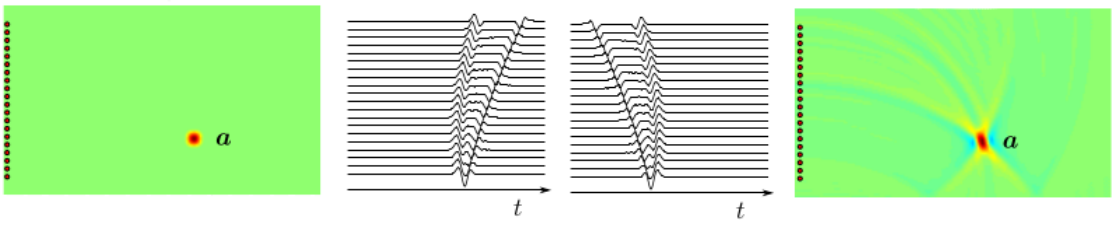

(a) Recording. (b) Emitting.

Figure 3.1: Principle of time reversal. An impact is generated at location a. A wave is propagated in the medium and is recorded by a set of transducers. These signals are time-reversed and emitted by the same transducers to obtain the reconstruction of the original impulse, from [40].

3.2.2 The fundamentals of time reversal

In a bounded domain ϕ, $h_{ab}(t)$ is the measured velocity of a point b, resulting from the application of a force impulse applied at time $t = 0$ at point a (see Figure 3.2). Thanks to the reciprocity principle, the sensor and the actuator can be interchanged, so that the signal recorded at a due to an impulse of force applied at b is the same, which means that $h_{ab}(t) = h_{ba}(t)$. Supposing now that the force applied at b is the response at a to an impulse applied at b, but inverted and shifted in time by T , that is, $f_b(t) = h_{ab}(T - t)$, the velocity at a point c is given by

$$v_c(t) = f_b(t) \otimes h_{bc}(t) = h_{ab}(T - t) \otimes h_{bc}(t) = \int_0^t h_{ab}(T - \xi)h_{bc}(t - \xi)d\xi \qquad (3.1)$$

where $\otimes$ is the convolution operation and ξ the variable of integration. If h_{ab} and h_{bc} are not correlated, waves interfere non-constructively, giving a background noise that can be modelled by a random signal with zero-mean velocity and standard deviation σ [18]. Applying the reciprocity principle, setting $c = a$, and time $t = T$ in Equation 3.1 gives,

$$v_a(T) = \int_0^T h_{ab}^2(T - \xi)d\xi \qquad (3.2)$$

The interference is now constructive, yielding a peak of signal localised in space and in time. This process is graphically represented in Figure 3.2 for a two dimensional domain.

3.2.3 Signal processing

Calibration and focusing

Time reversal focusing of flexural waves in thin plates is achieved in two steps. In a first step, an impulse source located at point a produces flexural waves which propagate and reverberate in the material. A set of Q transducers record the resulting out-of-plane displacements during a period T. The signal recorded by each transducer is the initial portion of the impulse response, $h_{aq}(t)$, between the source's location a and a transducer's location q. In a second step, the time reversed impulse

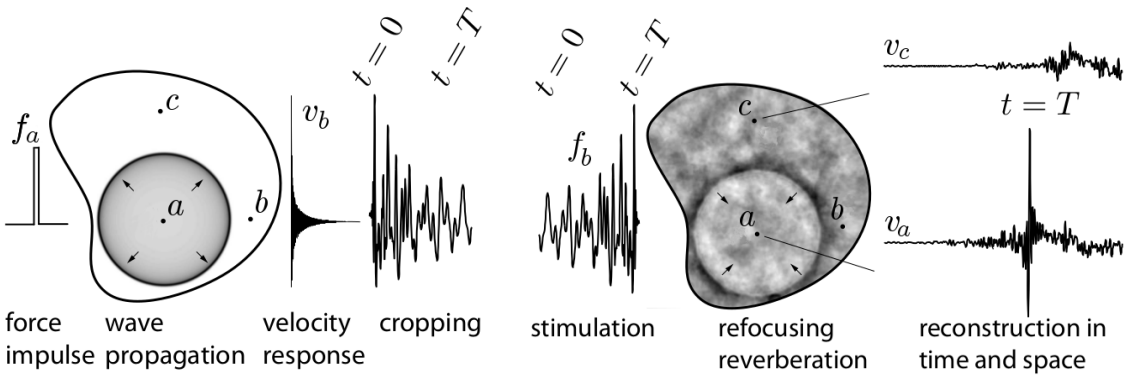

(a) Measurement. (b) Time reversal.

Figure 3.2: Time-reversal applied to a reverberant cavity. a) The velocity response at b of a force impulse applied at a is recorded and the initial portion of the signal length T is cropped. b) The signal is time-reversed and used as an actuator signal in b. Waves propagate and reverberate to eventually refocus in a. Perfect reconstruction would entail an infinitely long window and the absence of transducer noise. In practice, the response separates into a signal, as in a, and a background noise, as in a and c, from [41].

responses $h_{aq}(T-t)$ are used as driving voltage for the transducers. This leads to the focusing of the waves at point a and at time $t = T$.

From mechanical impacts to electrical white noise

The basic time reversal process described in the previous section appears to be simple but its implementation implies some challenges. The first one is to produce repeatable and calibrated mechanical impacts at the desired focusing point. The second challenge implies the use of a first dedicated electronics for signal acquisition during the calibration step and a second dedicated electronics for emission during the focusing step. Using the reciprocity principle, [38] showed that inverting the emission and the reception points gives an identical impulse response signal ($h_{aq}(t) = h_{qa}(t)$). The impulse responses can be acquired by sending separately an electric impulse $v_q(t) \approx \delta(t)$ to each transducer q and recording the displacement $u_a(t)$ at the focusing point a. The benefits are twofold: a short electric impulse is easier to generate in a repeatable manner than a mechanical impact and the transducers (piezoelectric actuators) are the same in the calibration and focusing step, reducing the electronics requirements.

Furthermore, it is possible to increase the input energy and thus, the signal-to-noise ratio of the acquired signals by replacing the short electric impulse with a wide band signal such as white noise [38]. In the frequency domain, the ratio of the measured displacement $U_a(\omega)$ to the driving voltage $V_q(\omega)$ gives the transfer function, $H_{aq} = \frac{U_a(\omega)}{V_q(\omega)}$. The impulse response $h_{aq}(t)$ is the inverse Fourier transform of the transfer function $H_{aq}(\omega)$. Therefore it is possible to get the needed impulse responses $h_{aq}(t) = TF^{-1}[H_{aq}(\omega)]$, where TF^{-1} is the inverse Fourier transform.

These improvements in the signal acquisition process are depicted in Figure 3.3a.

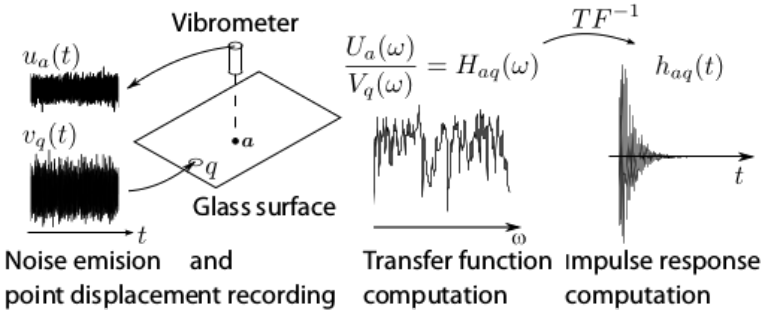

(a) Impulse acquisition.

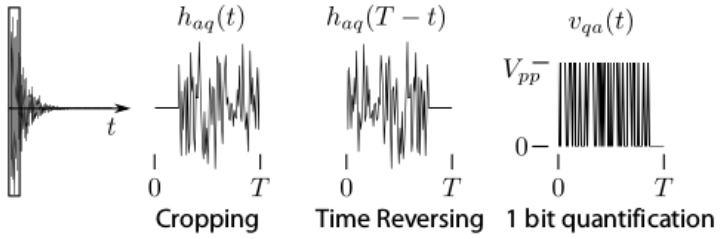

(b) Signal processing.

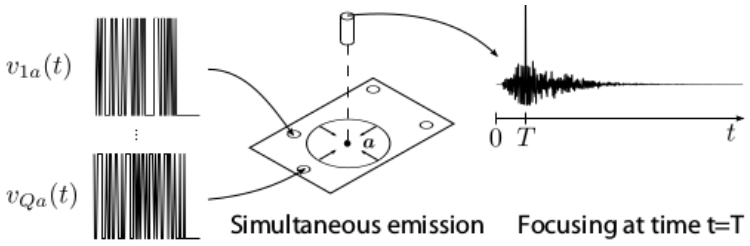

(c) Focusing.

Figure 3.3: Time reversal procedure to focus waves at a point a, using Q transducers. (3.3a) The impulse response between a transducer at location q and the focus point at location a is obtained by deconvolution of the measured displacement, $u_a(t)$, by the wide band driving voltage $v_q(t)$ applied to the transducer. (3.3b) The first seconds T of the impulse response are cropped, quantified on one bit, offset and amplified. Step 3.3a and 3.3b are repeated for each transducer. The impulse responses are then simultaneously sent to all transducers in step (3.3c) to achieve the focusing at point a and time T, from [39]

Simplified emission with binary signals

In the previous section, the drive signals are impulse responses, recorded in an analogue fashion. [38] simplified the drive signal by extracting only the sign of the impulse response, therefore constructing a binary drive signal $sign[h_{aq}(T-t)]$, as shown in Figure 3.3b. This preserves the focusing quality while increasing the displacement amplitude of the focus point [17]. The increase in amplitude is however gained at the expense of added noise emission, as binary drive signals generate more noise than analogue drive signals.

In addition, it simplifies the driving electronics, as the required analogue circuit is replaced by a simple switching electronics. Time reversal is a process insensitive to DC components, thus eliminating the need for bipolar amplification by simply adding a constant offset to the driving signal which becomes $v_{qa}(t) = \frac{1}{2}V_{pp}[1 +$

$sgn(h_{aq}(T-t))]$. Figure 3.3 summaries all these steps.

Simplified calibration

The impact produced by time reversal is localised but requires a calibration step, where for each impact location distributed in a uniform grid, the recording of an impulse response $h_{aq}(t)$ per transducer q is required. This quickly leads to a great number of impulse responses. This amount can be decreased by interpolation. This is achieved by spatially oversampling the measured impulse responses over the surface with a uniform grid of a pitch equals to half of the shortest excited wavelength λ_{min} . The total number of impulse responses N_m is in this case equal to the plate surface area S divided by half the minimum wavelength squared, that is $N_m = 4S/\lambda_{min}^2$ [38].

3.3 Engineering Trade-offs

It is possible to emit a single time reversed impulse response from a single actuator to create the focusing phenomenon [19]. However this is the least efficient scenario in terms of performances, as only small displacement amplitude can be generated. In the following sections, a number of design parameters are introduced: the contrast, describing the quality of the focalisation, the focus point's displacement amplitude, which is the deformation of the plate at the time of focalisation, the repetition frequency, the energy balance and the spatial resolution. The different optimisation alternatives and the associated trade-offs are investigated.

3.3.1 Contrast

The contrast is a measure of the quality of focusing, as it is defined as the ratio of the displacement amplitude reached at focused point a and time T to the quadratic average amplitude at any other location over the plate. It can be interpreted as a signal-to-noise ratio, where the signal is the displacement amplitude at the focus point and the noise is the remaining vibration elsewhere on the plate. In [40] an expression of the contrast ratio C in a finite sized thin plate is provided,

$$C = \sqrt{BT_c}\sqrt{\frac{Q\tau[1-exp(-2T/\tau)]}{(Q+1)\tau[1-exp(-2T/\tau)]+T_c}} \tag{3.3}$$

where Q is the number of transducers, T is the duration of the focusing process, B is the bandwidth of the driving signals, τ the attenuation time constant of the vibrations in the plate, and T_c the characteristic time of the plate, which depends on the plate dimensional and mechanical properties. T_c is given by,

$$T_c = \frac{\sqrt{3}S}{\eta}\sqrt{\frac{\rho(1-\nu^2)}{Y}} \tag{3.4}$$

with S and η being the plate surface area and thickness, and ρ, Y, and ν the material density, Young's modulus, and Poisson's ratio, respectively.

Equation 3.3 sets an upper bound on achievable contrast, with the maximum achievable contrast being $C_{max} = \sqrt{BT_c}$. Reaching high contrast values therefore requires to increase the signal bandwidth B. When attenuation can be neglected,

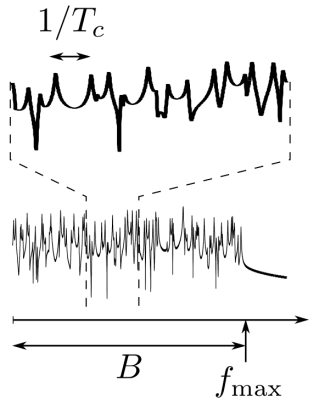

Figure 3.4: Characteristic time T_c and eigenmodes' density.

that is when $\tau \gg T$, maximum contrast is achieved when $QT \gg T_c$. When a plate with low attenuation is used, it is possible to increase the time-reversal duration, T , and thus use fewer actuators. Impulse responses however may drift significantly with temperature and degrade the performance of time reversal. To tackle this point, it was shown that reducing the time-reversal duration T makes the focusing process less sensitive to environmental variations [40], [69].

3.3.2 Amplitude

Tactile detection thresholds are frequently given in terms of skin probe vibration displacement amplitude [79]. The maximum amplitude of vibration at the focusing point and time is therefore of interest to maximise this quantity in order to generate a detectable stimulus. In the case of time-reversal focusing in a reverberating medium, the amplitude, A, follows [40],

$$A \propto Q\tau[1 - exp(-2T/\tau)] \tag{3.5}$$

Increasing the number of sources, Q, or the duration of the time-reversal window, T , not only increases contrast but also leads to a larger peak displacement. However, increasing T such as $T \geq \tau$, limits the amplitude gain.

3.3.3 Repetition

One approach to provide sustained stimulation is to repeat the focusing process in order to obtain a train of impulsive displacements. The repetition period, T_r, is limited by the attenuation of vibration in the medium. Indeed, the instant of focusing concludes the convergence of a wave-front toward the focal point where it produces a peak displacement. Immediately after focusing, that is for time $t > T$, the wave-front diverges from the focus point, reverberates in the plate, and decays with a time constant τ. When the focusing process is repeated at a period, T_r, that is smaller than the attenuation constant τ, decaying wave-fields resulting from previous impulses build-up. This leads to an increase of the background average displacement all over the plate. The focusing contrast is therefore sensitive to the repetition period. The effective contrast, $\hat{C}$, is governed by [39],

$$\hat{C} = C\sqrt{1 - e^{-2T_r/\tau}} \tag{3.6}$$

where C is the contrast of an isolated impulse. Over 93% of the initial contrast is therefore preserved when $T_r \geq \tau$.

3.3.4 Energy Balance

The effectiveness of the time-reversal approach for tactile stimulation depends on the amount of energy needed to achieve focusing at one point with a given amplitude, A, and spatial resolution, R_s (described in subsection 3.3.5). [39] evaluated the total mechanical energy, E, in the plate at the focusing instant, which gives,

$$E = \frac{\pi^3}{18}\frac{Y}{1-\nu^2}\eta^3\left(\frac{A}{R_s}\right)^2 \tag{3.7}$$

This energy corresponds to the energy transferred from the Q actuators to the plate during T seconds of emission. The average energy input per actuator is therefore $E_a = E/Q$ and the average power consumed by each actuator is $P_a = E/(QT)$. The plate thickness, η, as indicated in Equation 3.7 is a critical design parameter since the total energy is proportional to its cube.

3.3.5 Spatial Resolution

The spatial resolution R_s , or -3 dB width, is defined as the width of the focus point at half of its maximum displacement amplitude, as depicted in Figure 3.5 [39].

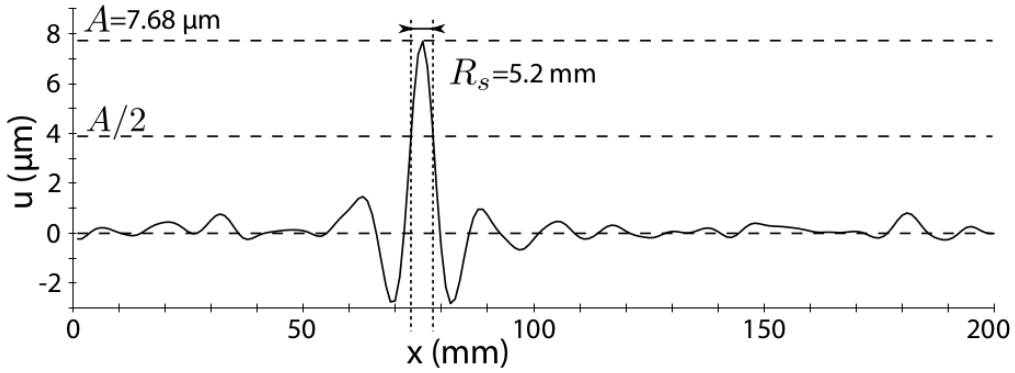

Figure 3.5: Focus point with an amplitude of 7.68 µm and a spatial resolution measured at 5.2 mm, from [39].

The spatial resolution R_s is a critical parameter for tactile displays. It is indeed directly related to the width of the focus point and dictates the minimum distance between two focus points in a multi-point feedback system. R_s depends on the frequency of the driving signals, the plate's geometry and the material. The state of the art however does not take into account variable frequency bands to derive an accurate predictive model for R_s. In the next section an analytical model for R_s is proposed and confronted to measurements on an experimental set-up.

3.4 Spatial resolution model

In this section, the focus is on predicting the spatial resolution R_s of the time reversal process, i.e. the focus point's size. With a wide bandwidth driving signal the point is circular, so the measure of its width is sufficient. The proposed analytical model is based on Kirchhoff's equation for wave propagation. The model requires accurate material properties, such as the Young's modulus Y, the Poisson's coefficient ν and the area density ρ_s. To tune the model, an experimental method is presented to provide an estimation of these parameters.

3.4.1 Analytical model

The displacement around the focus point u, located in $r = 0$, is described as superposition of plane waves (modelled by a Bessel function J_0,) of amplitude A, angular velocity ω and wave number k coming from every space direction and interfering additively in O [10], [40]. T is the focalisation time.

$$u(r,t) = \int_{\omega} A(\omega) J_0(kr) e^{j\omega(t-T))} d\omega \tag{3.8}$$

Spatial resolution R_s is given by the width at half-height of the focus point at the focalisation time, $u(R_s/2, t = T) = \frac{1}{2}u(0, t = T)$. For a constant bandwidth between pulsation ω_1 and ω_2, $A(\omega) = 1, \forall\omega \in [\omega_1, \omega_2]$, so:

$$\int_{\omega=\omega_1}^{\omega_2} (J_0(kR_s/2) d\omega = \frac{1}{2}\int_{\omega=\omega_1}^{\omega_2} J_0(0) d\omega = \frac{1}{2}(\omega_2 - \omega_1) \tag{3.9}$$

Taking the limited development of the second order Bessel function around O, $J_0(x) = 1 - (\frac{x}{2})^2$ and the dispersion relation in a thin plate $\omega = \sqrt{(\frac{D}{\rho_s})}k^2$ from the Kirchhoff's propagation model of waves in plates, gives:

$$\omega_1 - \omega_2 - \frac{1}{16}\sqrt{\frac{\rho_s}{D}} R_s^2 \left(\frac{\omega_2^2}{2} - \frac{\omega_1^2}{2}\right) = \frac{1}{2}(\omega_2 - \omega_1) \tag{3.10}$$

which is,

$$R_s^2 = 16\sqrt{\frac{D}{\rho_s}} \frac{\omega_2 - \omega_1}{\omega_2^2 - \omega_1^2} = 8\sqrt{\frac{D}{\rho_s}} \frac{2}{\omega_2 - \omega_1} \tag{3.11}$$

$$R_s = \sqrt[4]{\frac{D}{\rho_s}} \sqrt{\frac{8}{\omega_m}} = \sqrt[4]{\frac{D}{\rho_s}} \sqrt{\frac{8}{2\pi f_m}} \tag{3.12}$$

with $\omega_m = \frac{\omega_2 + \omega_1}{2}$ the mean angular velocity, $D = \frac{Y\eta^3}{12(1-\nu^2)}$ the bending rigidity and $\rho_s = \rho \cdot \eta$ the area density. By injecting $\omega_m = \sqrt{\frac{D}{\rho_s}}k^2, k = \frac{2\pi}{\lambda_m}$ into Equation 3.12, the spatial resolution can be expressed as a function of the mean wavelength λ_m:

$$R_s = \frac{\lambda_m \sqrt{8}}{2\pi} \approx \frac{\lambda_m}{2.2} \tag{3.13}$$

With Equation 3.12, the model links the spatial resolution to material properties included in the terms D and ρ_s and to the mean frequency of the used actuation bandwidth. Equation 3.13 explicitly points out the relation between the spatial resolution and the mean wavelength induced by the excitation bandwidth.

3.4.2 Material properties estimation

Without the accurate knowledge of the material properties, a method was used for estimation [1], [5]. It relies on measuring the surface wave velocity through the correlation of the recording of the same signal at different locations p and q on the plate. The correlation C_{pq}, in the spectral domain between two signals recorded in p and q is given by:

$$C_{pq} = \frac{S_p(\omega) \cdot S_q^*(\omega)}{|S_p(\omega)||S_q(\omega)|} \tag{3.14}$$

Where $S_q^*(\omega)$ is the complex conjugate of $S_q(\omega)$. From [1] and [5], we have:

$$E[\Re(C_{pq}(\omega)] = J_0\left(\frac{\omega r_{pq}}{V_\phi(\omega)}\right) = J_0(\alpha\sqrt{\omega} r_{pq}) \tag{3.15}$$

With E the expected value, $\Re$ the real part and $V_\phi(\omega)$ the phase speed of the waves at angular velocity ω. This phase speed in thin plates is given by:

$$V_\phi(\omega) = \sqrt[4]{\frac{D}{\rho_s}}\sqrt{\omega} = \frac{1}{\alpha\omega} \tag{3.16}$$

For a set of angular velocities ω and pairs p, q, the coefficient α is the one which minimises the quantity $\left(\Re(C_{pq}(\omega) - J_0(\alpha\sqrt{\omega} r_{pq})\right)^2$,

$$\alpha = arg_\xi min\left[\sum_w \sum_p \sum_{p\neq q} \left(\Re(C_{pq}(\omega) - J_0(\alpha\sqrt{\omega} r_{pq})\right)^2\right] \tag{3.17}$$

To estimate the material properties, regrouped here in the term α, a signal was emitted and recorded at different locations. Those recordings were used to compute the correlation term. Inserted into Equation 3.17, a value of α can be computed, which enables, according to Equation 3.16, to compute a value for $\sqrt[4]{D/\rho_s}$. This value represents an aggregate of the material properties for the time reversal plate. When applied into Equation 3.12, the spatial resolution model is tuned to our experimental conditions.

3.4.3 Experimental validation

Experimental set-up

Rectangular glass plates of dimensions 330 by 254 mm^2 with different thicknesses of 2 mm and 3 mm are used in the set-up. The plates are positioned on four supports in the corners and free on each side. The first resonant mode was measured at 41.5 Hz and 54 Hz for the 2 mm and 3 mm plates, respectively. The implemented transducers are piezoelectric diaphragms, (Murata 7BB-12-9 and 7BB-35-3), of diameter ⌀12 mm and ⌀35 mm and with thickness of 0.12 mm and 0.23 mm respectively. 16 transducers (8 on each side, in pairs facing each other) are glued with epoxy resin on the glass plates at a distance of 25 mm between the transducer's center and the plate's edge. A non symmetrical distribution as shown in Figure 3.6 aims at avoiding any symmetrical arrangements that would give correlated waveforms. The 16 transducers are driven in pairs in order to maximize the plate's deformation. A

total of four plates are studied, two 2 mm thick and two 3 mm thick plates. One of the 2 mm thick plates is equipped with ⌀12 mm transducers, the other one, with ⌀35 mm transducers. The same diaphragms(⌀12 mm and ⌀35 mm) are used for the 3 mm thick plates.

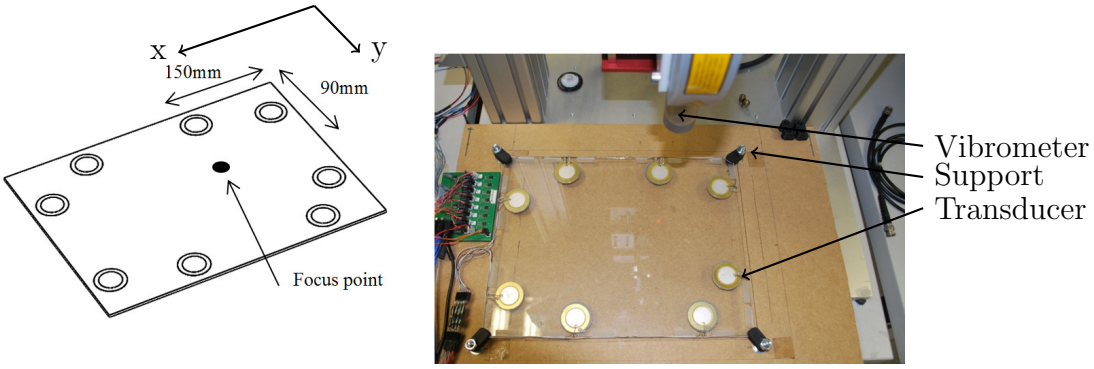

Figure 3.6: Position of the piezoelectric transducers on the glass plate, here ϕ 35 mm.

The acquisition and control software is developed in LabVIEW. Driving signals (sample frequency 50 kHz, giving a bandwidth of 25 kHz) are amplified to 30 Vcc through a custom electronics relying on OPA552 (gain set to 5) operational amplifier chips. The plate's displacements are measured with a laser vibrometer (Polytec OFV 534). Due to stability problems when driving the highly capacitive charge of PZT (Lead Zirconate Titanate ceramic material) transducers (⌀12 mm: 8 nF, ⌀35 mm: 30 nF at 1 kHz), a low pass filter component is added on the amplification stage. The gain is measured across the whole bandwidth ($0-25$ kHz) (see Figure 3.7). The gain is of an almost constant value of 5 between 0 and 8 kHz. At about 8 kHz the gain slowly decreases to reach 3.6 at 25 kHz, corresponding to a decrease of 28%.

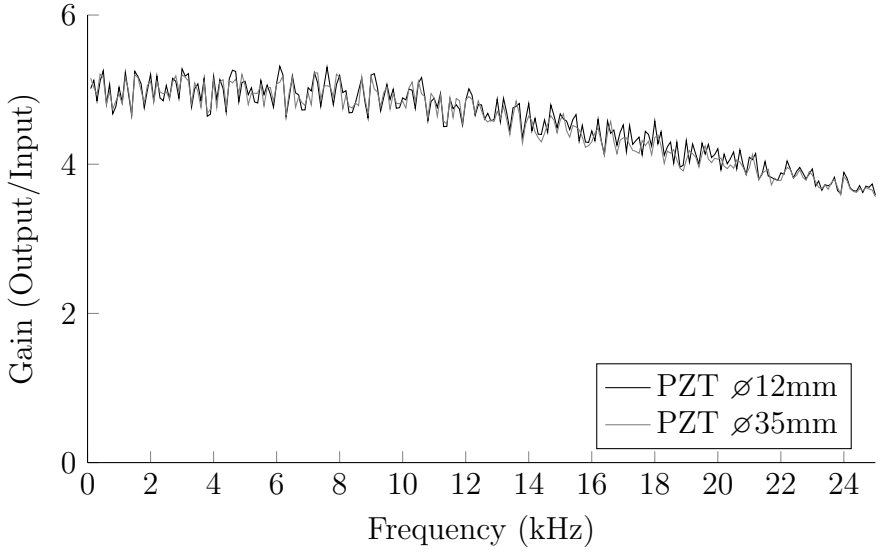

Figure 3.7: Gain of the amplification stage for the $0-25$ kHz bandwidth.

Spatial resolution and amplitude wide band measurements

A first study aims at determining the effect of plate's thickness and piezoelectric transducers surface on the dimension of the focus point while using the whole bandwidth ($0 - 25$ kHz) of the system. For each one of the four plates, the drive signals are computed for the coordinates ($x = 150$ mm, $y = 90$ mm) on the plate as shown in Figure 3.6. To obtain the spatial distribution of the wave's propagation around the focus point, measurements of the vibrations are taken along a grid of 60 by 60 mm^2 with a 2 mm step size, centered on the focus point as shown in Figure 3.8a. This allows reconstructing the propagation of the wave in the glass plate. The reversal time T is set to 2 ms. The corresponding time frame is used to measure the spatial resolution R_s of the focus point, which is defined as its width at half-height as shown in Figure 3.8b. The measurement is carried out along the cross section $A - B$.

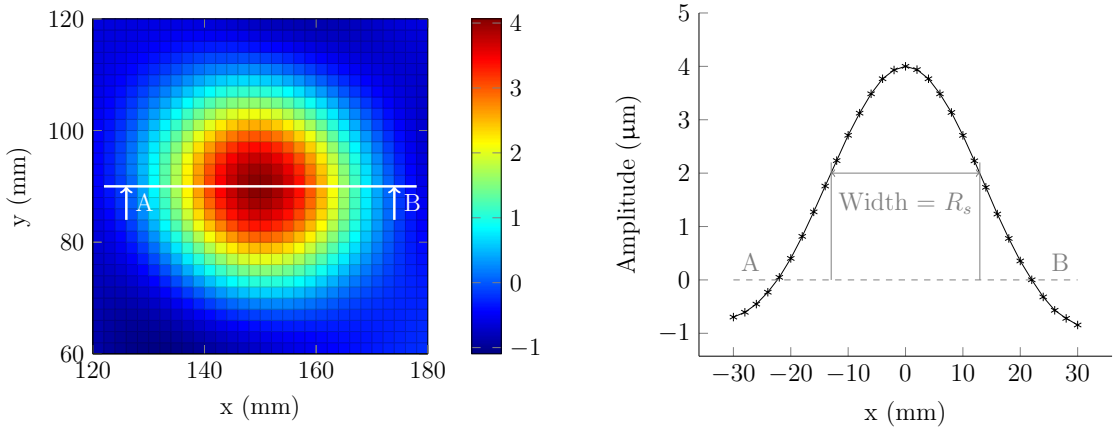

(a) Scan of the focus point.

(b) $A - B$ section and spatial resolution.

Figure 3.8: Displacement amplitude (µm) at the focus point for a 25 kHz wide bandwidth and $A - B$ cross section detail.

It is observed that for the four experiments the spatial resolution is relatively constant, at about 23 mm, as shown in Table 3.1. The measurements for the ⌀35 mm PZT transducers exhibit a stable width (23.7 mm and 23.1 mm), while those for the ⌀12 mm PZT transducer show a variation of 3.5 mm (22.2 mm and 25.7 mm).

R_s (mm)	⌀35mm	⌀12mm
Glass $\eta = 2$mm	23.7	22.2
Glass $\eta = 3$mm	23.1	25.7

Table 3.1: Spatial resolution R_s (mm) of the focus point.

The displacement amplitude A of the focus point decreases with increasing plate's thickness (-26 % for the 35 mm PZT and -16 % for the 12 mm PZT, see Table 3.2). This is explained by the fact that energy input E and the spatial resolution R_s remain the same while the plate's thickness η increases from 2 mm to 3 mm. According to Equation 3.7, if η increases with E and R_s remaining constant, A has to decrease.

To better understand how parameters such as the frequency band B, the plate's thickness η and the actuator's size impacts the spatial resolution R_s, different measurements are carried out. First, the time reversal process is limited to a 1 kHz

A (µm)	⌀35mm	⌀12mm
Glass $\eta = 2$mm	3.59	0.61
Glass $\eta = 3$mm	2.78	0.51

Table 3.2: Displacement amplitude A (µm) of the focus point.

bandwidth, starting with $0 - 1$ kHz up to $24 - 25$ kHz for plate's thicknesses of 2 mm and 3 mm and actuators of diameter ⌀12 mm and ⌀35 mm.

Narrow band spatial resolution measurements

With the method described in subsection 3.4.2, the α parameter for each plate thickness is estimated from Equation 3.17 (see Table 3.3).

Plate's thickness η	2 mm	3 mm
α	0.5434	0.4606

Table 3.3: Computed values for α for the 2 mm and 3 mm thick plate.

Figure 3.9 presents the spatial resolution R_s measurements for each frequency band for a 2 mm thick plate compared to the analytical model from subsection 3.4.1, which is based on the Kirchhoff theory. The estimated parameter α value is in this case 0.5434. ⌀12 mm and ⌀35 mm piezoelectric diaphragms exhibit relatively close values to each other and to the model. The different frequency bands resulted in spatial resolution variation from 60 mm ($0 - 1$ kHz) to 13 mm ($24 - 25$ kHz), and are in good agreement with the spatial resolution model.

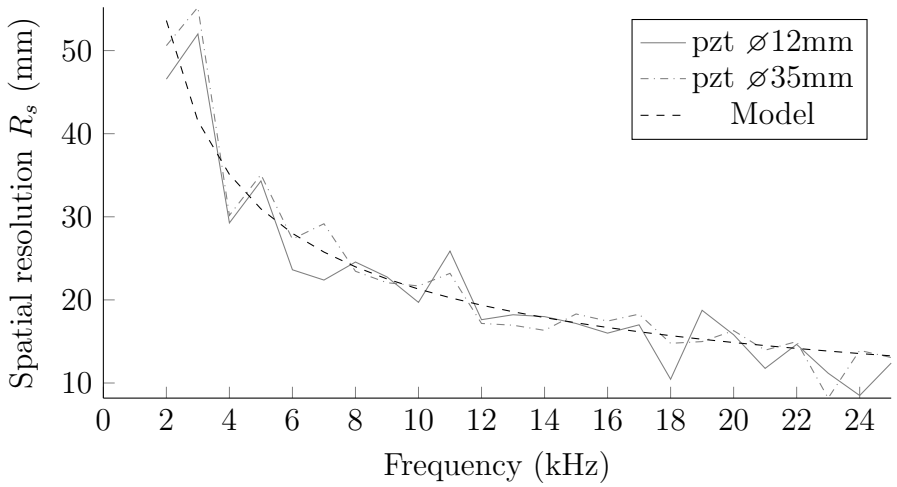

Figure 3.9: Spatial resolution R_s as a function of the bandwidth on a 2 mm glass plate.

Figure 3.10 presents the spatial resolution R_s measurements for each frequency band for the 3 mm thick plate compared to the analytical model from subsection 3.4.1, which is based on the Kirchhoff theory. The estimated parameter α value is in this case 0.4606. Both experimental data curves (PZT ⌀12 mm and ⌀35 mm) exhibit similar variations. The different frequency bands resulted in a spatial resolution variation from 77 mm ($0 - 1$ kHz) to 15 mm ($24 - 25$ kHz) corroborating the spatial resolution model.

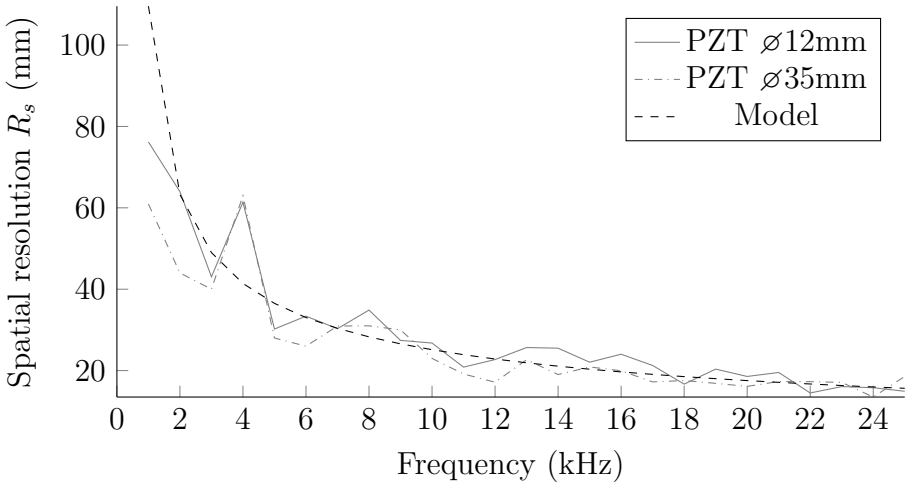

Figure 3.10: Spatial resolution R_s as a function of the bandwidth on a 3 mm glass plate.

Narrow band amplitude measurements

Figure 3.11 and Figure 3.12 present the amplitude of vibrations at the focus point, for each of the four plates. The displacement amplitude of the focus point varies strongly in the first half of the frequency domain ($0 - 12$ kHz) for both plates with ⌀12 mm PZT transducers (see Figure 3.11). In the second half of the frequency domain ($13 - 25$ kHz) a slow decay is noted. Similar behaviour is observed for both plate thicknesses with ⌀35 mm PZT transducers (see Figure 3.12).

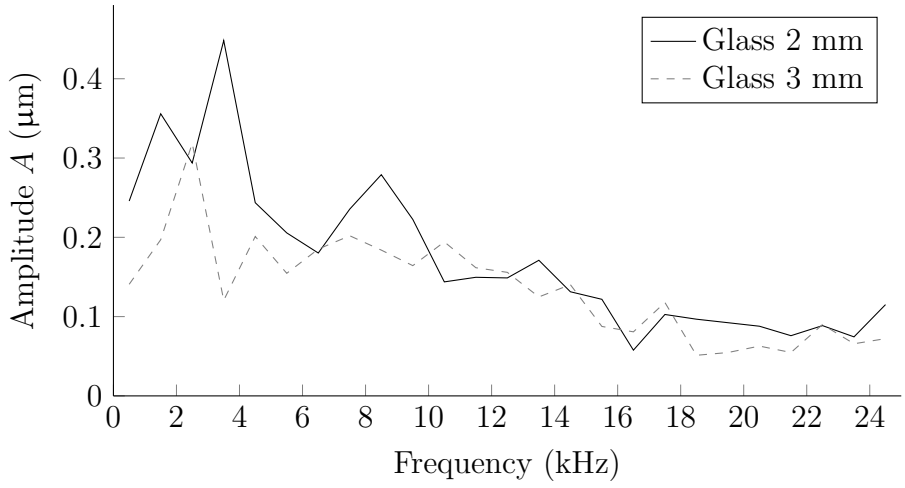

Figure 3.11: Displacement amplitude A of focus point for the ⌀12 mm transducers.

Figure 3.13 illustrates 2D scans from the spatial resolutions from the 2 mm thick glass plate equipped with ⌀35 mm PZT transducers. Depending on the frequency band, the focus point does not always result in a perfect circular deformation. For example, the focalisation process in the $1 - 2$ kHz band results in a circular shape, whereas in the $3 - 4$ kHz band it is an ellipsoidal shape and in the $9 - 10$ kHz band is close to a triangular shape.

To better understand the relation between the displacement amplitude A of the focus point and the frequency band B, the frequency response at the same location

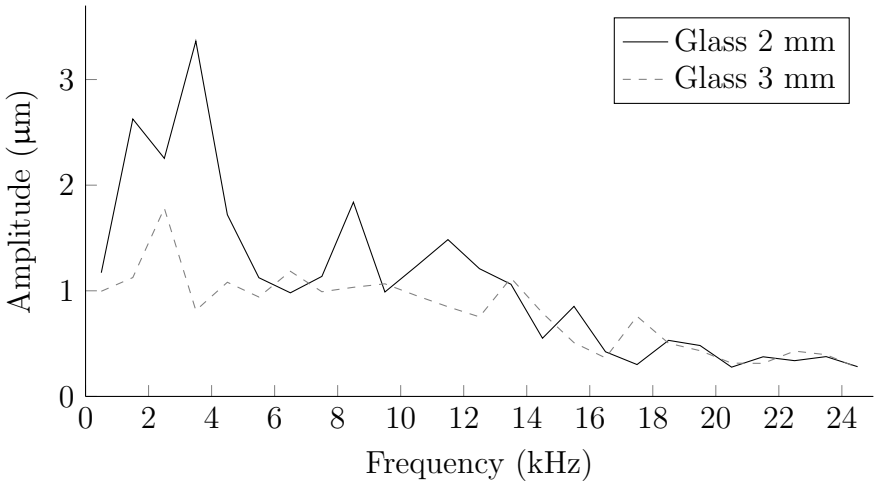

Figure 3.12: Displacement amplitude A of focus point for the ⌀35 mm transducers.

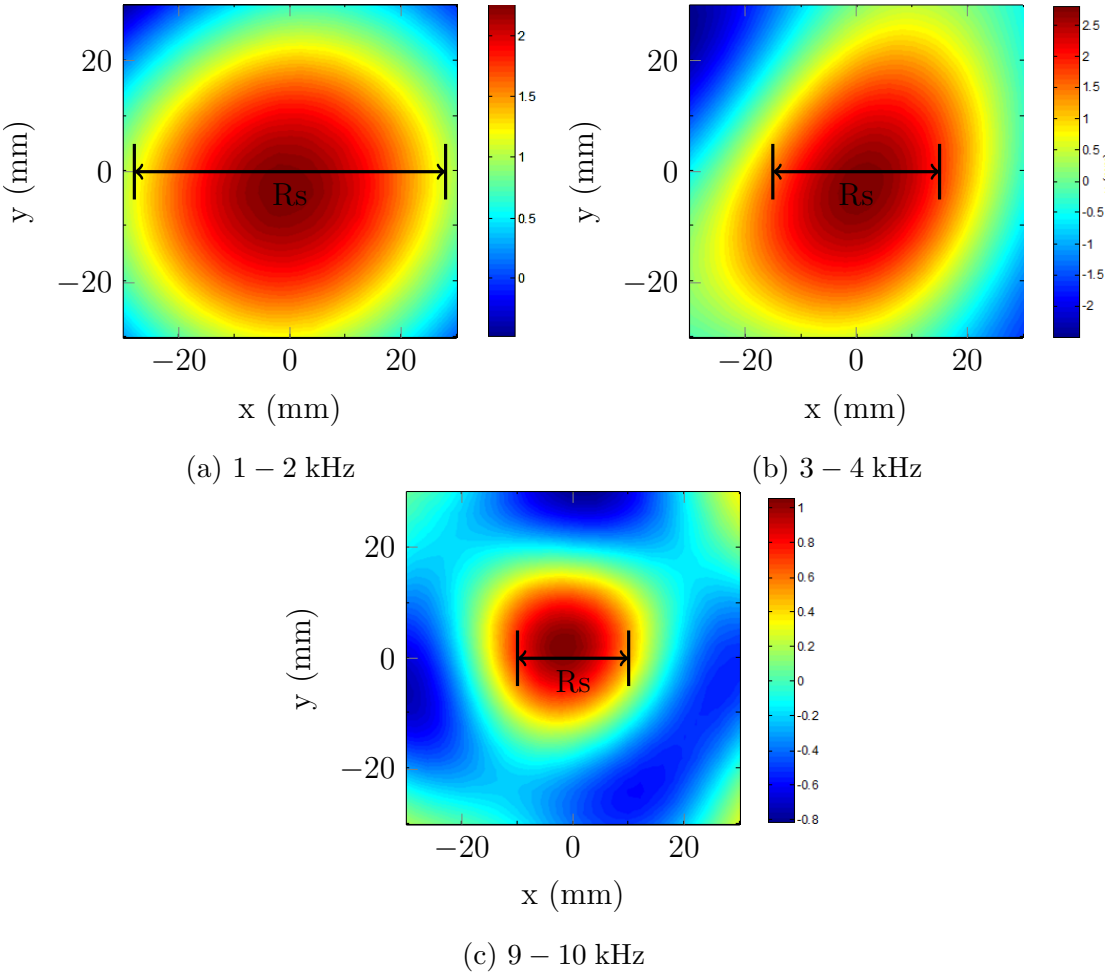

(a) $1 - 2$ kHz

(b) $3 - 4$ kHz

(c) $9 - 10$ kHz

Figure 3.13: Focus point's scan for specific frequency bands.

as the focus point is measured for a $0 - 10$ kHz frequency sweep (see Figure 3.14). An average of the frequency response is computed as FFT_{mean} and plotted on the same curve. In addition, the displacement amplitude of the focus point for each frequency band are reported.

As observed in Figure 3.14, for each frequency band, an increase in the mean

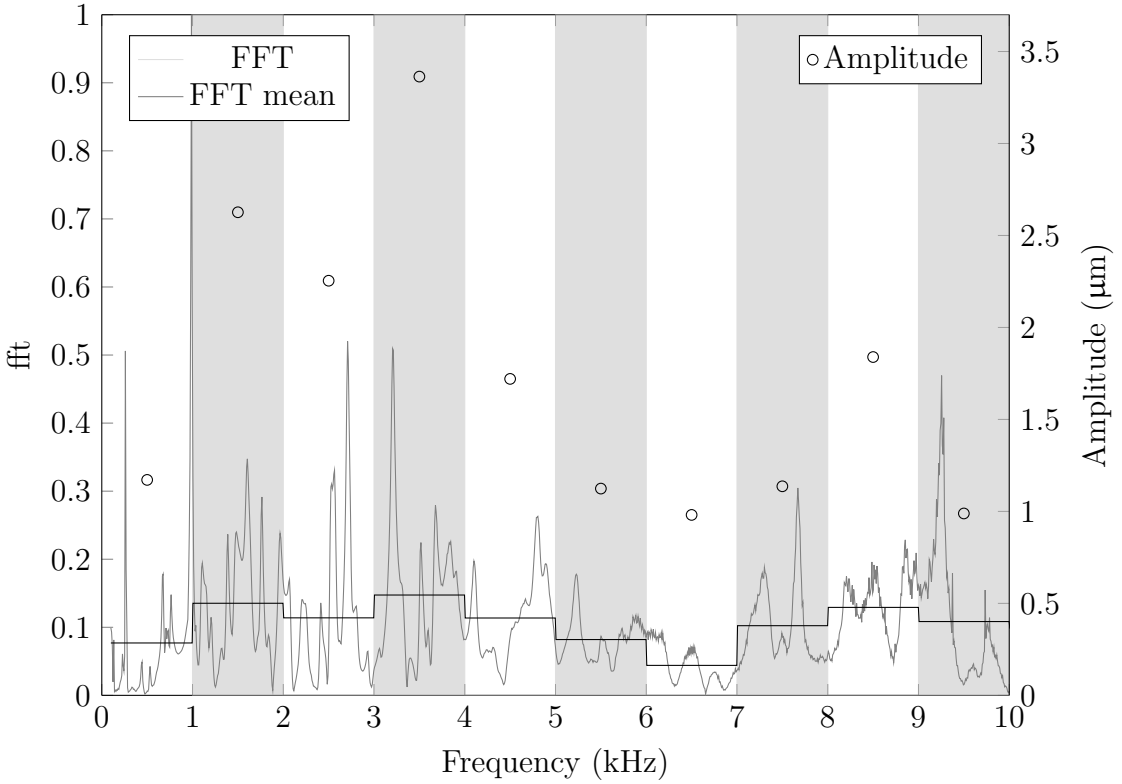

Figure 3.14: Frequency response at the focus point in the $0-10$ kHz band and focus point displacement amplitude A measurements on the 2 mm thick plate with ⌀35 mm transducers.

FFT value increases the displacement amplitude. In the $3-4$ kHz band, the mean FFT is the highest as the displacement amplitude reaches its maximum (3.4 µm). Time reversal in fact adds every contribution of every resonant mode.

Another observation is that on a $0-25$ kHz driving signal (total frequency band), the displacement amplitude is 3.59 µm (from Table 3.2. The $3-4$ kHz band generates a 3.4 µm deformation which represents 94 % of the amplitude generated by a $0-25$ kHz driving signal (a 25 times wider band driving signal). Therefore, time reversal could rely on choosing specific frequency bands to optimise the displacement amplitude. However, the $3-4$ kHz band signal produces a 30 mm spatial resolution ($f_{mean} = 3.5$ kHz), whereas a $0-25$ kHz driving signal produces a 23.7 mm ($f_{mean} = 12.5$ kHz). Generating large amplitudes requires to use low frequencies or a wide frequency band, whereas improving the spatial resolution requires to use a higher f_{mean}.

3.4.4 Discussion

Spatial resolution

For the considered $0-25$ kHz band, Figure 3.9 and Figure 3.10 show that for each glass thickness, the variations of spatial resolution R_s between ⌀12 mm and ⌀35 mm piezoelectric transducers are small. This indicates that the transducer's size has little influence on the achievable spatial resolution R_s, for the considered frequency band.

However it is also observed from Figure 3.9 and Figure 3.10 that parameters such

as the mean frequency of the driving band, the plate's geometry and the material have a direct impact on the spatial resolution. This was verified on 1 kHz frequency bands. According to the model, and confirmed by the measurements, the spatial resolution R_s decreases with an increase of the mean frequency of the excitation signal band, for given plate characteristics (material properties and geometry).

Considering that the minimum distance between finger contacts in multitouch interactions on a surface is around 10 mm, the spatial resolution of time reversal should be about 5 mm. Targeting a spatial resolution of 5 mm requires a mean frequency of the excitation signal around 170 kHz on the 2 mm thick plate and around 240 kHz on the 3 mm thick plate. However, the higher the frequency, the more challenging is the design of an analogue amplifier capable of driving the transducers at such frequencies. The spatial resolution also decreases with a decrease in the plate's thickness. In order to target a 5 mm spatial resolution, a thickness lower than 2 mm with a correspondingly reduced mean frequency would be a better choice, as it would require a lower mean frequency and hence, less complex driving electronics.

It is also noted that for some limited frequency bands, the focus point is not perfectly circular, as compared to wide band excitation signal (see Figure 3.8). The time reversal process adds the contribution from every frequency across the whole frequency band. However the deformation modes of the plates within a narrow frequency band could become dominant in the time reversal process and explain the non circular shapes observed in some cases.

Amplitude

The displacement amplitude A generated depends on the size of the transducers. For wide band drivings signals, the amplitudes generated by ⌀35 mm piezoelectric transducers are in average six times larger than those generated by ⌀12 mm piezoelectric transducers (on a 2 mm thick plate: 3.59 µm vs. 0.61 µm and on a 3 mm thick plate 2.78 µm vs 0.51 µm).

The displacement amplitude A of the focus point was also measured in each configuration, for 1 kHz bands. Strong variations are observed in the first half of the frequency domain ($0-1$ kHz until $11-12$ kHz). Measurements of the system's frequency response at the location of the focus point show a correlation between the density of eigenmodes and the focus point's displacement amplitude.

As also observed from the previous measurements, the displacement amplitude A decreases as the driving signal increases in frequency. In order to get sufficient amplitude, lower frequencies should be used. For the 2 mm plate, the contribution of the $3-4$ kHz is the most important. However, the audible range for humans ranges from 20 Hz to 20 kHz. There is therefore a compromise to find between the peak amplitude and the emitted noise that alters user acceptance.

3.5 Design guidelines

The previous sections of this chapter introduced the time reversal fundamentals and identified the different parameters that influence the process. These parameters are summarised hereafter in order to propose design guidelines, which are used in the next chapter to develop a new time reversal enabled haptic screen.

3.5.1 Plate's material Y, ν, ρ

For a desired amplitude A and spatial resolution R_s of focalisation, the choice of the material, in particular its Young's modulus Y is of importance. The required energy to deform the plate is proportional to the Young's modulus Y and to the squared Poisson's ratio ν^2 while the density ρ does not influence the required energy (Equation 3.7). Decreasing Y and ν at constant energy E, increases the displacement amplitude A and improves the spatial resolution R_s.

As in [39], the material for the new prototype development is borosilicate glass, which is transparent and commonly used as a material for the protective layer of touchscreens. A Schott B270 borosilicate glass is chosen, as its mechanical properties are very close to Corning's gorilla glass (compared in Table 3.4), a standard protective layer on smartphones and tablets.

	Schott B270	Corning Gorilla Glass 5
Y	71.5 GPa	76.7 GPa
ν	0.22	0.21
ρ	2.55 g/cm^3	2.43 g/cm^3

Table 3.4: Borosilicate glass and Corning Gorilla glass mechanical properties, from [65] and [14].

3.5.2 Plate's area S and thickness η

The energy balance of the focusing is not dependent on the the plate's area S (see Equation 3.7). However, the characteristic time T_c is proportional to S (see Equation 3.4). Increasing the plate's area increases the maximum achievable contrast ratio C_{max}. Dimensions of 200 mm by 300 mm are selected, leading to $S = 60000$ mm^2. The active surface is close to an A4 format and compatible with most tablets and tablet-PCs.

The energy balance is proportional to η^3, the plate's thickness. It is therefore the most dominant parameter. A thinner plate, enables to obtain at constant energy E a larger peak amplitude of displacement (see Equation 3.7) and a better spatial resolution (see Equation 3.12). There is a compromise to reach in terms of thickness. On the one hand, a thinner plate will lead to larger displacement amplitudes and a better spatial resolution. On the other hand, a thicker plate will be stiffer and hence mechanically more robust.

To estimate the lower admissible limit for the thickness, a 2 N force, corresponding to a finger pressing on the plate, is applied at its center. Borosilicate glass allows bending stress up to 30 MPa. If a security factor of 4 is taken into account, the bending stress should not exceed 7.5 MPa. This leads to a minimum thickness of about 1 mm, as shown in Figure 3.15a. A 1.1 mm thickness was selected, due to its availability. For a 2 N load at the center point of a 1.1 mm thick plate, the deflection is 0.17 mm, as shown in Figure 3.15b.

3.5.3 Bandwidth B

The maximum attainable contrast C_{max} increases with the square root of the product of the time constant T_c and the bandwidth B (see Equation 3.3). As T_c is given

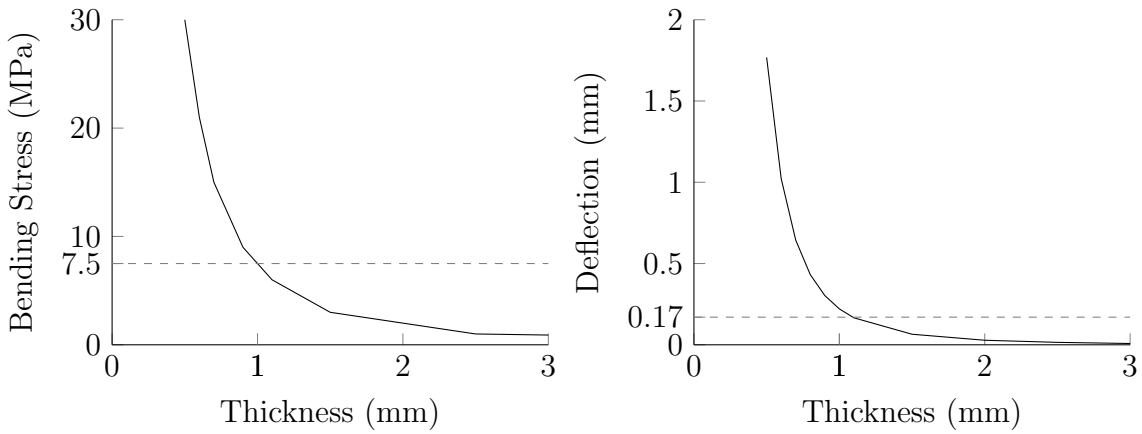

(a) Bending stress as a function of the plate's thickness.

(b) Maximum deflection as a function of the plate's thickness.

Figure 3.15: Bending stress and maximum deflection as a function of the plate's thickness, for a 2 N force applied at the plate's center.

by the plate's mechanical and geometrical characteristics, increasing B is the only possibility to increase C_{max}.

To limit the emission of noise in the audible bandwidth, the lower limit of the bandwidth should ideally be above 20 kHz. In this work, it is proposed to select $f_{min} = 25kHz$. The spatial resolution R_s is proportional to $1/\sqrt{f_{mean}}$ and $f_{mean} = (f_{min} + f_{max})/2$ (see Equation 3.12). Based on the model presented in this chapter and the material properties selected in the previous section, R_s is plotted as a function of f_{mean} in Figure 3.16. In this work, a spatial resolution of 5 mm is targeted, which corresponds to $f_{mean} = 87.5$ kHz. This leads to $f_{max} = 150$ kHz and a bandwidth $B = 125$ kHz for a 1.1 mm plate's thickness.

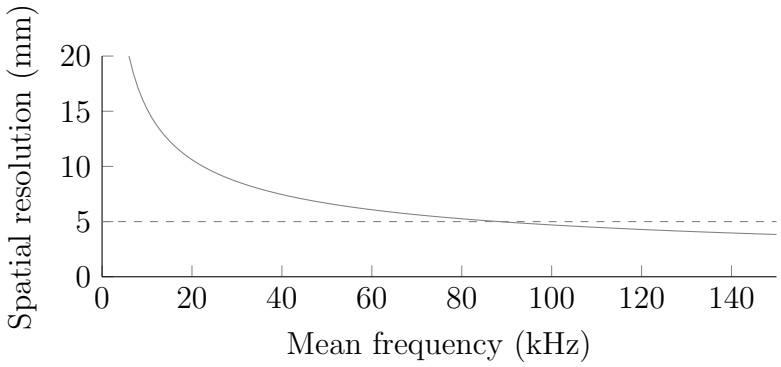

Figure 3.16: Spatial resolution R_s as a function of mean excitation frequency, for a 1.1 mm thick glass plate.

3.5.4 Characteristic time T_c

The characteristic time T_c of a plate is given by Equation 3.4 and represents the density of eigenmodes. On the considered plate, $T_c = 17$ ms, which represents $\rho_{modes} = 17 \cdot 10^{-3}$ per Hz (or 1.7 modes per 100 Hz) in average.

3.5.5 Attenuation constant τ

Impulse responses decay over time with an attenuation constant τ as shown in Figure 3.17. The value of the damping constant is not easily analytically predictable. It depends on the material, the surface of the plate and the plate's boundary conditions. Finite element simulations can be used to determine τ for a given plate. However a slight variation in the boundary conditions can significantly alter the results. Therefore, the preferred method to evaluate the plate's attenuation constant is through measurements (see subsection 4.3.1).

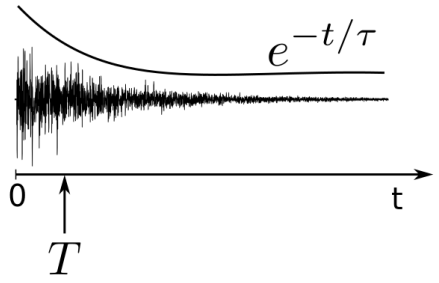

Figure 3.17: Impulse response, attenuation constant τ and reversal time T, from [40].

3.5.6 Reversal time T

T is the reversal time, during which the focalisation occurs. A longer T increases the displacement amplitude A. When $T \geq \tau$ the increase in A tends to saturate (see subsection 3.3.2), while a shorter T allows to increase the repetition frequency of the focalisation.

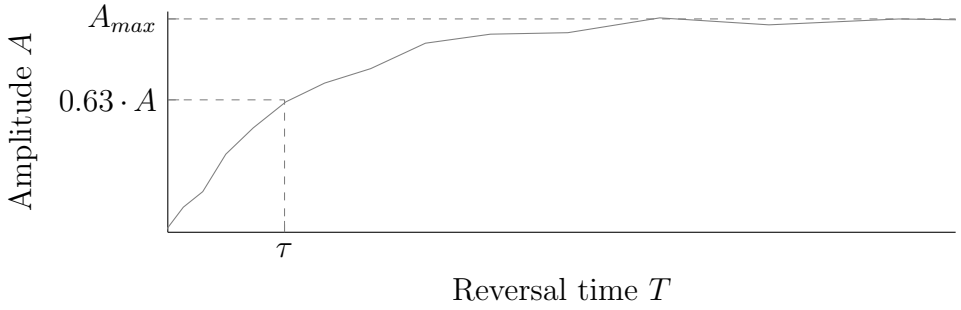

Figure 3.18: Displacement amplitude A of the focus point as a function of the reversal time T.

3.5.7 Repetition time T_r

The repetition time T_r gives the minimum time after which a new focalisation can occur, i.e a new haptic feedback (see Figure 3.19). Haptic patterns can be generated by repeating the focalisation process with different amplitudes A and at different frequencies. This can be used for complex signal generation by modulating the

amplitude A over time. A maximum repetition rate of 500 Hz to cover the human vibrotactile sensitivity range leads to a T_r of 2 ms.

The repetition time T_r has to verify $T \leq T_r$ so that the quality of focusing is maintained throughout the stimulation period. Indeed, if a new focalisation begins before the previous one is carried out, the driving signals of the second one mix with the first focalisation, resulting in a loss of both contrast C and displacement amplitude A.

The repetition time should also verify $T_r \geq \tau$ in order to avoid focusing noise build-up during repetition and, as a consequence, a loss of contrast C.

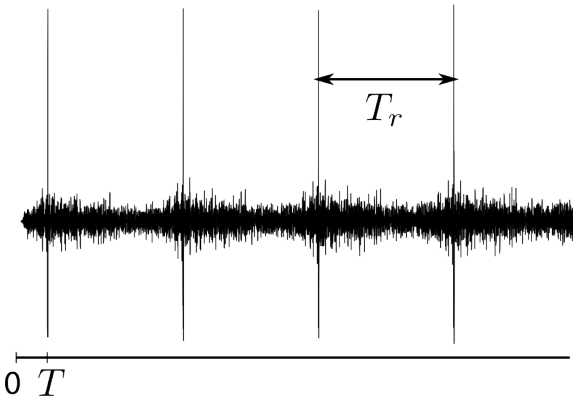

Figure 3.19: Repeated focalisation with a reversal time T and a repetition time T_r, from [40].

3.5.8 Time constant recommendation

From the previous sections, $\tau \leq T$ is required to reach a large amplitude. To maintain a good quality of focalisation, $T \leq T_r$ and $T_r \geq \tau$ are required. However, to reach a high repetition rate, T_r should be the smallest possible: $T_r = T$. A compromise is to choose $\tau \approx T \approx T_r$. The different time constants of the time reversal are represented in the time domain in Figure 3.20.

Figure 3.20: The time constants used in time reversal.

3.5.9 Contrast C

Maximum contrast C_{max}

Once selecting the bandwidth B and calculating the value of T_c, as described in the previous sections, the maximum achievable contrast is given by $C_{max} = \sqrt{B \cdot T_c}$. As T_c represents the eigenmodes' density (see subsection 3.3.1), $B * T_c$ is the number of eigenmodes N_{modes}. Therefore the maximum achievable contrast is directly related to the number of the plate's eigenmodes in the driving signals bandwidth by $C_{max} = \sqrt{N_{modes}}$. For the considered case in this section, $C_{max} = 39$.

Achievable contrast C

Neglecting attenuation, Equation 3.3 can be simplified to:

$$C = \sqrt{B \cdot T_c}\sqrt{\frac{2QT}{2(Q+1)T + T_c}} \tag{3.18}$$

So $C = C_{max} \cdot f(Q,T)$ with $f(Q,T) \to 1$ when $Q \cdot T \geq T_c$. In order to reach the maximum achievable contrast C_{max} and introducing the previously calculated value for T_c, $QT \geq 17$ has to be verified. The achieved contrast C depends on the number of transducers Q and the reversal time T as depicted in Figure 3.21. The contrast increases with the reversal time T but tends to saturate. With a larger number of actuator Q, a higher contrast C can be achieved.

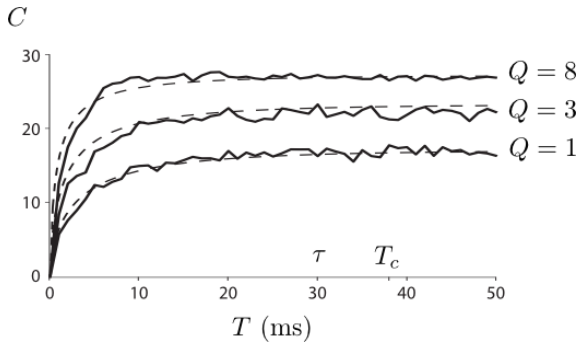

Figure 3.21: Evolution of contrast C as a function of the actuator's number Q and the reversal time T, from [39].

3.5.10 Number of transducers Q, and material properties

After fixing the reversal time T, the bandwidth B and the characteristic time of the plate T_c, the number of transducers Q is the last adjustable parameter to get the desired contrast. To reach maximum contrast, the number of transducers Q has to verify $Q > T_c/T$ (see subsection 3.5.9). To reach the desired repetition time, T_r should be 2 ms, implying a maximum reversal time of $T = 2$ ms. In theory Q should be at least 9. In order to carry out measurements on a broad range of parameters in the next chapter, it is chosen to develop an electronics capable of driving 32 piezoelectric actuators.

The amplitude at the focusing point is also proportional to Q (see subsection 3.3.2). The amplitude increases with the reversal time T (see subsection 3.5.6) and also with the transducer surface (see section 3.4.3).

The piezoelectric ceramics chosen as transducers have to present a good piezoelectric coupling coefficient d_{31} and a high Young's modulus Y_q to maximise the amount of deformation of the piezoelectric transducer transmitted to the plate and thus, the displacement amplitude A. Typical Young's modulus Y_q of PZT piezoelectric material are lie between 80 GPa and 160 GPa and typical d_{31} lie between -150 pC/N and -250 pC/N [20]. The driving voltage should be the maximum possible, while maintaining the electrical field in the ceramic below its breakdown field. In most piezoelectric actuated devices the driving voltage is limited by the driving

electronics. For security reasons, a driving voltage of 60 V would be a maximum upper limit for safe human-machine interaction, which limits the achievable electrical field.

The values calculated for the different parameters resulting from the design guidelines for a time reversal haptic screen are summarised in Table 3.5.

Plate's characteristics	
Young's modulus Y	71.5 GPa
Poisson's ratio ν	O.22
Density ρ	2.55 g/cm^3
Area S	200 x 300 mm^2
Thickness η	1.1 mm
Characteristic Time T_c	17 ms
Focalisation	
Spatial Resolution R_s	5 mm
Max. contrast C_max	39
Repetition Time T_c	2 ms
Min. number of actuator Q	9
Driving signals	
Min. frequency f_min	25 kHz
Mean frequency f_mean	87.5 kHz
Max. frequency f_max	150 kHz
Bandwidth B	125 kHz

Table 3.5: Parameters.

3.6 Conclusion

In this chapter, the theory of time reversal is first introduced. The design relationships between the crucial parameters of the system are given as engineering trade-offs. An analytical model for the spatial resolution is then proposed, based on Kirchhoff's wave theory. Experimental measurements are presented to validate the model. It appears that the thickness of the plate η influences significantly the spatial resolution R_s. However, no influence from the actuators size is observed on spatial resolution R_s for the studied frequency band.

To design a haptic interface based on time reversal, design guidelines are provided and summarised in Figure 3.22, based on the application requirements: size, material and spatial resolution:

- The size of the display on which the haptic feedback will be integrated is considered to be given. The haptic surface should be the thinnest possible, while stiff enough to withstand the finger's pressure.

- The plate's material is determined by the application. The choice of material for the surface is of high importance. It has to be transparent, in order to integrate the time reversal surface and not to interfere with the visual display.

- The spatial resolution is also an input requirement. Once the dimensions and the material are fixed, the spatial resolution R_s depends on the mean frequency f_{mean} of the driving signals (refer to the proposed model in section 3.4). The higher f_{mean}, the higher the spatial resolution. The maximum frequency f_{max} should then be as high as possible while maintaining f_{min} above the hearing threshold resulting in a wide bandwidth B.
- The dimensions and the material of the plate fix the characteristic time T_c of the plate (see Equation 3.4). With T_c and the bandwidth B fixed, the maximum attainable contrast C_{max} is given by $C_{max} = \sqrt{B \cdot T_c}$.
- The attenuation of the system τ, is given by the plate's material and the boundary conditions. The easiest method to determine the plate's attenuation constant is through experimental measurements.
- The reversal time T is bounded by τ and T_r, as it should verify $\tau \geq T \geq T_r$.
- To achieve a high contrast C, the number of transducers Q should verify $Q > T_c/T$.

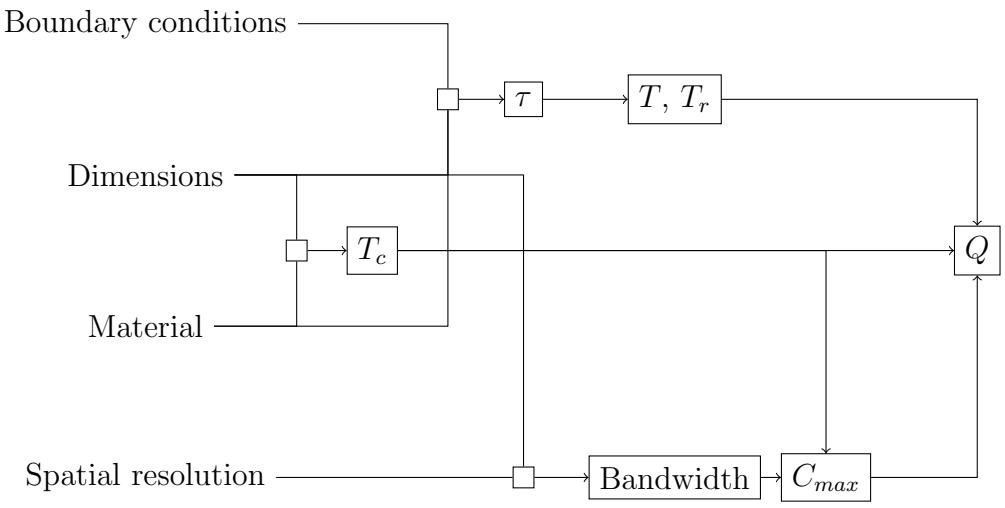

Figure 3.22: Application specific design guidelines.

The next chapter is focused on the design of a novel prototype, with specifications tailored to improve the amplitude of the focus point and the spatial resolution, while maintaining an appropriate contrast ratio.

Chapter 4

Time Reversal Performance

4.1 Introduction

In this chapter we introduce a time reversal haptic screen prototype with an A4 format. The prototype plate's material is borosilicate glass and its thickness is 1.1 mm. The 1.1 mm thickness choice is a compromise between the necessity of a thinner plate to favour greater displacement amplitudes and a thicker plate to favour mechanical robustness, as detailed in section 3.5. Dedicated electronics is developed allowing wide band excitation.

First the prototype's design is introduced in section 4.2. The different driving signals are then presented. Their influence on the amplitude and the temporal and spatial resolution are discussed in section 4.3. The power consumption is investigated in section 4.4 and the noise emissions are measured in section 4.5. Finally, the amplitude and spatial resolution measurements at different locations on the plate are discussed in section 4.6.

4.2 The tactile display prototype

4.2.1 The piezoelectric transducers

The prototype, shown in Figure 4.1 consists of a 300 by 200 mm^2 borosilicate glass plate (unit1.1mm) with 32 piezoelectric actuators.

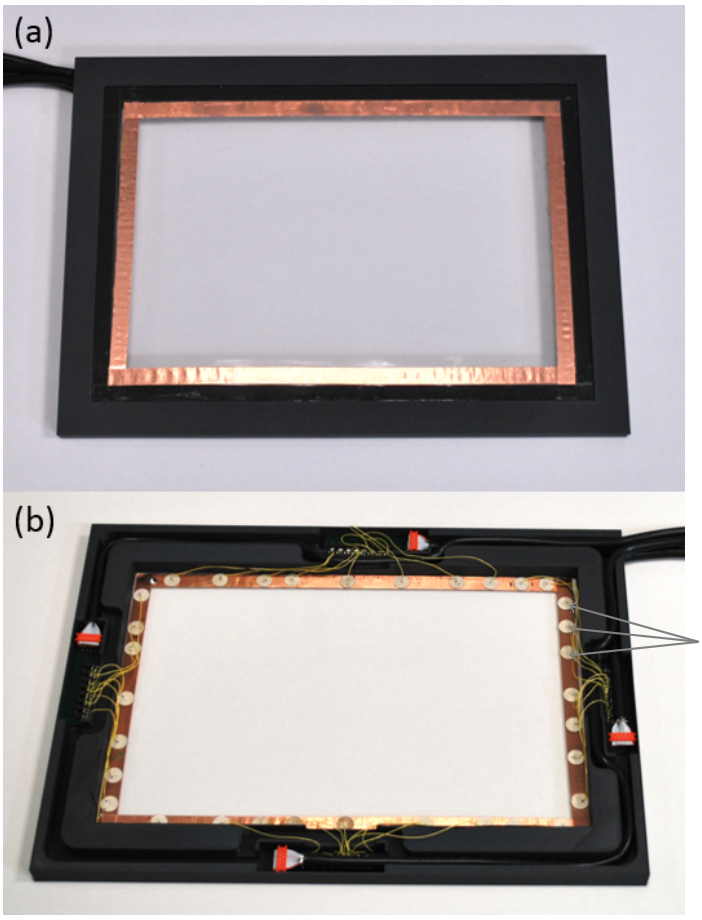

Figure 4.1: The time reversal haptic screen prototype. (a) the frontside. (b) the backside with the 32 piezoelectric actuators.

The glass plate is fixed on a 3D printed support with a 0.9 mm thick and 10 mm wide Polyethylene (PE) foam over the entire contour. The foam provides a damping effect, resulting in an increase of the attenuation constant of the plate and allowing a higher repetition frequency [41].

The piezoelectric transducers are fixed on the backside of the glass plate. A common ground is required to address all the transducers. A copper band of width 10 mm and thickness 0.1 mm is first fixed on the plate. The piezoelectric transducers are then glued on the copper band. Figure 4.2 indicates a cross-section of the prototype. Each piezoelectric transducer has a wire soldered on its free electrode, applying the high potential. A ground return wire is simply soldered on the copper band[1].

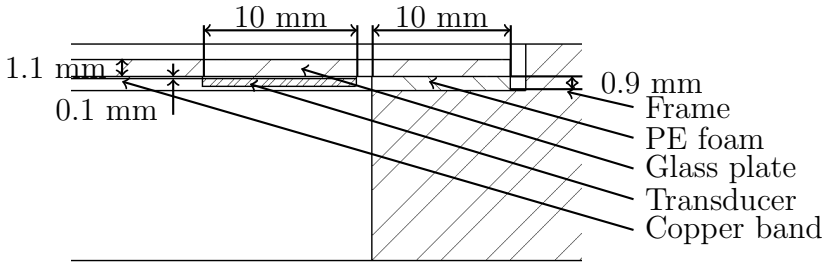

Figure 4.2: Section of the haptic display.

The diameter of each piezoelectric transducer is 10 mm, which is equal to the width of the copper band. When the total surface of the copper band with all the 32 transducers is calculated, it represents 17 % of the total surface. This would leave 83 % of the surface uncovered and then appropriate for interaction with a visual display. The required surface for the boundary conditions (in this case, the foam surface) is not considered in these calculations. In fact, if optimised, it can take limited space but this is not in the scope of this work. With ⌀20 mm transducers, the surface left for interaction would have been only 67%. Transducers of ⌀5 mm would leave 91% of the surface available. As detailed in section 3.4.3, a larger transducer surface produces a greater displacement amplitude. A ⌀10 mm is therefore a good compromise between leaving a large surface for interaction and having sufficient transducer surface to generate a large amplitude. 32 piezoelectric transducers (⌀10 mm, thickness : 0.5 mm, piezoelectric material from Ferroperm: PZ27 with characteristics described in Table 4.1 are used for this prototype.

Relative dielectric permittivity	K_{33}^T	1800
Coupling factors	k_p	0.59
	k_t	0.47
Piezoelectric charge coefficient	d_{33}	425 pC/N
	d_{31}	-170 pC/N
	d_{15}	500 pC/N
Mechanical Quality Factor	$Q_{m,t}$	80

Table 4.1: PZ27 material properties.

[1]Transducers with a special electrode arrangement (wrap-around contacts) would allow to solder both wires on one side of the transducers and therefore use less of the interactive surface

4.2.2 Driving electronics and amplification stage

A standard PC is interfaced with a NIDaqMX 6363 PCI-Express acquisition card controlled using python scripts. The acquisition card can drive 32 digital output channels ($0 - 10$ V) at up to 10 MHz. These signals are fed to a custom made amplification stage consisting of a mosfet driver (SI8244BB-C-IS) and a dual N-channel mosfet (FDS3992) layout for each channel, as shown in Figure 4.3. The mosfets drive the piezoelectric actuators with a $0 - 60$ V signal.

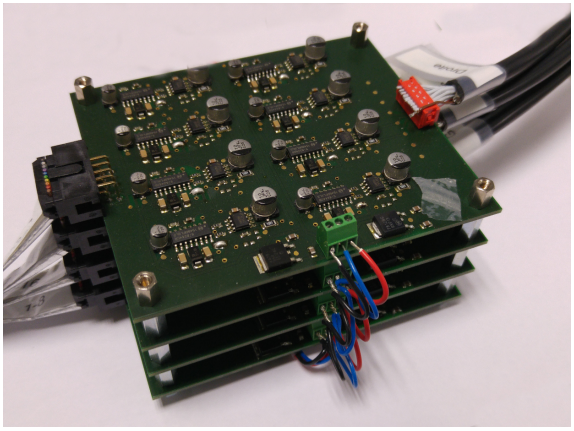

Figure 4.3: Stack of 4 boards, each embedding 8 amplification channels

In order to reach higher driving signal frequencies than the one used for the experimental results discussed in chapter 3, new electronics was developed. The previous amplification stage had a $0 - 25$ kHz bandwidth and used analogue amplifiers. In order to drive the piezoelectric actuators at a much higher frequency, a class-D amplification electronics has been designed. A class-D amplifier uses a high frequency digital signal as input, amplified to the required voltage level and then fed through a low pass filter, reconstructing an analogue signal of a lower frequency than the input. The advantage is that a high frequency digital amplification is easier and cheaper to design than its analogue equivalent. The design of the low pass filter adds little complexity to the design.

The low-pass filter is optimised for the piezoelectric actuator. The capacitance component of the filter is the piezoelectric actuator capacitance itself (2.1 nF), while a resistor (1 kΩ) and an inductor (470 μH) are added in series, resulting in a cut-off frequency of approximately 125 kHz. This results in an analogue signal of $0 - 125$ kHz bandwidth driving the piezoelectric actuators. The functional diagram of the electronics is shown in Figure 4.4.

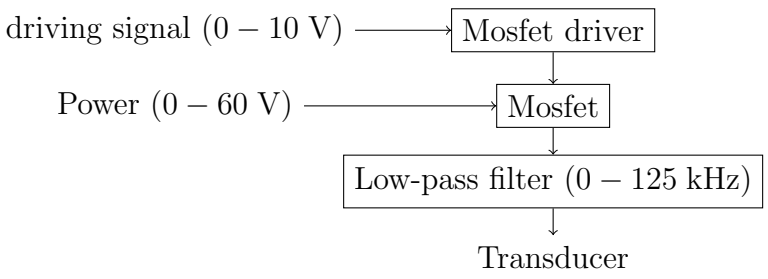

Figure 4.4: Functional diagram of the electronics.

4.2.3 Driving signals

As discussed in chapter 3, the driving signals are time reversed impulse responses, which are inherently analogue. As detailed in subsection 3.2.3, the time reversed impulse responses are derived by the following equation.

$$h_{aq}(t) = TF^{-1}\left(\frac{U_a(\omega)}{V_q(\omega)}\right)$$

The time reserved impulse responses $h_{aq}(T-t)$ are then subjected to a number of signal processing steps. First the signals are filtered, then quantified and then an offset is applied, to transform them into usable high frequency signals (4 MHz) as input for the class-D amplifier.

Filtering

In order to decrease the noise emission, a high-pass FIR filter is applied to the driving signals with a cutting frequency set at 25 kHz. As a result, the audible components of the signals applied to the transducers are reduced. In the following sections, the driving signals are referred to as **filtered** or **non-filtered** driving signals.

One bit quantification

A first quantification process, as previously covered in [39], is used to quantify the driving signals on one bit. This step consists of extracting the sign of the signal, as shown in Figure 4.5 and is referred to as **1b** signals. The square wave signal is fed to the amplification electronics used as a digital amplifier. The one bit quantification process has the advantage of being simple and providing more energy to the plate due to the square waveform, which results in higher displacement amplitudes at the focus point. However, one drawback is that more noise is generated as the square wave excites all the plate's eigenmodes.

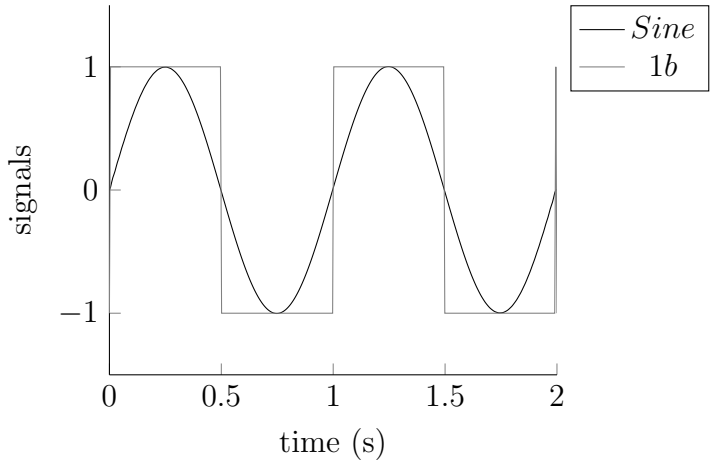

Figure 4.5: Quantification of a sine wave.

Modulation

A second quantification process is to use the class-D amplifier design by modulating the impulse responses signals at a high frequency. These high frequency modulated

driving signals are then filtered through the hardware low-pass filter to reconstruct an analogue signal. This case is referred to as **modulated** signals.

To compute the high frequency digital signal from the analogue impulse response, two modulation approaches are considered in this work : Pulse Width Modulation (PWM), which is a well known modulation method and Sigma-Delta Modulation (SDM). Figure 4.6a illustrates an example of pulse width modulation. The average voltage value applied to the transducers is controlled by the ratio, defined as the duty-cycle, between the "on" time and "off" time for each period of the modulated signal. Figure 4.6b illustrates an example of Sigma-Delta Modulation. The average value applied to the transducers is controlled by the density of pulses in the modulated signal. The high frequency modulated signals are amplified and smoothed by the low-pass hardware filter to apply an analogue signal to the transducers. In the developed electronics, the modulation frequency is 4 MHz to achieve a 125 kHz analogue output.

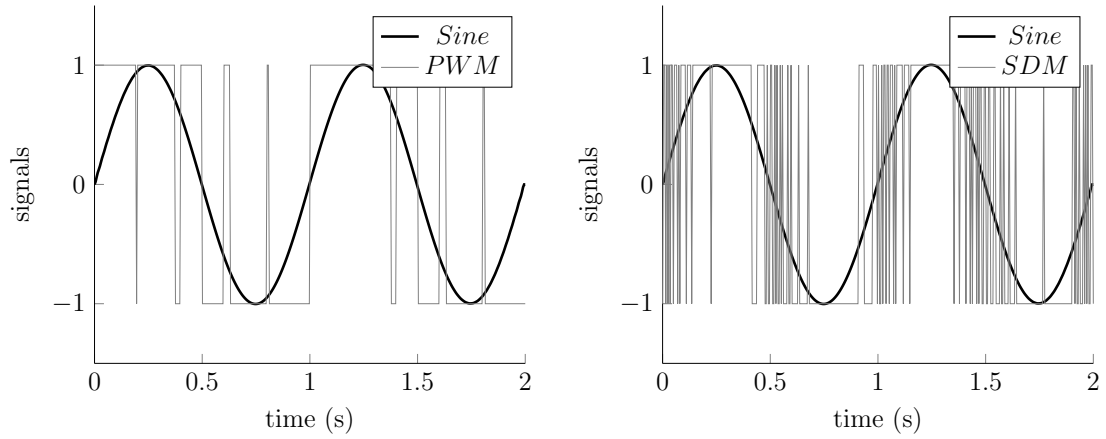

(a) 10 Hz PWM of a 1 Hz Sine.

(b) 400 Hz SDM of a 1 Hz Sine.

Figure 4.6: Comparison between PWM and SDM modulation methods.

Figure 4.7 presents the functional diagram of a Sigma-Delta modulation process of the first order. The input signal $X(n)$ goes through an integrator and its sign is extracted afterwards. The value of the output $Y(n)$ is subtracted to the next input value in a negative feedback loop (Z^{-1}). The number of integrators, and consequently, the number of feedback loops, indicates the order of a Sigma-Delta modulation. A second order Sigma-Delta modulation diagram, shown in Figure 4.8, is more complex but is more efficient in terms of noise reduction (discussed in the next section).

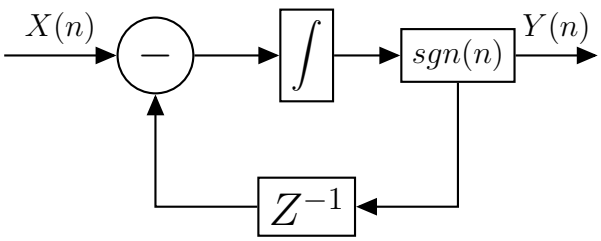

Figure 4.7: Diagram of a first order Sigma-Delta modulation.

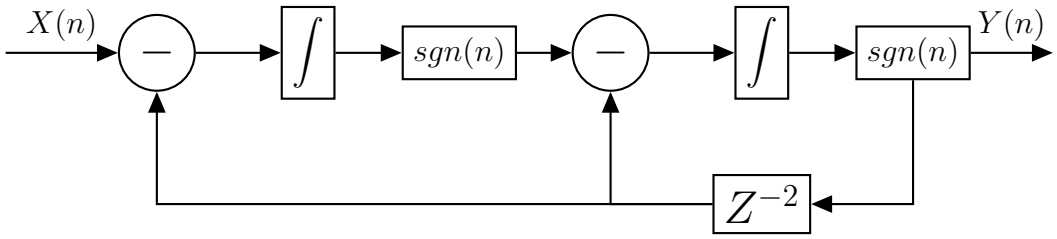

Figure 4.8: Diagram of a second order Sigma-Delta modulation.

Quantification and noise emission

In order to limit the noise emission, a comparison is made between the amount of noise added by the different quantification methods. A white noise signal sampled at 4 MHz is generated. A $25 - 125$ kHz band-pass filter is applied to the white noise signal to ensure that it does not include any frequencies in the lower audible frequency range. The different signal processing steps are then applied: 1b, PWM and SDM (SDM1 for the first order modulation and SDM2 for the second order modulation). Each of the modulation method adds noise inherent to the quantification process, which is called quantization error noise.

To compare the frequency spectrum of each driving signal, and thereby the amount of noise they add, a Fast Fourier Transform (FFT) is applied. The resulting FFTs are plotted in Figure 4.9 with a focus on the $0 - 25$ kHz band, where added noise is audible. It appears that SDM adds less noise than PWM and 1b quantification. The noise level is reduced when the order of the SDM is higher. In the following sections, the signals referred to as **modulated**, are processed with a SDM of the second order (SDM2).

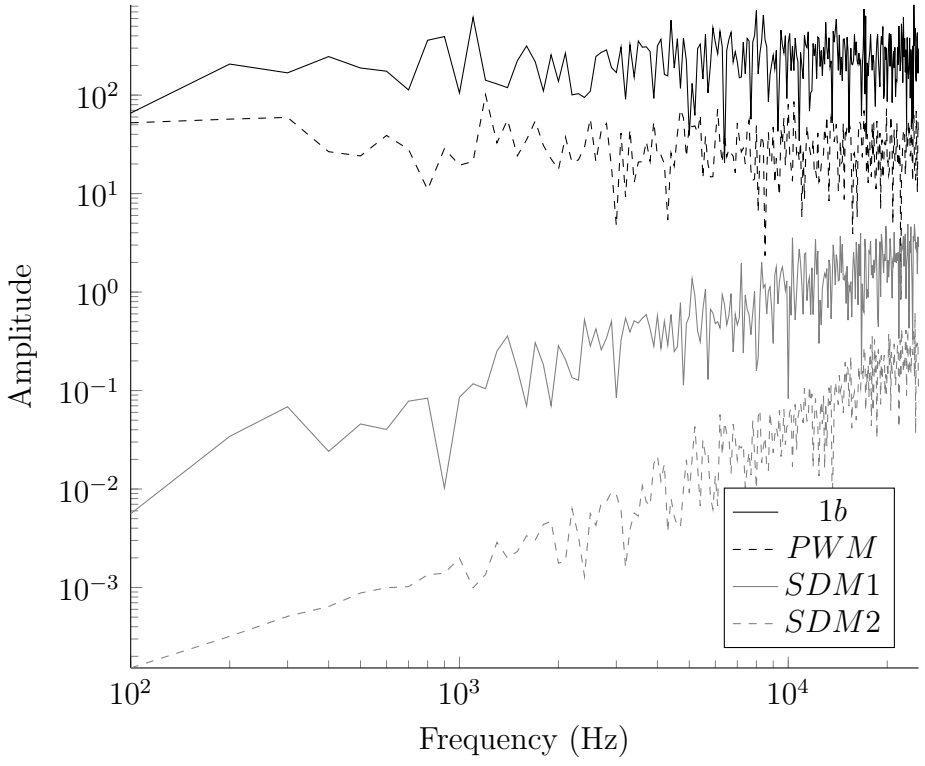

Figure 4.9: Spectral density of the quantification noise in the $0 - 25$ kHz band.

Offset and final signal

As time reversal is not influenced by DC components, previous designs based on bipolar amplification are replaced with a simple class-D based mosfet switching amplifier. Transforming the $\pm V_{pp}$ bound signals produced by quantification noted $Qtf(h_{aq}(T-t))$, into $0-V_{pp}$ bound signals is carried out by simply adding a constant offset to the driving signal which becomes,

$$v_{qa}(t) = \frac{1}{2} V_{pp}[1 + Qtf(h_{aq}(T-t))].$$

The different driving signals processing methods are summarised in Table 4.2.

	Audio filter off	Audio filter on
Quantification on one 1 bit	1b non-filtered	1b filtered
Sigma-Delta Modulation	SDM non-filtered	SDM filtered

Table 4.2: The different driving signals used.

4.3 Measurements : amplitude and spatial resolution

The first measurement to be achieved is to determine the attenuation constant τ of the glass plate. Once τ is identified, it is possible to determine the appropriate reversal time T (see section 3.5) which ensures a working focalisation process. The prototype is then characterised with the four different driving signals in terms of amplitude, temporal resolution and spatial resolution. The prototype is positioned under a laser vibrometer (Polytec, OFV 534), which records the focus point's displacement amplitude. The focusing is carried out at the center location of the plate, called point O, as shown in Figure 4.10. The voltage applied to the piezoelectric actuators is 60 Vpp.

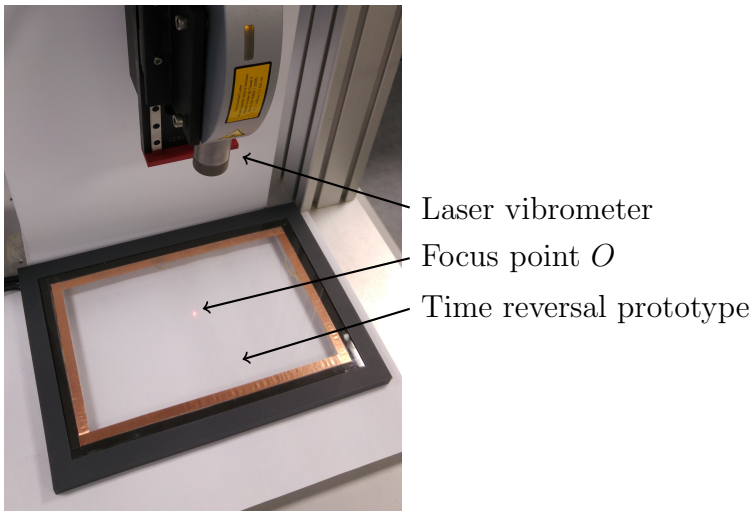

Figure 4.10: Experimental set-up, with time reversal prototype and laser vibrometer measuring the focus point's displacement amplitude.

4.3.1 Attenuation constant τ and reversal time T

Attenuation constant τ

The attenuation constant τ is the time it takes for a vibration to damp out to a near zero-level. Finite element simulations can be used to determine τ for a given plate. However a slight variation in the boundary conditions can significantly alter the results. A convenient way to determine the attenuation constant is through experimental measurements.

Impulse responses $h_{aq}(t)$ are deduced from the time reversal calibration process (see subsection 3.2.3). The normalised $h_{rms}(t)$ shows a logarithmic decay of the vibration amplitude, as seen in Figure 4.11. It is possible to fit a decaying exponential function $f(t) = e^{-t/\tau}$, in order to determine the attenuation constant τ. The fit gives an attenuation constant of $\tau = 1.8$ ms.

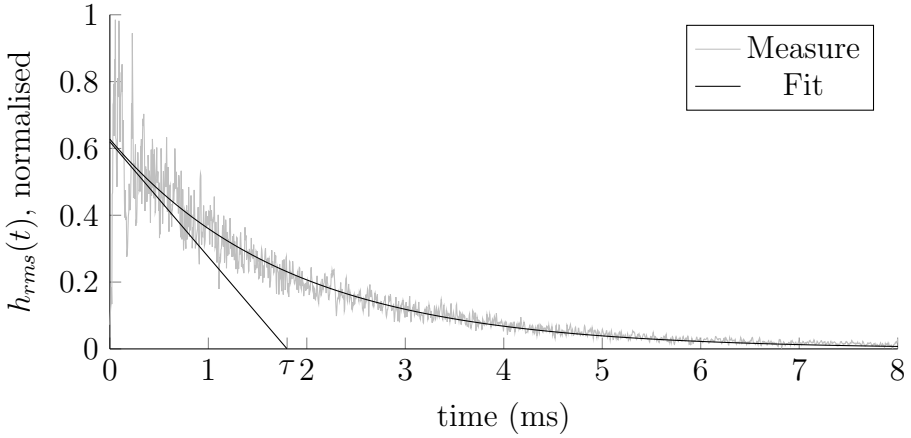

Figure 4.11: Fit of a decaying exponential on an impulse response signal.

Reversal Time T

As introduced in subsection 3.3.2 the amplitude at the focus point depends on the reversal time T. The reversal time should be longer than the attenuation constant τ to prevent accumulation of focalisation noise and the resulting loss of contrast [40]. However, the longer the reversal time T, the longer the repetition time T_r and the slower the repetition frequency. With $\tau = 1.8$ ms, a $T = 2$ ms is considered to be an appropriate reversal time. This choice however limits the repetition frequency to 500 Hz ($T_r = 2$ ms). The effect of the reversal time on the displacement amplitude A of the focus point and the contrast C of focalisation is experimentally investigated in this section.

Influence on the amplitude A A range of reversal times T are tested with driving signals of the modulated filtered type. The measured displacement amplitudes A are plotted in Figure 4.12. The amplitude increases with T and tends to stabilise at a value of 2.95 µm. A function $f(t) = A_f(1 - exp(-\tau_A \cdot t)$ is fitted to the curve. The fit gives $A_f = 2.95$ and $\tau_A = 1.09$. It is common to consider a $5 \times \tau_A$ time to reach 99.3 % of the maximum value of the curve. Here $5 \times \tau_A = 5.45$ ms. To get the maximum amplitude for each focalisation, a minimum of 5 ms reversal time should

be used, resulting in a maximum 200 Hz repeating frequency. On the other hand, a 2 ms reversal time generates a 2.66 µm peak (90% of the maximum amplitude). This value is considered to be a good compromise for both the repetition frequency (500 Hz) and the amplitude (90 % of the maximum amplitude achieved). Note that if a 1 kHz repeating frequency is required, the amplitude drops to 2.03 µm in this case (only 69% of the maximum amplitude).

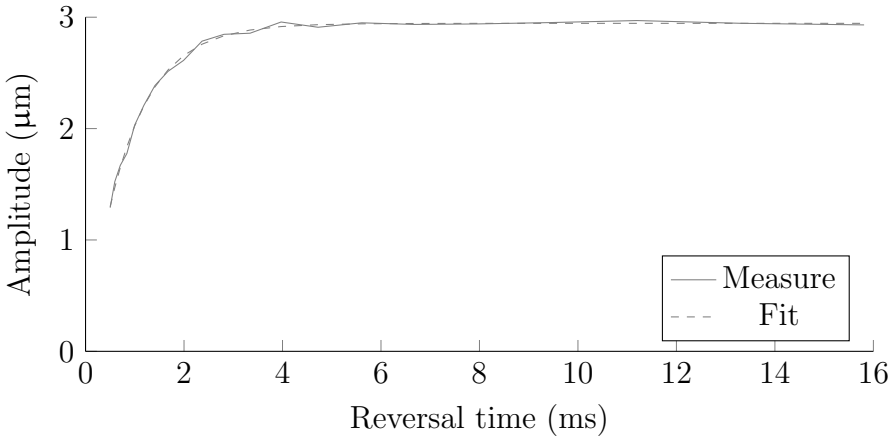

Figure 4.12: Displacement amplitude A of the focus point as a function of the reversal time T.

Influence on the Contrast The reversal time T also affects the signal-to-noise ratio, called contrast C. In order to measure the contrast, the displacement amplitude A at the focus point at the focalisation time $t = T$ should be compared to the vibration level (noise) on the whole surface. This would require a large number of vibration amplitude measurements distributed along the whole surface. In [38], the noise level is determined by measuring the RMS amplitude of the focus point during a time window such as $t \neq T$, while $t \leq \tau$. The noise level is therefore estimated on a 0.5 ms window beginning 25 µs after focalisation time T (see Figure 4.13). Here the driving signals are of the modulated non-filtered type.

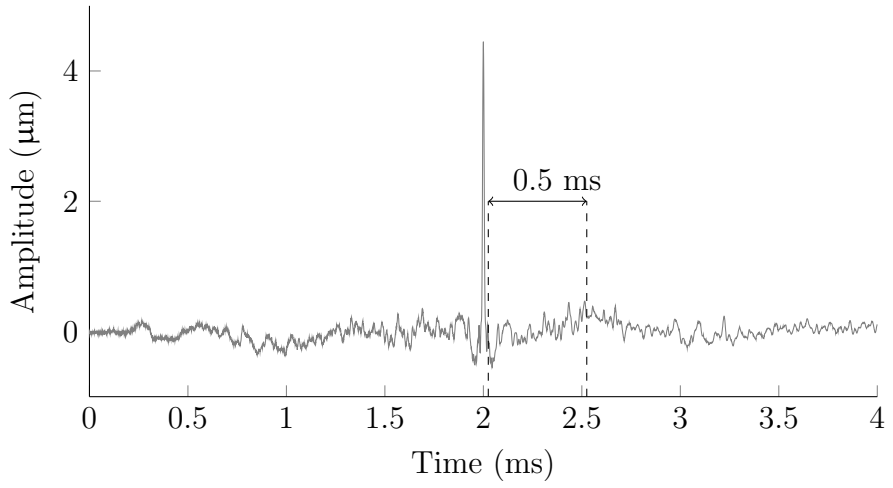

Figure 4.13: Amplitude at focus point and time window for noise level estimation.

Figure 4.14 shows the contrast C measurements for different reversal times T. Below a 2 ms reversal time the contrast drops significantly, from 29 to 14. This is explained by the fact that, as the attenuation constant is 1.8 ms, the induced vibrations by the focalisation process are not yet dissipated when the next focalisation occurs. This results in a poor signal-to-noise ratio. Above 2 ms the contrast increases up to 31 and then saturates. To maintain a high contrast, the reversal time should not drop below 2 ms, limiting the time reversal process on this plate to a frequency of 500 Hz.

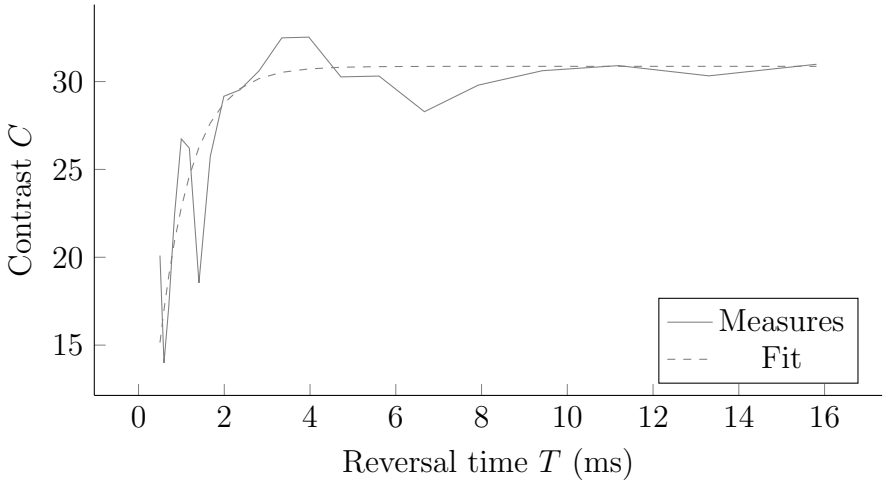

Figure 4.14: The contrast C as a function of the reversal time T.

In order to guarantee simultaneously large amplitudes (see Figure 4.12) and high contrasts (see Figure 4.14) a 2 ms reversal time T is a good choice. All measurements in this chapter are based on this value.

4.3.2 Displacement amplitude A

First the displacement amplitude A at the focus point is measured for the four driving signal types (presented in Table 4.2). The focalisation is at point 0, the plate's center. The influence on the displacement amplitude using different input signals: the quantification one one bit (1b), the Sigma-Delta modulation (SDM) and filtering the audio band is studied here, with a constant applied voltage (60 Vpp).

The first driving signal used is 1b non-filtered. The time-reversed impulse responses are quantified on one bit and no audible frequency filtering is applied ($0 - 125$ kHz band). The displacement amplitude measurements are presented in Figure 4.15. A peak displacement amplitude at the focus point of 13.86 µm is measured. Figure 4.15a indicates the vibration amplitude at point O as a function of time during the focalisation process. Figure 4.15b is a zoom at the focusing time, showing the temporal resolution, here measured at 9.8 µs. The amplitude gradually increases and at $t = T$ (2 ms), a peak is measured. Two side lobes before and after the peak are observed. They have a negative sign compared to the main lobe. The ratio between main lobe and first side lobe is 10. The next side lobes, before and after the focalisation, are much less significant.

The second driving signal is 1b filtered ($25 - 125$ kHz band, see Figure 4.16). The displacement amplitude drops to 9.70 µm which is a 30 % drop (see Figure 4.16a)

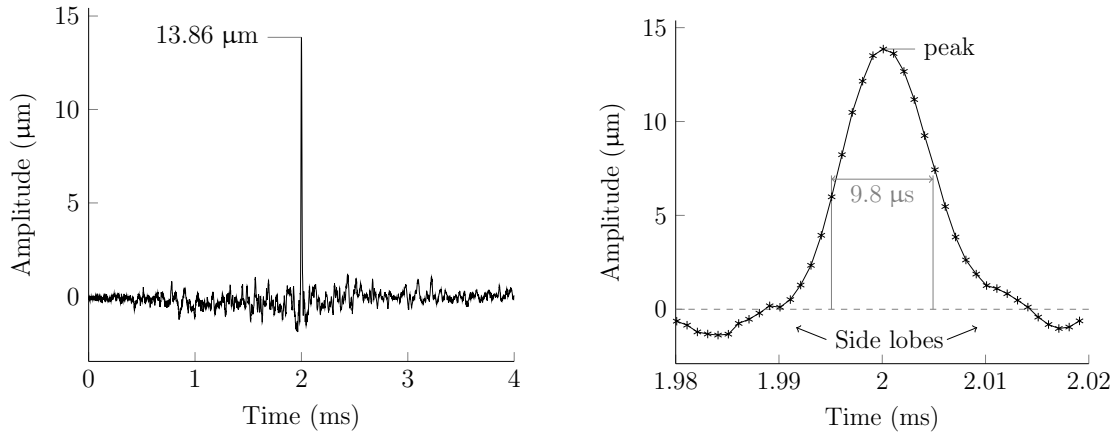

(a) Amplitude. (b) Temporal resolution.

Figure 4.15: Temporal characteristics of the focus point for 1b signals with no filtering

compared to the previous 1b non-filtered signal. As previously detailed in section 3.4.3, this is due to the fact that a significant amount of the wave energy is in the lower frequency part ($0 - 25$ kHz) of the driving signals. Due to the reduced bandwidth (from $0 - 125$ kHz to $25 - 125$ kHz), the mean frequency is shifted upwards (from 62.5 kHz to 75 kHz) resulting in a smaller temporal resolution, at 6.9 µs. Another effect resulting from the audible frequency band filtering is the greater negative deformation of the side lobes, due to the absence of low frequency components in the filtered signal (see Figure 4.16b). The ratio between main lobe and first side lobe decreases to 2.1. The addition of lower frequencies evens out this deformation, as can be seen in Figure 4.15b.

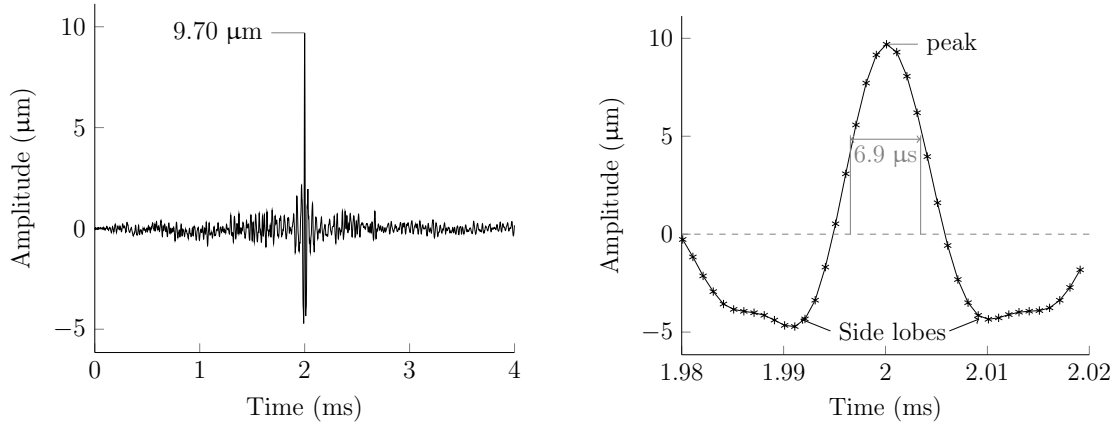

(a) Amplitude. (b) Temporal resolution.

Figure 4.16: Temporal characteristics of the focus point for 1b signals with filtering

The SD modulation process is used instead of the one bit quantification process, to generate the driving signals without audible band filtering ($0 - 125$ kHz band). It generates a much lower amplitude at the focus point, as shown in Figure 4.17. The displacement amplitude (4.45 µm) drops by 68 % when compared to the 1b non-filtered signals (see Figure 4.17a). The temporal resolution is 9.2 µs, (see Figure 4.17b), which is similar to the 1b non-filtered measurement. The ratio between

main lobe and first side lobe is 13.5.

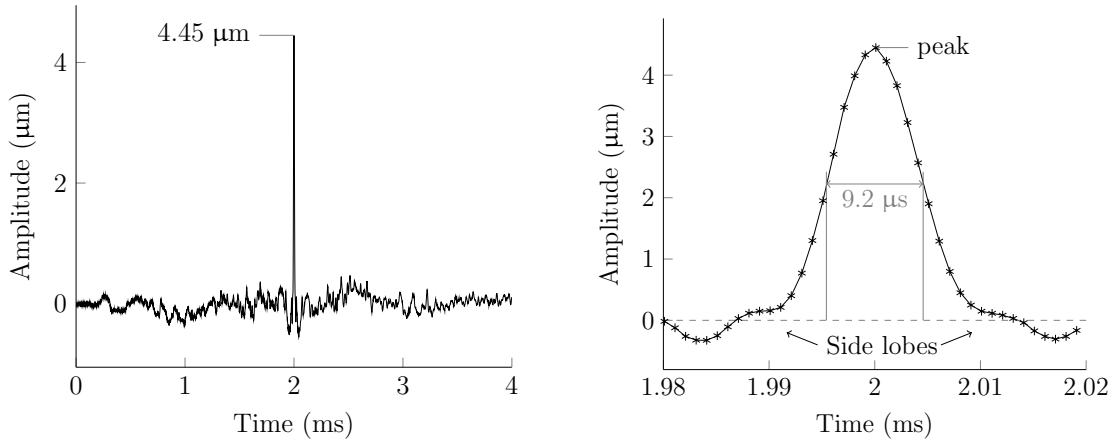

(a) Amplitude. (b) Temporal resolution.

Figure 4.17: Temporal characteristics of the focus point for SDM signals with no filtering

Filtering the audible frequencies out of the signals generated by the SD modulation ($25 - 125$ kHz band) results in a further drop in amplitude at the focus point, as shown in Figure 4.18. The amplitude is now 2.71 µm, which is a further 40 % drop compared to the unfiltered SDM signals (see Figure 4.18a). Compared to the 1b filtered signals, it is a 72 % drop. The temporal resolution is 6.6 µs (see Figure 4.18b), which is similar to the 1b filtered measurement. The same shift in mean frequency results in the same temporal resolution change. The ratio between main lobe and first side lobe is 2.5.

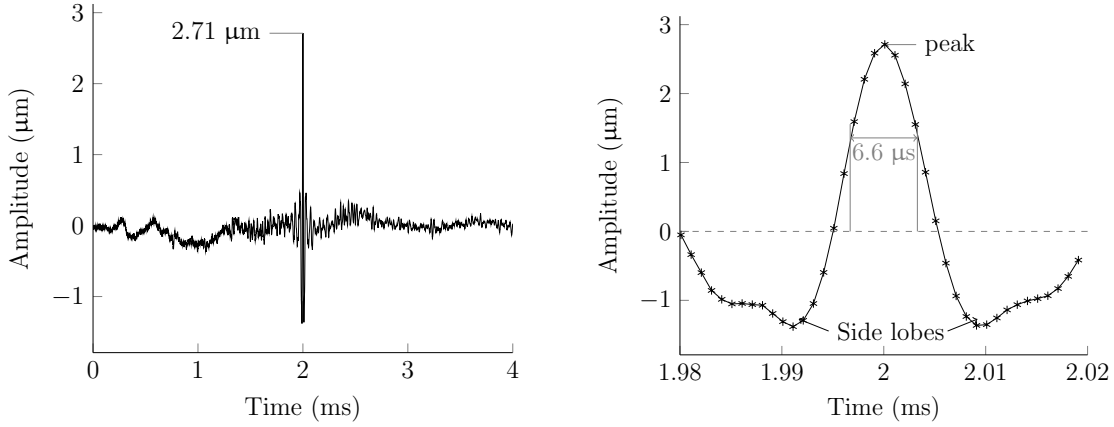

(a) Amplitude. (b) Temporal resolution.

Figure 4.18: Temporal characteristics of the focus point for SDM signals with filtering

Based on the amplitude measurements, the switch from 1b to SDM signals results in an amplitude drop of about 70 %. The filtering of audible frequencies represents a further drop of 30 % to 40 %. Studying the impact of filtering out the audible frequency band from the driving signals is still important as the noise emitted by the device (discussed in section 4.5) decreases with filtering.

4.3.3 Spatial Resolution R_s

To determine the spatial resolution R_s of the focus point for the different driving signals, a scan of the surface is carried out, around the same center point, O. The vibrometer records the vibrations on a 30 by 30 mm grid with a 1 mm step size. For each location, the amplitude at the focusing time is extracted and plotted on an XY plane to constitute the displacement amplitude map at focusing time. A section $A - B$ along the x axis is then considered. The width at half-height is measured to provide the value of the spatial resolution, R_s.

Figure 4.19 shows the displacement amplitude map and the $A - B$ section for the 1b non-filtered signals ($0 - 125$ kHz band). As the used driving signals are wide band, the shape of the deformation is circular. The spatial resolution is in this case 9.5 mm (see Figure 4.19b). In the spatial domain, as noted in the temporal domain in the previous section, the two first side lobes can be seen with negative amplitudes. The ratio between main lobe and first side lobe is 15.8.

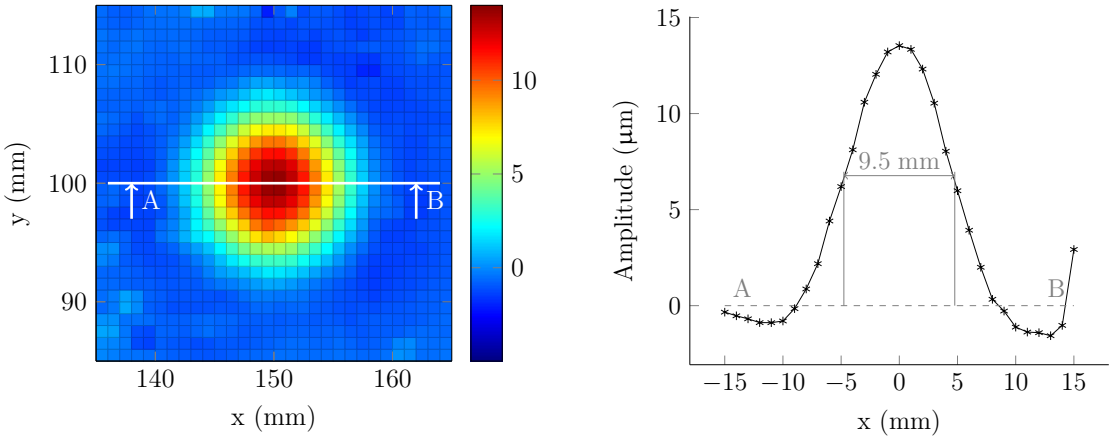

(a) Scan of the focus point.

(b) A-B section and spatial resolution.

Figure 4.19: Spatial characteristics of the focus point for 1b signals with no filtering

In Figure 4.20 the displacement amplitude map and the $A - B$ section for 1b filtered signals is presented ($25 - 125$ kHz). The spatial resolution is reduced to 6.4 mm (see Figure 4.20b), which is predicted by Equation 3.12. This reduction in R_s comes from the increase in the mean frequency of the driving signal, resulting from the filtering of the audible band (from 62.5 kHz to 75 kHz). The same behaviour as noted in the temporal domain is observed: the deformation in the spatial domain for the filtered driving signal also exhibits deeper secondary lobes than the non-filtered signals. This is due to the absence of low frequency components in the filtered signals. The ratio between main lobe and first side lobe is 3.5.

Figure 4.21 shows the displacement amplitude map and the $A - B$ section for the SDM signals without filtering ($0 - 125$ kHz band). The spatial resolution in this case is 9.2 mm (see Figure 4.21b). This result is similar to the one for 1b non-filtered signal as the mean frequency of the driving signals is the same in both cases. The ratio between main lobe and first side lobe is 16. The SDM driving signals exhibits however lower amplitudes as discussed the previous section.

In Figure 4.22 the displacement amplitude map and the $A - B$ section for SDM filtered signals is presented ($25 - 125$ kHz). The spatial resolution is 7.2 mm (see Figure 4.22b). This result is similar to the one for 1b filtered signal, as the mean

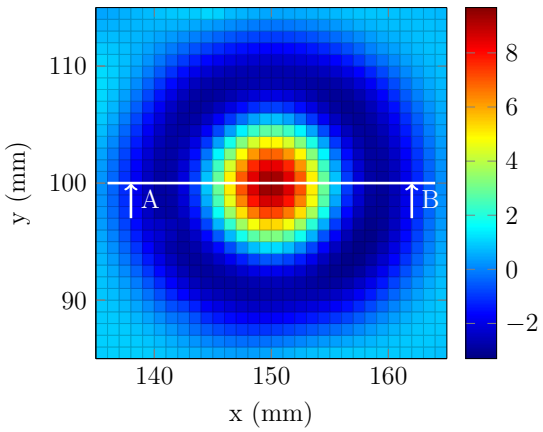

(a) Scan of the focus point.

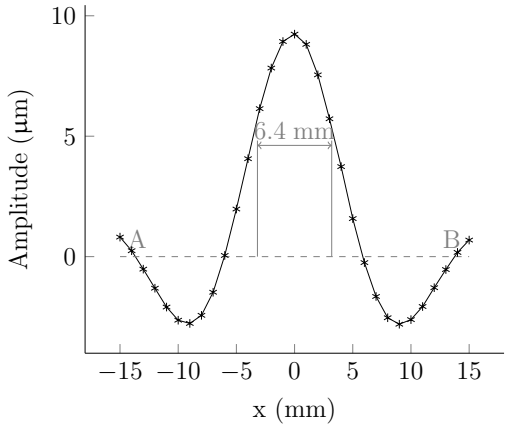

(b) A-B section and spatial resolution.

Figure 4.20: Spatial characteristics of the focus point for 1b signals with filtering

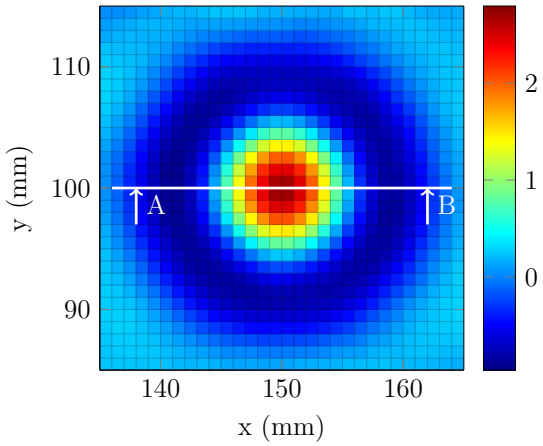

(a) Scan of the focus point.

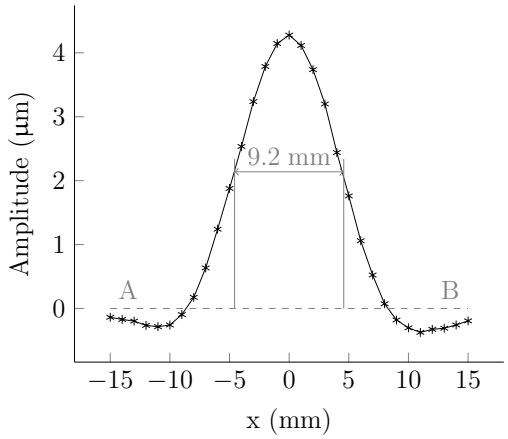

(b) A-B section and spatial resolution.

Figure 4.21: Spatial characteristics of the focus point for SDM signals with no filtering

frequency is the same in both cases (75 kHz). The ratio between main lobe and first side lobe is 3.3.

To verify the analytical model developed in subsection 3.4.1 on the 1.1 mm thick plate, spatial resolution measurements on 1 kHz wide band driving signals are carried out and are plotted in Figure 4.23. The different frequency intervals produced a point varying from 48.1 mm ($0-1$ kHz) to 6.4 mm ($74-75$ kHz), which is in good agreement with the proposed model and confirm the tendencies observed in section 3.4.3.

When the analytical model developed in subsection 3.4.1 is applied to the four driving signals, it results in:

- a spatial resolution of 5.74 mm for a mean frequency of 62.5 kHz, corresponding to the non-filtered signals (1b and SDM) and
- a spatial resolution of 5.24 mm for a mean frequency of 75 kHz, which corresponds to the filtered signals (1b and SDM).

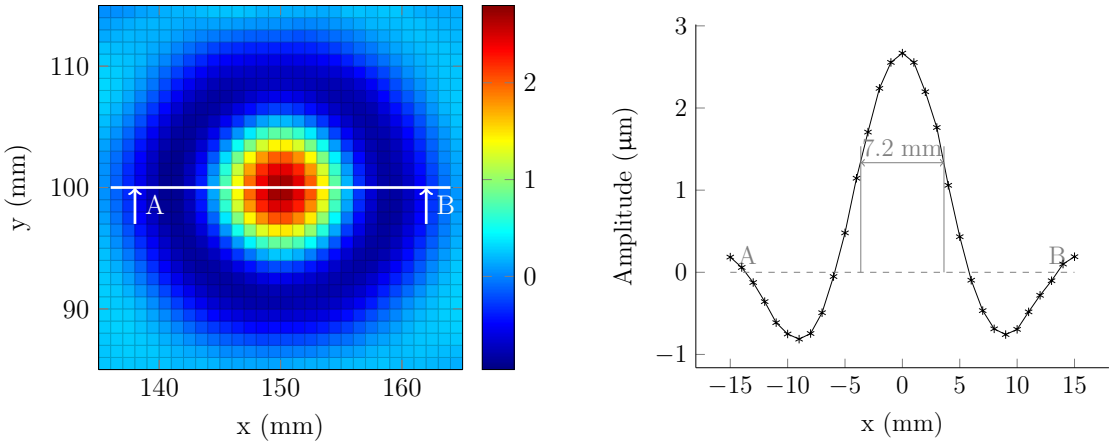

(a) Scan of the focus point.

(b) A-B section and spatial resolution.

Figure 4.22: Spatial characteristics of the focus point for SDM signals with filtering

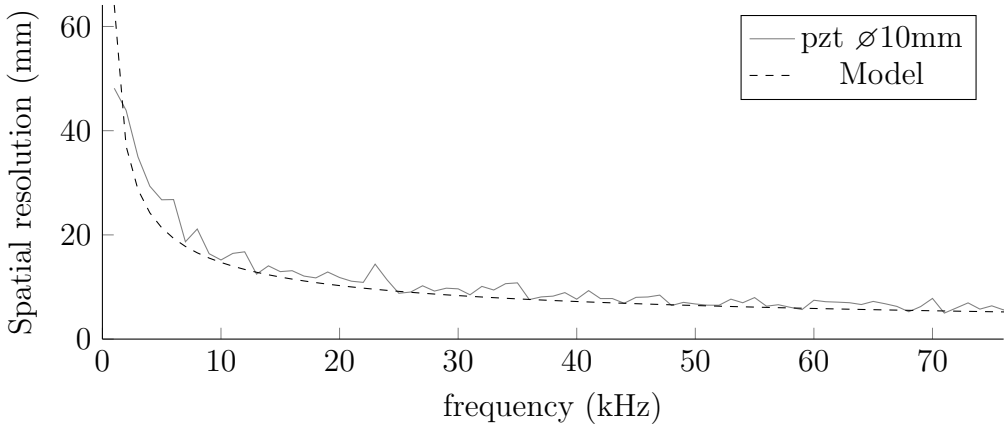

Figure 4.23: Model and measurements of the focus point's spatial resolution on a 1.1 mm glass plate.

The experimental measurements resulted in a spatial resolution R_s of 9.5 mm and 9.2 mm for non-filtered signals and 6.4 mm and 7.2 mm for filtered signals. Although slight differences between these measurements and the theoretical values exist, the models predictions are considered to be accurate enough to provide design guidelines.

4.3.4 Discussion

Table 4.3 sums-up the different measurements reported in this section, as a function of amplitude, temporal resolution, spatial resolution and contrast for the four driving signal types.

The 1b driving signals generate larger displacement amplitude than the SDM driving signals, as 1b (square wave signals) inject more energy in the plate. Filtering the signals decreases their amplitude, as filtering reduces the signal bandwidth and therefore less eigenmodes are excited to contribute to the focalisation. Overall, in terms of displacement amplitude, the 1b non-filtered drivings signal is the best choice, with A=13.89 µm.

Signals	1b non-filtered	1b filtered	SDM non-filtered	SDM filtered
Amplitude (µm)	13.86	9.70	4.45	2.71
Temporal Res (µs)	9.8	6.9	9.2	6.6
Spatial Res (mm)	9.5	6.4	9.2	7.2
Contrast	25.3	22.7	35.6	26.5

Table 4.3: Performance comparison in terms of Amplitude, Temporal and Spatial Resolution and Contrast for the four different driving signals.

Temporal and spatial resolution exhibit a similar behaviour, decreasing with the filtering of the driving signals. This is explained by the increase of the driving signals' mean frequency (from 62.5 kHz to 75 kHz) by the filtering process. SDM filtered driving signals produce the shortest focalisation with a temporal resolution of 6.6 µs, while 1b filtered driving signals produce the narrowest deformation, with a spatial resolution of 6.4 mm.

The SDM driving signals exhibit better contrast than the 1b driving signals. As 1b signals inject more energy in the plate, the overall vibration noise is more important than with SDM signals, which explains the lower contrast of the 1b signals. Non-filtered driving signals have a larger bandwidth than the filtered ones, which explains that the contrast of focalisation is higher when non-filtered driving signals are used. Overall, the SDM non-filtered signals produce the best contrast, at 35.6.

4.4 Energy consumption

In this section the electrical consumption of the prototype is investigated for the different driving signals. It should be noted that the power consumption measurements include the energy required to achieve the mechanical work, the energy required for addressing the piezoelectric transducers and the energy dissipated by the electronics.

4.4.1 Experimental measurements

The voltage drop (V_2 - V_1) across a resistor ($R_p = 2.1\ \Omega$) is measured to determine the current, as depicted in Figure 4.24. This is carried out for both power supply lines : the mosfet drivers (15 V) and the mosfets (60 V).

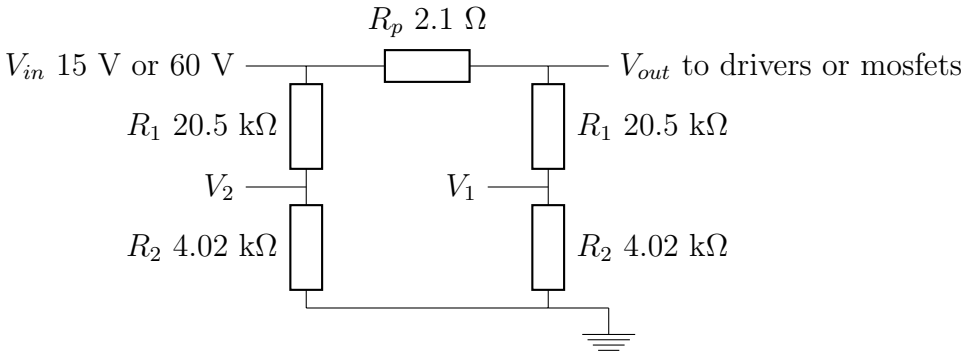

Figure 4.24: Electrical circuit for the consumption measurements.

A voltage divider is used for the measurements:

$$V_2 = V_{in}\frac{R_2}{R_1 + R_2} = V_{in}\frac{4.02}{4.02 + 20.5} = \frac{1}{6.1}V_{in} \tag{4.1}$$

$$V_1 = V_{out}\frac{R_2}{R_1 + R_2} = \frac{1}{6.1}V_{out} \tag{4.2}$$

The current I_p flowing across R_p is given by:

$$I_p = \frac{V_{out} - V_{in}}{R_p} = \frac{6.1(V_2 - V_1)}{R_p} \tag{4.3}$$

The power consumption P for both supply lines is therefore:

$$P = V_{supply} \cdot I_p \tag{4.4}$$

The following measurements are carried out when activating all 32 channels. When SD modulation is on, the drivers' consumption is 15 W and the mosfets' consumption is 25 W. Total consumption is 40 W, resulting in a 1.25 W consumption per channel. Adding the filtering to the modulated driving signal does not affect the consumption.

When 1b signals are used, the drivers' consumption drops to 5 W and the mosfets' consumption decreases to 18 W. Total consumption is 23 W, resulting in a 0.72 W consumption per channel. Adding the filtering to the 1b driving signal does not change the consumption.

1b signals consumption is about 43 % less than SDM signals. This is mainly due to the difference in switching frequency between 1b signals and SDM signals. In the case of 1b signals, the electronics is at most switching at 125 kHz, whereas the SD modulation is used with an oversampling to 4 MHz, which sets the switching frequency of the electronics (32 times higher switching frequency). As for the filtering stage, it is part of the computation process producing the driving signals and does not change drastically the average switching frequency of the driving signals.

Signals	1b non-filtered	1b filtered	SDM non-filtered	SDM filtered
Power (W)	23	23	40	40

Table 4.4: Power consumption for the different driving signals.

4.4.2 Analytical estimation

In order to get a better understanding of the power consumption measurements, an analytical estimation is proposed. The power flowing through the RLC_q filter is calculated, with C_q being the capacitance of the transducers, in order to approximate the power consumed by the transducers.

In the frequency domain, the power P is:

$$P(\omega) = \frac{1}{2}U(\omega)I^*(\omega) \tag{4.5}$$

where U is the voltage and I the intensity. The voltage U is also defined by:

$$U = ZI \tag{4.6}$$

where Z is the electrical impedance. Combining Equation 4.5 and Equation 4.6 gives:

$$P(\omega) = \frac{1}{2}\frac{U^*}{Z^*} = \frac{|U|^2}{2Z^*} \tag{4.7}$$

Taking the magnitude of P gives:

$$|P(\omega)| = \frac{1}{2}\frac{|U|^2}{|Z|} \tag{4.8}$$

For the RLC filter, $Z = R + \frac{1}{jC_q\omega} + jL\omega$, so:

$$|Z| = \frac{\sqrt{(1 - LC_q\omega^2)^2 + (RC_q\omega)^2}}{C_q\omega} \tag{4.9}$$

Combining Equation 4.8 and Equation 4.9 gives :

$$|P(\omega)| = \frac{|U|^2}{2}\frac{1}{\frac{\sqrt{(1-LC_q\omega^2)^2+(RC_q\omega)^2}}{C_q\omega}} \tag{4.10}$$

Introducing $\omega = 2\pi f$ leads to

$$P_{mean} = \frac{U_{mean}^2}{2}\frac{1}{\frac{\sqrt{(1-LC_q(2\pi f_{mean})^2)^2+(RC_q 2\pi f_{mean})^2}}{C_q 2\pi f_{mean}}} \tag{4.11}$$

With $U_{mean} = 30$ V, $C_q = 2.1$ nF, $L = 470$ µH, $f_{mean} = 75$ kHz, we get $P_{mean} = 0.31$ W per channel and for the whole 32 channels, $P_{mean} = 9.92$ W. This represents the theoretical energy consumed by the piezoelectric actuators and does not take into account the efficiency of the driving electronics. The consumption of a driving electronics for piezoelectric transducers depends on the power requirements. In commercially available products, the driving electronics can require two to ten times the energy required to drive the piezoelectric actuators. In our case the ratio is between 2 and 4, which points to a limited improvement margin.

To decrease the energy consumption, a driving electronics with a better efficiency could be designed. However, a larger consumption reduction is expected in finding a better compromise between the spatial resolution requirements and the chosen frequency band. Lower frequencies and narrower frequency bands would decrease the power consumption of the electronics. Fine tuning the coupling between the plate and the transducers would allow, for a constant deformation, to decrease either the number of transducers or the supply voltage. Those approaches can be envisioned as future improvements of the system efficiency.

4.5 Noise emission

Noise emissions are of critical importance for a haptic feedback system in direct interaction with the user. An ideal system would not emit any noise. In order to compare the different driving signal parameters, presented in Table 4.2, noise measurements are carried out while a focalisation at the center of the plate takes place. A sound level meter (model CA834 from Chauvin Arnoux) is used to record

the noise emissions. These measurements allow to compare sound emission of the presented system to commercially-available systems and characterise how users are affected, as sound level meters report units in dBA (A-weighted sound pressure level measures). These measurements take however into account a limited bandwidth, ranging from 37.5 Hz to 8 kHz. This does not take into account the full acoustic noise emission band of our device. However, it is useful to quantify the noise emissions in terms of human audition. In order to verify the filtering of the whole audible band, a second approach with complementary measurements using a calibrated microphone with a bandwidth ranging from 0 to 80 kHz is carried out.

4.5.1 Noise emission in dBA

The noise emission of continuous haptic feedbacks using time reversal at 500 Hz (T = 2 ms) are compared with the four different driving signals (audio band filtering enabled/disabled and SDM/1b). The sound level meter is placed perpendicularly to the glass surface at a distance of 20 cm. The ambient noise is measured first and found to be at 42 dBA. The measures are shown in Table 4.5.

Signal at 500Hz	SDM	1b
no filter	76 dBA	80 dBA
filter	73 dBA	77 dBA

Table 4.5: Noise emission of the different driving signals in dBA.

The unfiltered 1b signal reaches a noise level of 80 dBA. SDM reduces the sound pressure level by 4 dBA and the filtering of the audio bandwidth further reduces the sound pressure level by 3 dBA.

From the previous sections, it has been shown that the SD modulation represented a drop of around 70% in terms of amplitude at the focusing point. This represents a factor of 3.3. The drop in dBA is 4 dBA, which represents a factor of 2.5 in terms of sound pressure level. This means that the SD modulation reduces the noise emissions in a less significant way than it reduces the amplitude of the impact. It can be concluded that it is not an efficient approach for noise emission reduction. Furthermore, it was shown that filtering represented a drop of around 30 to 40% in terms of amplitude at the focusing point. This is a factor of 1.4 to 1.7. The drop in dBA was 3 dBA, which is equivalent to a drop of a factor 2 in terms of sound pressure level. This means that filtering reduces the noise emissions more than it reduces the amplitude.However, even when filtering the $0 - 25$ kHz band the noise emissions are well above the ambient noise level. To investigate the noise emissions in the frequency spectrum, further measurements are presented in the next section.

4.5.2 Wide bandwidth sound level measurements

In this section the noise emissions are measured using a calibrated microphone (378C01-C from Piezotronics) with a $5 - 80,000$ Hz bandwidth, connected to a conditionner (482C54 from Piezotronics). The signals' amplitude are measured and plotted normalised along the whole bandwidth taken into account. The frequency domains of the 4 signals are shown in Figure 4.25.

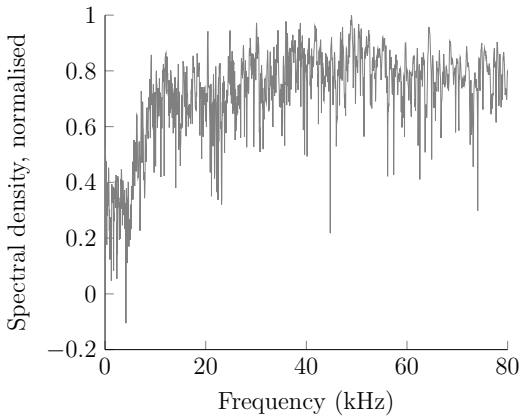

(a) FFT of the 1b non-filtered focalisation.

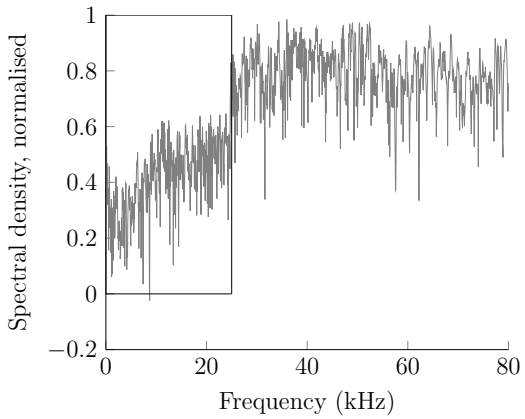

(b) FFT of the 1b filtered focalisation.

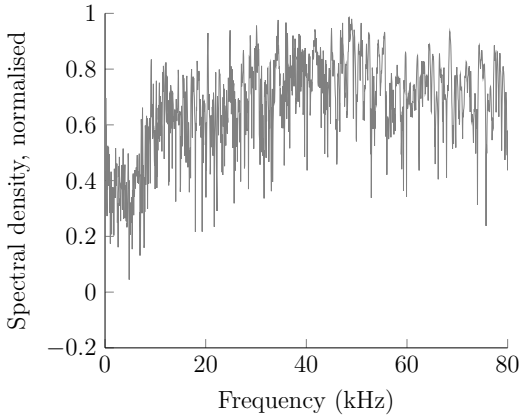

(c) FFT of the SDM non-filtered focalisation.

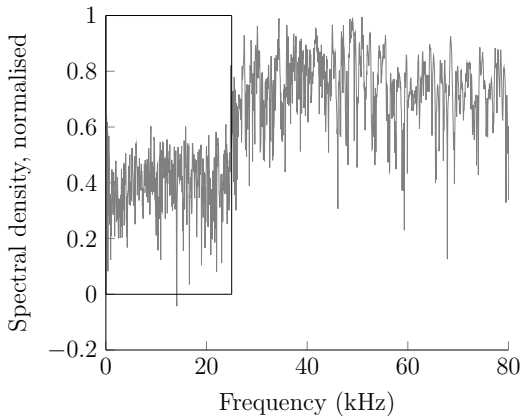

(d) FFT of the SDM filtered focalisation.

Figure 4.25: $0 - 125$ kHz FFTs of the noise emissions for the four driving signals.

The effect of the filter is clearly visible when comparing Figure 4.25a to Figure 4.25b and Figure 4.25c to Figure 4.25d, with a significant drop in frequency amplitude before 25 kHz. However, the amplitudes measured in the audible band are still important (around half of amplitude for frequencies in the $25 - 80$ kHz) and well above zero. The next section investigates in detail this effect.

Effect of filtering

Figure 4.26 is a zoom of Figure 4.25 for a limited frequency range ($0 - 25$ kHz). Figure 4.26a compares the effect of filtering on the SDM driving signals. In the $0 - 6$ kHz band the noise level is quite similar for both signals, however the contribution of the filter is high in the $6 - 25$ kHz range. Figure 4.26b compares the effect of filtering on the 1b driving signals. In the $0 - 5$ kHz band the noise level is quite similar for both signals. The added value of the filter in the $5 - 25$ kHz range is high.

Repetition and spectrum discretization

In Figure 4.27 the case of a single focalisation compared to a repeated focalisation is considered for a SDM non-filtered driving signal. The FFT on the $0 - 5$ kHz of a

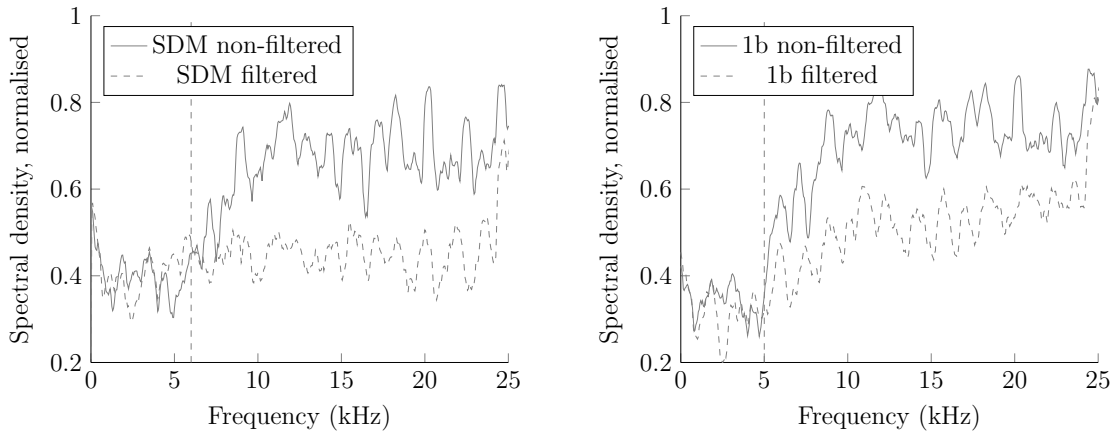

(a) SDM signals.

(b) 1b signals.

Figure 4.26: Comparison of the FFTs of the filtered and non-filtered signals.

single focalisation is plotted against the FFTs of its 500 Hz repeated counterpart. On the FFT of the repeated signal, a peak every 500 Hz is observed. This corresponds to the repetition frequency and its harmonics. Therefore, it is clear that the repetition rate (here 500 Hz) will add noise in the audible band. Ideally the repetition rate should be above 20 kHz in order not to add any noise. However, in practice and as discussed in subsection 4.3.1, the repetition rate is limited to 500 Hz. Above 500 Hz, the amplitude at the focus point decreases exponentially, as previously shown in Figure 4.12. At 1 kHz ($T = 1$ ms), the amplitude is 69 % of the maximum amplitude and at 2 kHz ($T = 0.5$ ms), the amplitude drops to 44 % of the maximum amplitude.

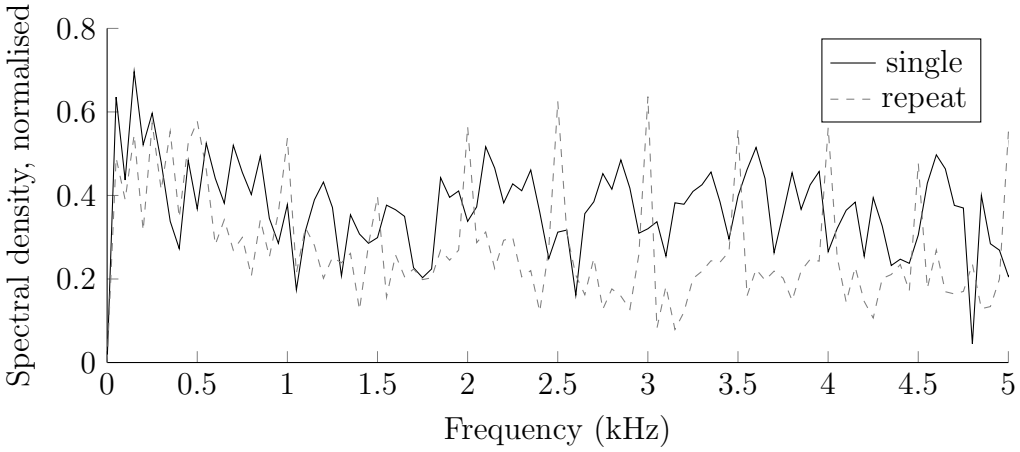

Figure 4.27: SDM non-filtered signals.

4.6 Variability and integrability

In this section, the contribution of each transducer to the focalisation process is investigated. Is there a relationship between the focus point and the distance from each transducer? Do all the transducers have the same contribution to the generated amplitude at the focus point? These questions are answered in the following section.

4.6.1 Transducers' location and generated amplitude

In order to study the effect of the transducer's location, a series of 12 points are chosen as focusing location, as shown in Figure 4.28. The points are taken along a rectangular shape as an inside contour of the plate. For each of the 12 points, the focusing process is carried out 32 times, once with each transducer independently. Each time the displacement amplitude A of the focus point is measured.

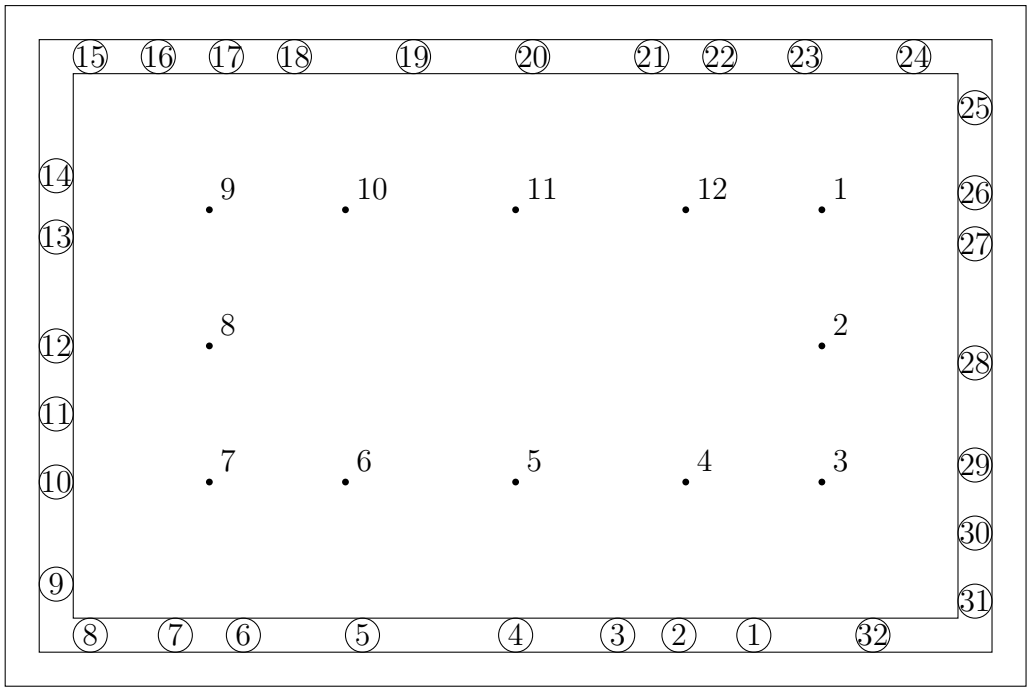

Figure 4.28: Transducers positions and focus points' locations on the prototype.

Contribution to the focalisation process

For each point the 32 amplitude measurements are averaged and plotted on Figure 4.29. The mean value for the generated amplitude is 0.155 µm. Each transducer generates an amplitude between 0.130 µm and 0.180 µm.

In Figure 4.30, the number of transducers contributing to the focalisation is varied between 1 and 32. The increase in displacement amplitude is linear. The higher the number of transducers Q, the higher the displacement amplitude A at the focus point.

Influence of the transducer's position

In order to determine whether there is a dependency between the generated displacement amplitude A at a specific point and the transducer position, the transducers are grouped in four subsets. The "bottom" subset includes the transducers n_1 to n_8 plus the n_{32}, the "left" subset includes the transducers n_9 to n_{15}, the "top" subset includes the transducers n_{16} to n_{24} and the "right" subset includes the transducers n_{25} to n_{31}. The amplitudes generated at each of the twelve selected locations are averaged for each transducer subset and plotted in Figure 4.31.

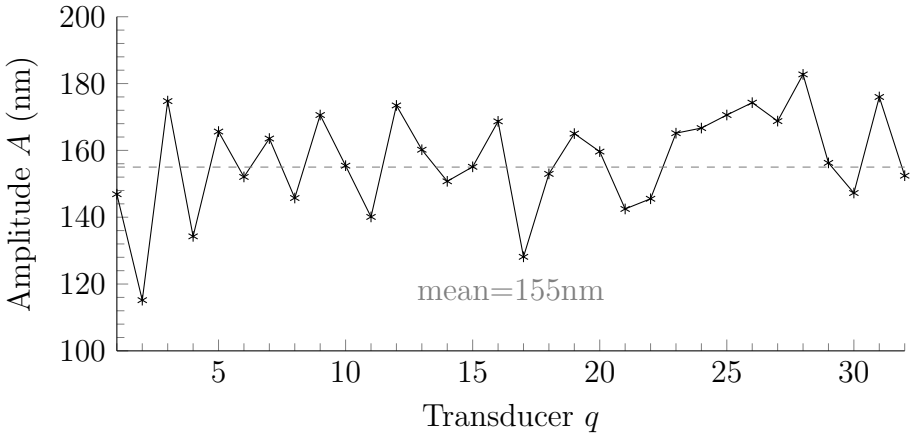

Figure 4.29: Mean displacement amplitudes A generated by each transducer independently.

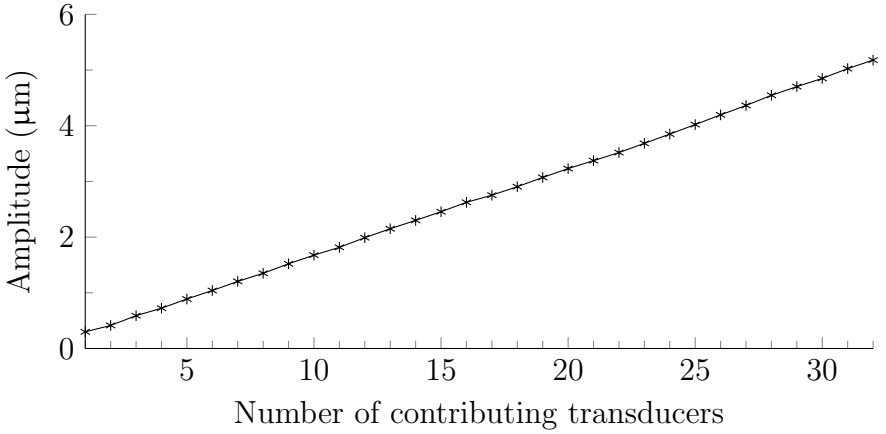

Figure 4.30: Displacement amplitude A as a function of the number of transducers Q used in focalisation.

Points 8 to 12 exhibit a larger displacement amplitude than points 1 to 7 for each subset. On average, point 7 has the smallest amplitude. To determine whether the distance between transducer subsets and focus point location influences the displacement amplitude, let's consider point 2 and point 8. The transducer subset the further away from point 2, and point 8 respectively, are the left one, and the right one. For point 2 the left subset gives a slightly better amplitude (+3% compared to the right one) even if it is further away from the point. For point 8, it is the right one, even if it is also the further away (+27 % compared to the left one). In average the bottom subset seems to be slightly less efficient than the others. One explanation could be a less efficient mechanical coupling between the copper band on which the transducers are glued and the glass substrate.

No impact or direct correlation between the focus point location and the actuator subset can be found. Therefore, there is no need for equal distribution on the sides of the plate to get a good focalisation process. For better integration purposes, the 32 actuators could be located on only one side of the plate without deteriorating the focalisation process, as shown in Figure 4.32. To fit on a single side the 32 transducers are chosen as squares of 9 by 9 mm^2, which represents the same active

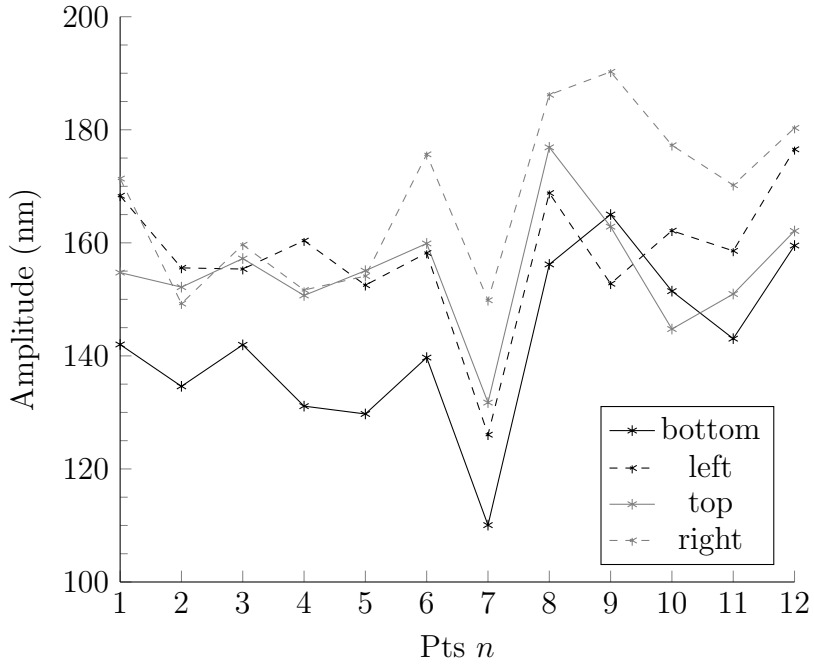

Figure 4.31: Mean amplitude for each focus point by transducers subset.

area as circular transducers of ⌀10 mm. Instead of using 17 % of the interactive surface for the transducers (copper band included), the new arrangement reduces the interactive area only by 4.3 %.

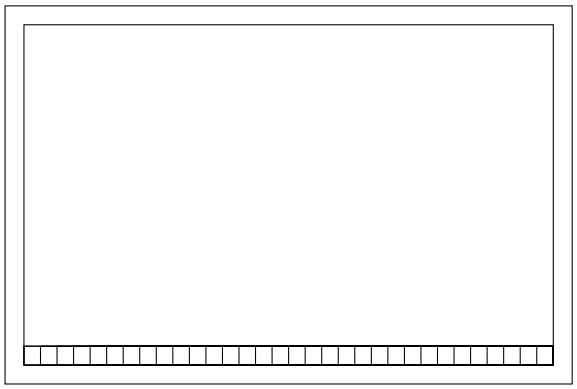

Figure 4.32: A prototype with 32 square transducers located on one side of the plate.

4.6.2 Focus point's location and spatial resolution

As shown in Figure 4.33, focusing is carried out on different locations : in the plate's corner (1), on one side (2), on the inside of the plate (3) and in the center (4). The focalisation is achieved with the 32 transducers. The spatial resolution scans are superimposed on the focus point's locations.

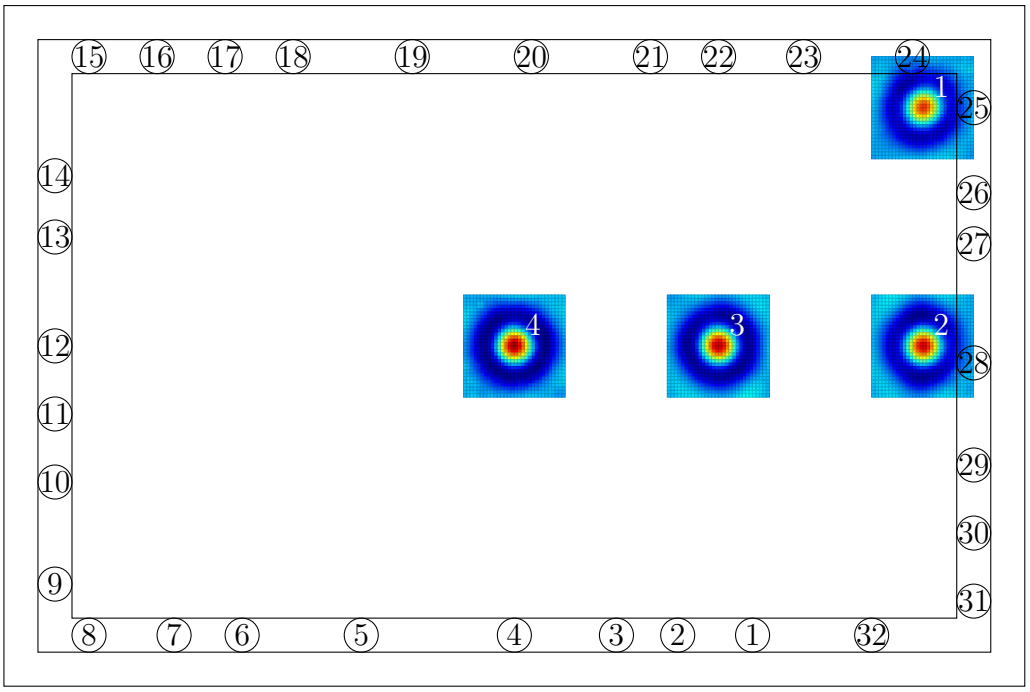

Figure 4.33: Prototype and transducers, with focus point locations.

Distribution across the plate

The spatial resolution is measured for each focalisation location. Figure 4.34 shows that the spatial resolution is almost constant at 7 mm ± 0.2 mm. This means that the spatial resolution does not change whether the focusing is achieved on the sides or inside the plate. The focusing in terms of amplitude and spatial resolution is homogeneous across the plate.

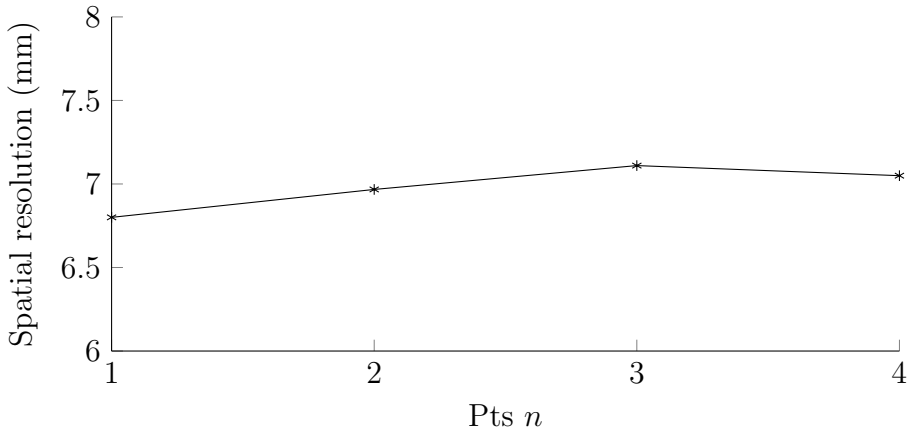

Figure 4.34: Spatial resolution of each focus point.

4.7 Conclusion

In this chapter a new tactile display implementing the time reversal approach is presented and characterised. It is based on a 1.1 mm thick glass substrate of an area of 300 by 200 mm^2. 32 piezoelectric transducers are glued on the periphery.

Dedicated electronics based on the class-D amplifier principles is used to drive the transducers. Four types of driving signals are presented and compared in terms of generated amplitude, resolution, energy consumption and noise emission.

Filtering the audible frequencies out of the driving signals proved to be an interesting noise emission reduction strategy. The use of a Sigma-Delta modulation of the second order, however, appeared to be less efficient and resulted in a greater loss of amplitude than sound emission reduction. Moreover, generating modulated driving signal requires a higher energy consumption than for driving signals quantified on 1 bit. The best choice in terms of driving signals is therefore filtered signals quantified on 1 bit.

It is has been demonstrated through experimental measurements that there is no substantial impact or direct correlation between the focus point's location and the transducers' location. This allows better integration designs. All the transducers could be located on one side of the plate without deteriorating the focalisation process. The spatial resolution and the amplitude were measured and appeared to be constant all over the plate's surface.

In the next chapter we will use this newly designed prototype to study how the focus spot is perceived by the user.

Chapter 5

Time Reversal and perception

5.1 Introduction

The previous chapter introduced a new tactile display implementing the time reversal method. Its performance in terms of generated displacement amplitude improved upon the state of the art. Decreasing the thickness of the glass surface, while using a better piezoelectric material and an improved electronics, enabled to develop a sturdier prototype with increased performances. Nevertheless, the performance still needs to be qualified in terms of human perception. What happens to the impact's amplitude when the user applies a force on the surface, whether it is exactly on the focus point or elsewhere on the surface? Is the resulting displacement amplitude still perceived by the user?

In section 5.2, the influence of the force with which the user presses on the screen on the generated impact is investigated. Then, in section 5.3 the relation between the impact's amplitude and the user's perception is studied. The displacement amplitude detection threshold is determined as a function of the applied force. Finally, in section 5.4 a perceptual study using different impact patterns is carried out. The patterns are compared in terms of both clarity and pleasantness.

5.2 Time reversal and sensitivity to applied force

On a smartphone, interaction with more than two fingers is almost non-existent. However, the size of the haptic screen, the number and size of finger contacts can vary. For example, on a tablet or a multimedia table, interactions may involve several users. Therefore, a large number of simultaneous fingers, fists or palm contacts, are common. When a contact is applied on a time reversal screen in any location, part of the flexural waves are absorbed by the finger and another part is diffracted. If the contact is at the focusing point, the mechanical coupling between the finger and the plate results in a damping effect that decreases the amplitude of vibrations. The size, number and location of contacts influence the focalisation process and thus, the displacement amplitude. Therefore, the effect of contact areas (at the focus point and elsewhere on the surface) on the displacement amplitude A generated by the time reversal is studied.

Previous work [40] studied the influence of the finger's contact on the surface on the time reversal process. In [40] the influence of finger contacts outside of the focalisation point is predicted using the theory of multiple diffraction [72] and measured experimentally. The fingers' contact on the surface creates a loss in the impact's amplitude of up to 30 % for a reversal time of 3 ms with three fingers in contact with the surface, outside of the focalisation point. However no measurements of the loss as a function of applied force are carried out. A finger applying a 1 N force at the focus point resulted in a 60 % loss in displacement amplitude at the focus point, for a 0.5 mm thick plate of an A5 format. A model of the finger is developed based on a standard mass-spring-damper system. The physical parameters of the finger are then estimated. This allows to compute an optimum for the plate's thickness, which is 0.88 mm, for a plate material of $\rho_s = 2510\,\mathrm{kg}\cdot\mathrm{m}^{-3}$ and an A5 screen surface.

In the next section the influence of different contacts' surface and location on the displacement amplitude are measured.

5.2.1 Experimental set-up

In this section the loss in displacement amplitude with several types of contacts is measured. Figure 5.1 presents the measuring set-up. The time reversal prototype, presented in section 4.2, is resting on two load sensing units on its sides. Averaging both signals gives the force which is applied on the plate. Focusing is done continuously and the generated amplitude is measured thanks to a laser vibrometer. The laser beam is directed towards the backside of the surface with a mirror positioned at 45°. The front side of the surface is free to explore and forces can be applied with the finger without disturbing the measurements.

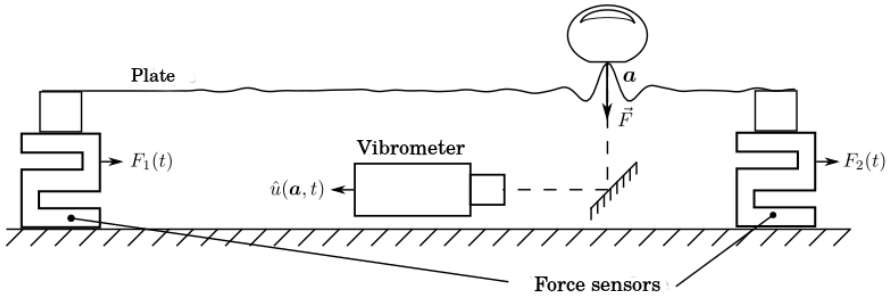

Figure 5.1: Haptic surface with force sensors and laser vibrometer.

For each measured point, a finger is pressed on a chosen location, either at the impact's location or away from it. At each impact a measurement of the applied force on the surface is carried out. This set-up allows to study the amplitude of the impact as a function of the applied force.

Contact force induced diffraction

A finger's contact on the surface at point P_1 introduces a local variation of the plate's impedance, leading to diffraction of the incidental waves. Measurements of the losses due to diffraction are carried out at the focalisation point F while applying force at point P_1, as shown in Figure 5.2.

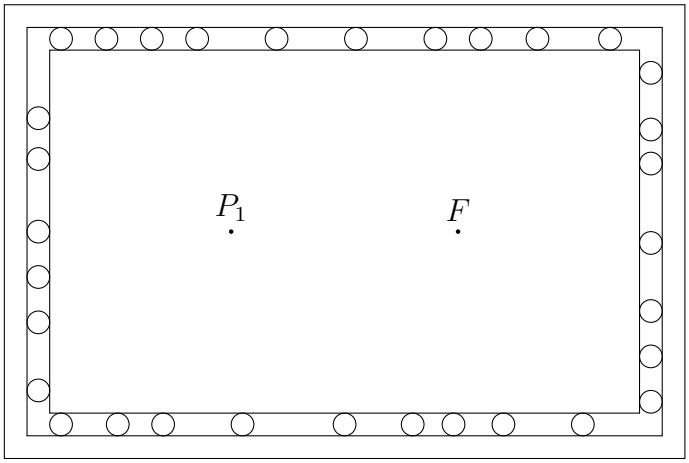

Figure 5.2: Focus points' location (F) and contact location (P_1).

Diffraction depends on the effective surface of the object applied to the surface. Different contacts are applied to the screen to study the effect. Centered around

point P_1, 1 finger, 5 fingers, a fist and a palm are applied successively, as shown in Figure 5.3.

(a) Five fingers press. (b) Fist press. (c) Palm press.

Figure 5.3: Different contacts pressed on the haptic screen.

Measurements are presented in Figure 5.4. The displacement amplitude is plotted as a function of the applied force when pressing on point P_1. The measurements are normalised to indicate a percentage loss. Applying a 2 N force with one finger on P_1 results in a 6 % loss in amplitude. Applying a 2 N force with five fingers around P_1 decreases the amplitude by 12 %. The drop is slightly less with a fist, around 10%. The five fingers and the fist contacts exhibit similar behaviour. However, applying a 2 N force with the palm of the hand around P_1 decreases the amplitude by 17 %. The palm contact area with the screen is larger than the previous cases which can explain the higher attenuation.

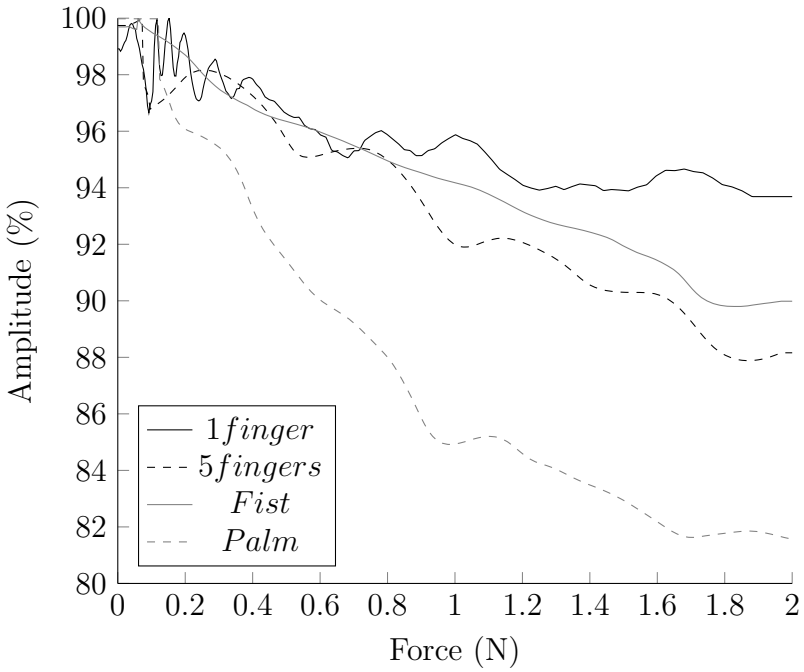

Figure 5.4: Loss of amplitude as a function of applied force for different contacts, at P_1.

The loss in amplitude due to contacts outside of the focalisation point increases with both the applied force and the contact area.

Amplitude loss due to an applied force at focus point

After quantifying the diffraction losses, measurements are carried out to estimate the losses due to the applied force by the finger at the focalisation point. The amplitude is measured with the laser vibrometer while the finger presses on the focalisation point and results are shown in Figure 5.5. A decreasing exponential curve is fitted on the measurements. Measurements are carried out during both the loading phase, when the finger presses on the surface, and the unloading phase, when the finger releases its pressure from the surface. A hysteresis effect is observed. The finger stiffness depends on the loading/unloading conditions and the related contact area affects the amplitude accordingly, as shown in Figure 5.5.

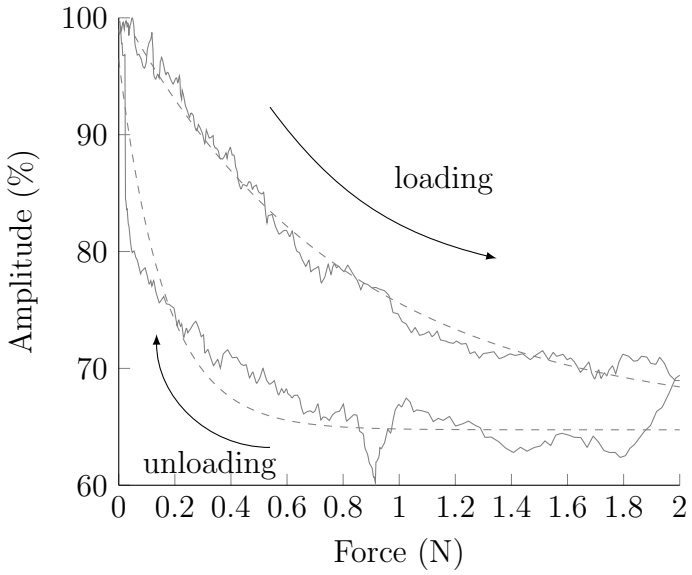

Figure 5.5: Drop in amplitude when a finger is pressing on the focus point F.

When a finger applies a 2 N force at the focus point, the impact's amplitude drops by 30 %. A 1 N force decreases the amplitude by 25 %.

5.3 Detection threshold

The previous section highlighted that the contact of a finger on the plate at the focusing point decreases the generated impact amplitude. In this section, the amplitude level required for the user to be able to perceive the impact is determined. Furthermore, the variation of the amplitude detection threshold with the applied force is investigated.

5.3.1 Parameters

Physical buttons usually click at 1 N or lower [12]. Haptic buttons designed with time reversal methods should mimic their physical counterparts. A simple touch on a touchscreen is usually registered when it exceeds 0.1 N. In this study, it is proposed to divide the touch force in three equally large intervals (0.1 N - 0.4 N, 0.4 N - 0.7 N and 0.7 N - 1.0 N).

The second parameter is the amplitude of the impact. This one is controlled by the input signal voltage. The driving signals are of the 1b non-filtered type with a peak amplitude A of 12.9 µm. This peak value is 8 % less than the peak value of 13.86 µm obtained in subsection 4.3.2 for the same driving signals. This is explained by the fact that the haptic surface is now fixed onto the load sensors, changing the boundary conditions. Amplitudes below 50% are not perceived by a few pilot participants. Therefore five amplitude values are chosen between 50% and 100% equally distributed. 0% is added as a control value. The input voltage values are 0%, 50%, 62.5%, 75%, 87.5% and 100%, with 100% corresponding to the peak amplitude of 12.9 µm.

It is observed in section 5.2 that the displacement amplitude of the focus point is influenced by the applied force. To take this into account, the real generated amplitude is measured with the laser vibrometer for each press.

5.3.2 Experimental protocol

The experiment design gives 3 forces x 6 amplitudes = 18 conditions. Each condition is repeated 5 times, giving a total of 90 trials per participant. The experiment takes about 20 minutes per participant.

The experimental setup is presented in Figure 5.6. For each trial the participant is asked to press the screen at the haptic feedback location and to stabilise the applied force. The applied force is indicated in red and the upper and lower range limits (indicated by blue bars) guide the user to adjust the force within the limits. When the user stabilises the applied force within the indicated range for one second, the system generates one single impact. The participant indicates then, whether he/she felt the impact on his/her finger or not.

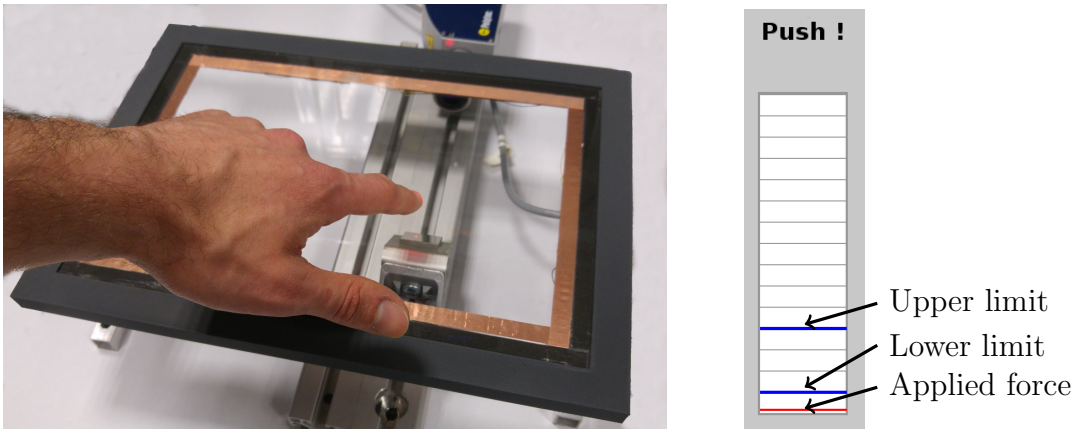

(a) Haptic screen, with a finger pressing at the focus point. (b) Force level.

Figure 5.6: The experimental set-up, composed of a time reversal haptic screen and a visual force level display in front of the user on a PC monitor.

After the experiment, each participant is asked to answer a few questions:

- How would you qualify the stimulus?
- For what kind of applications would you use this kind of haptic feedback?
- Do you have any further suggestions?

5.3.3 Participants

10 participants (6 Males and 4 Females with an average age of 25, SD 8.3, where 8 are right-handed) contributed to the study.

5.3.4 Results

Detection threshold

For each force range, the mean detection rate, averaged across participants, is shown in Figure 5.7 as a function of the impact amplitude. Each data point is reported with the standard deviation (Mean + σ and Mean - σ).

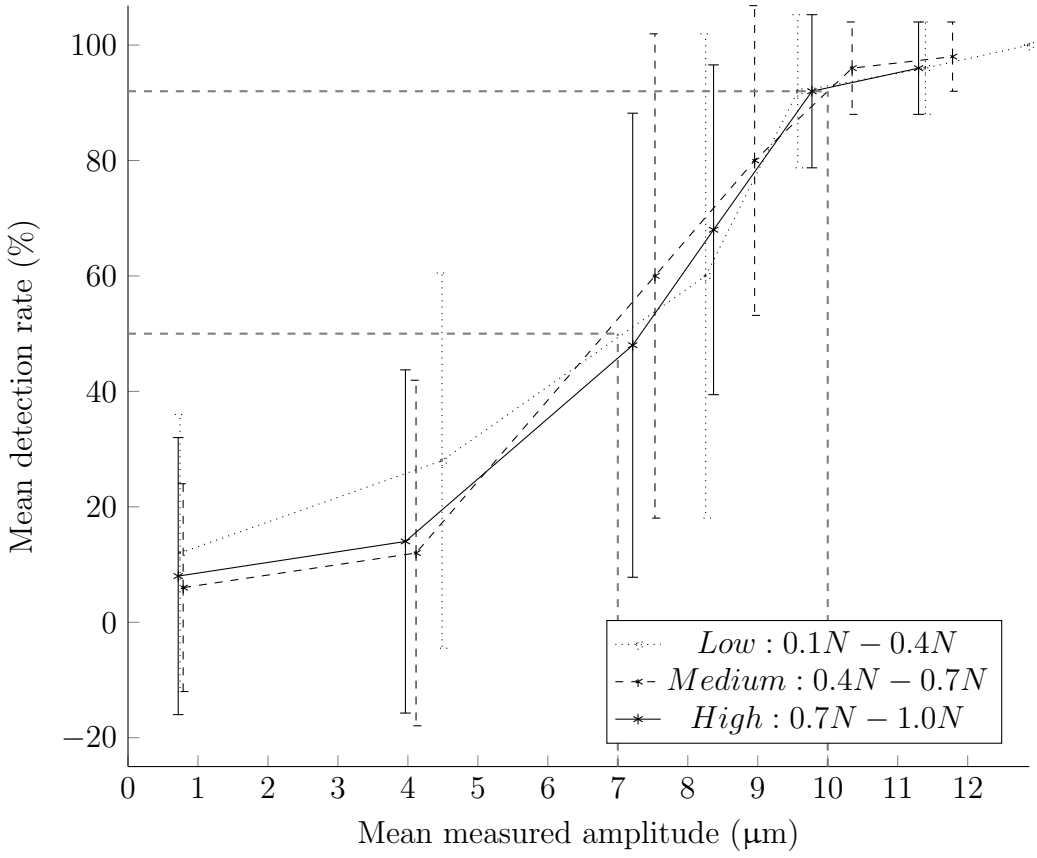

Figure 5.7: Mean detection rate as a function of mean measured amplitude.

A first observation indicates that the applied force does not significantly affect the detection threshold. For the specific panel of users, the detection threshold (generally given for a 50% detection rate) is around 7 µm. However the strong inter-participant variability illustrated by the large standard deviation, prevents to draw conclusions on a precise detection threshold. It is worth noting that at the lower applied force level, for the 100 % input signal (representing 12.9 µm), a 100 % detection rate is reached.

The participants were selected amongst the laboratory members, making the population non randomly chosen and non-representative. No extrapolation to the general population can be made at this point. It is however possible to propose recommendations for the amplitude requirements for future perceptual studies. The amplitude of the generated impact has to be at minimum 10 µm in order to be

detectable at various applied forces in the $0.1 - 1.0$ N range. Further studies on a wider randomly chosen population and a wider force range should be carried out to confirm the observed trends in this exploratory study.

Survey summary

A summary of the participants' feedback to the survey is provided in this section. The stimulus is often described as a pin, a prickling or a needle, seldom as a bursting bubble or a small electrical discharge. Moreover, it is not qualified as unpleasant or painful. However, it is rarely qualified as pleasant (only in the case where the stimulus is weak). The stimulus is perceived as local and brief. The pin sensation suggests that time reversal could be used to raise awareness or alert the user.

When asked what kind of haptic application they would imagine, the participants often cited button clicks. Others mentioned a relief information (tactile map, pin for a Braille interface) or a guiding information for visually impaired or disabled persons. Finally, another imagined application is rehabilitation, due to the strong induced vibration.

Future work should focus on the spatial and temporal shape of the impact. A less sharp localised feedback could prevent the needle feeling. A longer temporal signal could alleviate the problem of the short signal. In the next section the temporal modulation is explored.

5.4 Impact modulation and pattern perception

The previous study pointed out that the stimulus generated by time reversal is perceived as very localised and very brief. In this section, the temporal profile of the stimulation is addressed. Repeating the impact at a specific frequency while modulating the impact's amplitude would enable different haptic patterns.

5.4.1 Impact amplitude modulation

The use of the Sigma-Delta modulation allows to modulate the impact's amplitude by adding a gain to the driving signal. The different steps for the signal generation process, detailed in subsection 4.2.3 are as follows. The recorded impulse response is first cut to the reversal length and time reversed. It is then off-set and filtered. Then the sign is extracted and modulated. A gain is then applied (between 0 and 1) so that the modulation will give a correspondingly modified driving signal. To generate a pattern, the driving signal is repeated, while the gain is varied. The gain's variation along time is the modulation envelope.

5.4.2 Amplitude-modulated patterns

The maximum amplitude and the pattern duration are chosen to be fixed for all the patterns. The pattern envelope, which is the amplitude modulation with the time, is of crucial importance. In particular the repetition frequency has to be high enough so that the user perceives the signal's envelope as a whole and not as a succession of discrete impacts.

The pattern duration is of high importance. On the one hand, if too short, it is not possible for a human being to perceive the pattern. On the other hand, if the duration is too long, the pattern will not be appropriate for a click feedback and would be better suited for texture feedback. A compromise time of 100 ms is chosen, which corresponds to a common duration for patterns in haptic feedback systems [7], [48].

Two values are then compared for the repeating frequency. A frequency of 200 Hz corresponds to the optimum reversal time (5 ms in terms of amplitude generation, see subsection 4.3.1). The frequency is also quite near to the peak of sensitivity of human beings which is around 250 Hz [75]. However frequencies close to the peak of sensitivity are not perceived as pleasant by the users. A second frequency of 500 Hz is evaluated. It corresponds to the highest frequency with an impact amplitude still above the defined threshold of 10 µm, see (Figure 5.7). In order to compare the different patterns, the peak amplitude should be the same. As the displacement amplitude generated at a 200 Hz repetition rate is higher than at 500 Hz, a gain (in this case 0.6) is applied to the 200 Hz patterns. This enables to generate patterns with the same peak amplitudes.

Several pattern shapes, called P_n hereafter, are proposed, as shown in Figure 5.8. First, P_0 which is a single impact and previously used in the threshold experiment is tested. Three other envelopes are considered. A square one provides a pattern with sharp transitions for the beginning and the end of the pattern and a constant excitation amplitude. A cardinal sinus provides a smooth increase and decrease of the pattern's amplitude and reaches the maximum amplitude at the middle of the pattern. Finally a decreasing exponential function is tested for its sharp beginning and smooth decrease in amplitude along time.

5.4.3 Experimental protocol and participants

10 participants (6 Males and 4 Females with an average age of 25 among whom 8 are right-handed) took part in the study.

The experiment is conducted on the same prototype as the previous study, which performance is described in chapter 4.

The order in which the seven patterns are presented is chosen randomly. For each pattern, the participant is asked to touch the plate at the location of haptic feedback. He/She can press several times to get familiar with the feeling conveyed by the current pattern. He/she is then asked to answer a questionnaire, shown in Table 5.1, based on the AttrakDiff questionnaire [34]. After each pattern, the participant is asked to describe how the pattern felt. The mean time of the experiment is around 15 minutes.

The AttrakDiff questionnaire is commonly employed to measure perceived pragmatic quality (PQ), perceived hedonic quality-stimulation (HQS), perceived hedonic quality-identification (HQI) and perceived attractivity (ATT) through evaluational constructs. The questionnaire consists of 7-point items with bipolar verbal anchors (i.e., a semantic differential). Some adjectives of the initial questionnaire are removed as they are not considered to be of high relevance for this specific study.

Pragmatic attributes are linked to the user need to achieve behavioural goals. Goal achievement requires utility and usability and a product that enables effective and efficient goal-achievement is therefore perceived as pragmatic or as having

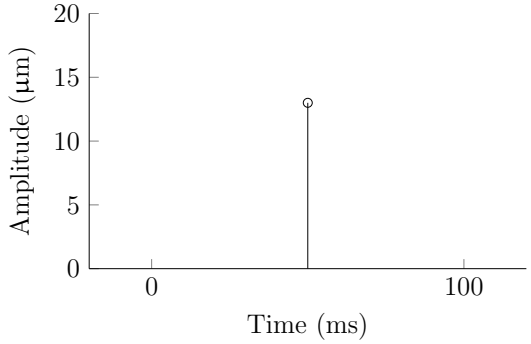

(a) P_0 : Single impact.

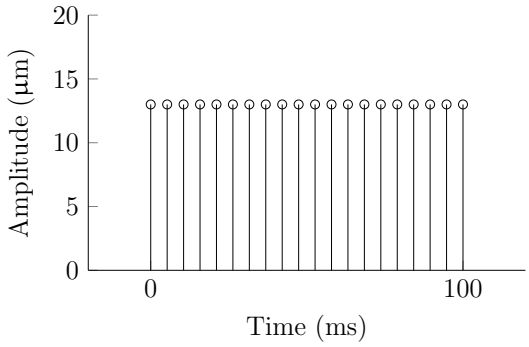

(b) P_1 : Square, $F_{sample} = 200$ Hz.

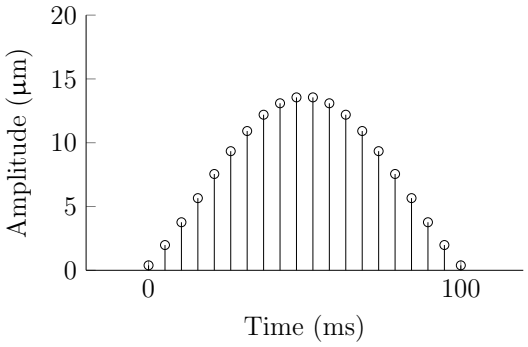

(c) P_2 : Cardinal Sinus, $F_{sample} = 200$ Hz.

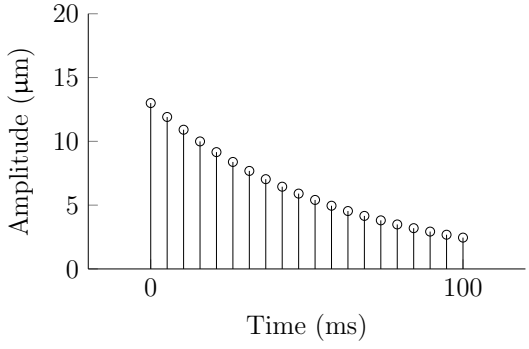

(d) P_3 : Decreasing Exp., $F_{sample} = 200$ Hz.

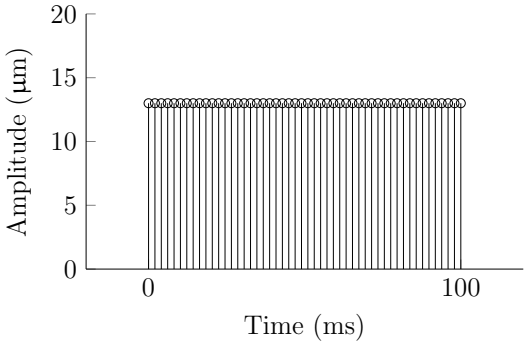

(e) P_4 : Square, $F_{sample} = 500$ Hz.

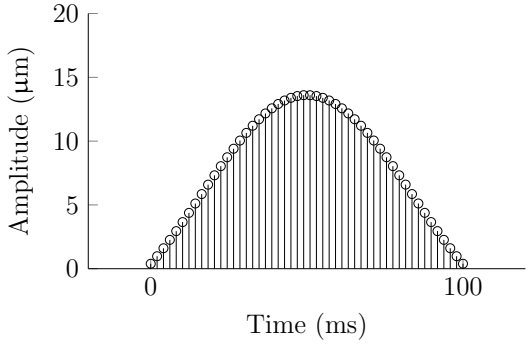

(f) P_5 : Cardinal Sinus, $F_{sample} = 500$ Hz.

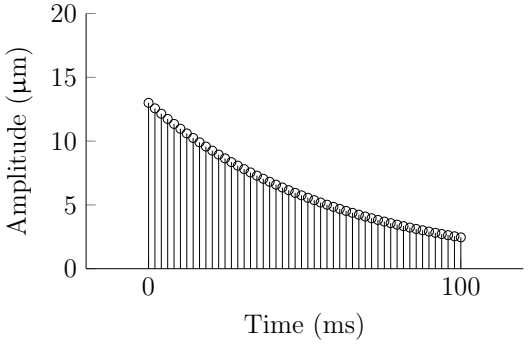

(g) P_6 : Decreasing Exp, $F_{sample} = 500$ Hz.

Figure 5.8: Patterns tested.

perceived pragmatic qualities. A high PQ score implies primarily high usability. Moreover, a product can be perceived as hedonic because it exhibits a challenging

Pragmatic quality (PQ)								
complicated	-3	-2	-1	0	1	2	3	simple
cumbersome	-3	-2	-1	0	1	2	3	straightforward
unpredictable	-3	-2	-1	0	1	2	3	predictable
confusing	-3	-2	-1	0	1	2	3	clearly structured
Hedonic Quality - Stimulation (HQS)								
conventional	-3	-2	-1	0	1	2	3	inventive
dull	-3	-2	-1	0	1	2	3	captivating
ordinary	-3	-2	-1	0	1	2	3	novel
Hedonic Quality - Identification (HQI)								
tacky	-3	-2	-1	0	1	2	3	stylish
cheap	-3	-2	-1	0	1	2	3	premium
unpresentable	-3	-2	-1	0	1	2	3	presentable
Evaluational Constructs - Attractivity (ATT)								
unpleasant	-3	-2	-1	0	1	2	3	pleasant
ugly	-3	-2	-1	0	1	2	3	attractive
disagreeable	-3	-2	-1	0	1	2	3	likeable
repelling	-3	-2	-1	0	1	2	3	appealing
bad	-3	-2	-1	0	1	2	3	good
rejecting	-3	-2	-1	0	1	2	3	inviting
discouraging	-3	-2	-1	0	1	2	3	motivating

Table 5.1: Pattern perception survey.

and novel character or communicates important personal values. A high HQS score implies a high degree of perceived novelty, stimulation and challenge. A high HQI score implies a high perceived capability of communicating identity to others. The use of a product results in emotions, as satisfaction, in evaluations, as judging a product appealing, or behavioural responses, such as approaching or avoiding. The separation of the attributes' perception from their evaluation may lead to find a product novel (an attribute of a product) but not necessarily attractive (an evaluation of a product). Evaluational constructs, such as pleasantness or appeal, are regrouped in the Attractivity section.

5.4.4 Results

Pattern evaluation

Figure 5.9 details the averaged scores of all participants for pattern 0 (single impact). A first analysis is to describe the score for each adjective, in relation to the other patterns. This gives a detailed representation of how the pattern is perceived. The individual score curves for the other 6 patterns are given in appendix A. A first general observation is that throughout the entire adjectives, none are given a negative score. Every pattern is rated on average positively throughout each of the AttrakDiff characteristics.

In Figure 5.9, corresponding to P_0's score, it is possible to qualify a single impact as a clear and straightforward signal. It is however not very pleasant and not inviting. Analysing in details each adjective is rather complex. In the following

section, it is proposed to calculate an average for each category, namely PQ, HQ-S, HQ-I and ATT, to identify trends (see Table 5.1).

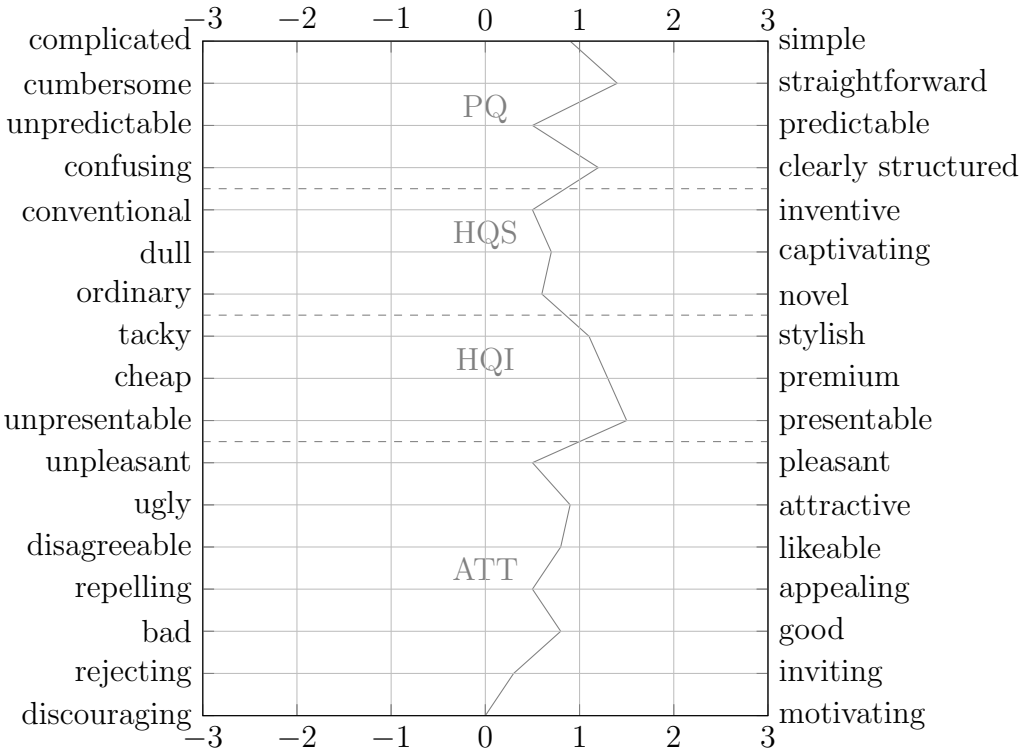

Figure 5.9: Pattern P_0 - score on the AttrakDiff inspired scale.

Patterns comparison

In Figure 5.10 and Figure 5.11 the average scores per pattern are presented. Each data point is plotted with the standard deviation (Mean + σ and Mean - σ). For better clarity the patterns P_1, P_2 and P_3 are first presented and compared to pattern P_0 (Figure 5.10). Figure 5.11 illustrates the scores of the other patterns P_4, P_5, P_6 in comparison to pattern P_0.

One first observation is that no single pattern performs better than the other in every category.

P_1, the square envelope at 200 Hz, has scores above P_0. Its scores are slightly above for PQ, HQ-I and ATT and well above for HQ-S. This means that it is more novel and stimulating for the users than P_0. This comes from its sharp transitions and from the frequency used.

P_2, the cardinal sine at 200 Hz, scores better than P_0 and P_1 (except in HQ-S). It scored best in HQ-I and ATT. This means that it is the best in conveying an identity and the most pleasant pattern. The smooth transitions of its envelope provides simultaneously pleasantness and some difficulties in clear perception.

P_3, the decreasing exponential at 200 Hz, follows a similar trend as P_1 but with lower scores. In both HQ-S and HQ-I it is worse than P_0. Its Attractivity is nevertheless the second best among the tested patterns.

P_4, P_5 and P_6 exhibit lower scores than P_0 in HQ-I and ATT, which makes them not very attractive. P_4 is better in HQ-S and has the best score in terms of PQ. this

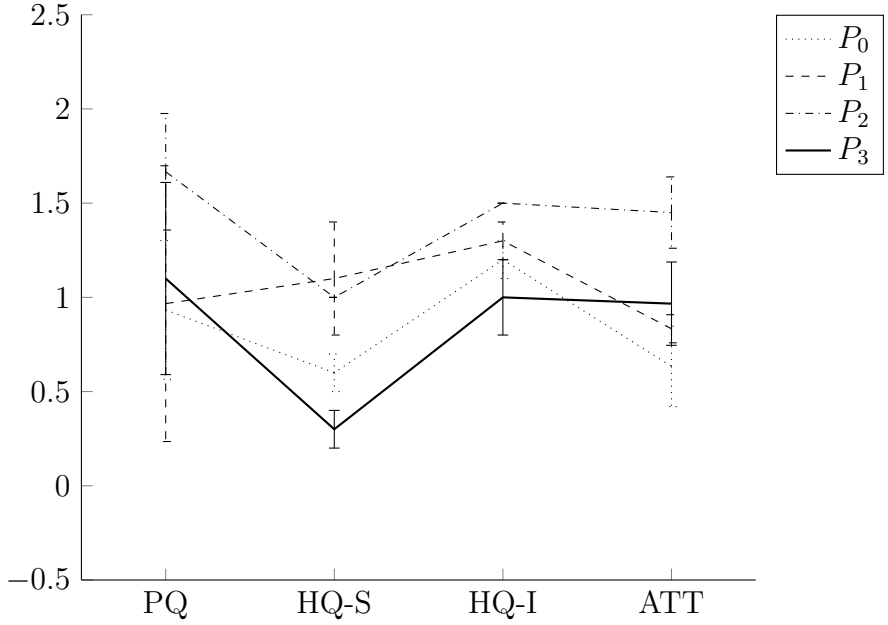

Figure 5.10: AttrakDiff scores of P_0, P_1, P_2 and P_3.

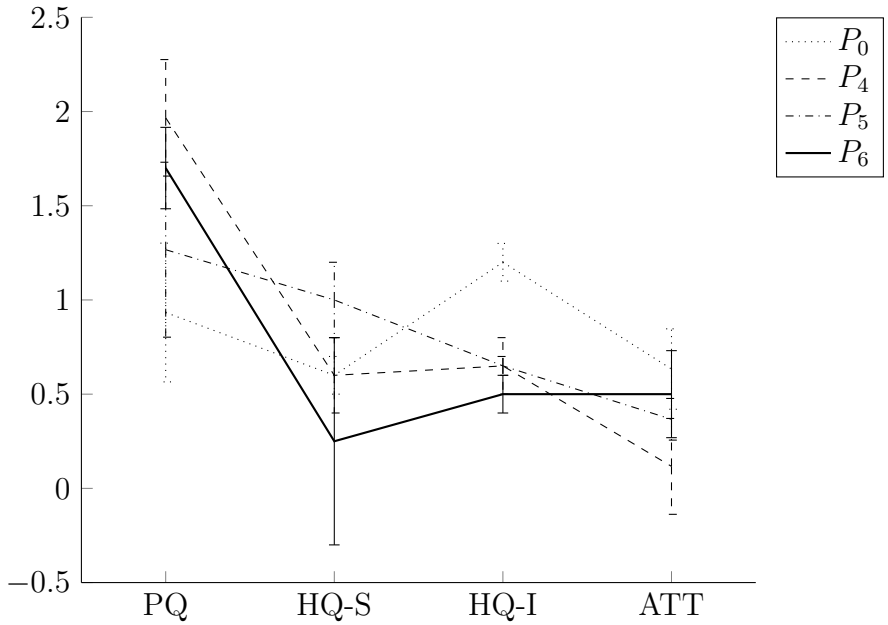

Figure 5.11: AttrakDiff scores of P_0, P_4, P_5 and P_6.

reinforce the fact that square envelopes are good for a clear and direct detection by the user.

From these results, it seems that envelopes and frequencies have a specific effect on the pattern perception. In the following section, the impact of the envelope and the frequency are analysed in detail.

Frequency influence

In Figure 5.12, the mean score of each pattern are grouped by frequency. The scores of the three patterns at 200 Hz (Low frequency, Lf) and the three patterns at 500 Hz

(High frequency, Hf) are averaged separately. Each data point is plotted with the standard deviation (Mean + σ and Mean - σ).

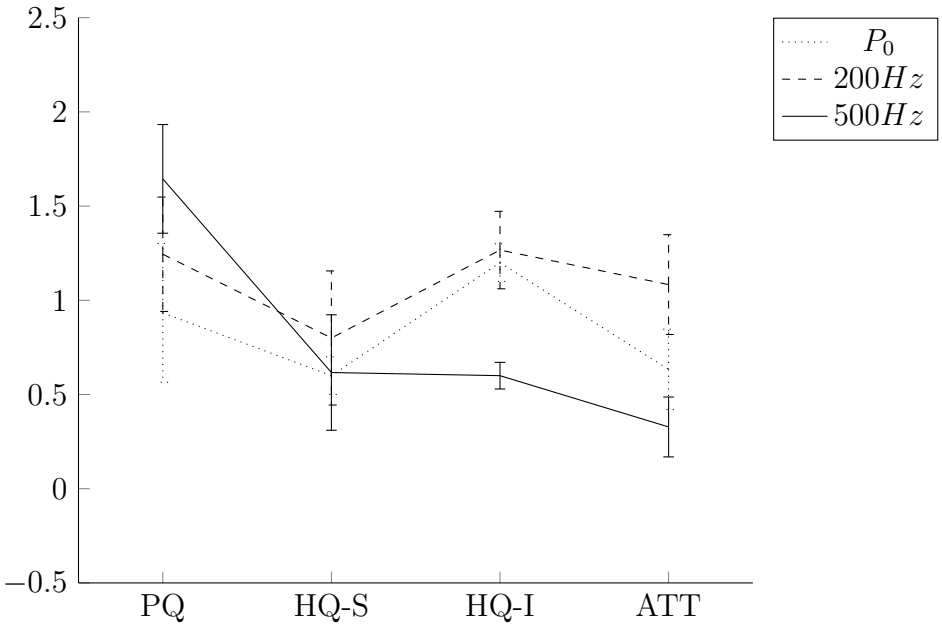

Figure 5.12: AttrakDiff score comparison between Lf and Hf, with P_0's score for reference.

The 200 Hz frequency is slightly better perceived than P_0 and the 500 Hz patterns in terms of hedonic qualities. It stands apart for giving both a pleasant and an attractive feeling with a score exceeding clearly the one of 500 Hz frequency patterns. However, the 500 Hz patterns are better in terms of usability and clarity. This implies that a repetition frequency at 500 Hz generates clearer, better perceived patterns but is less appreciated than lower frequencies.

Envelope influence

On Figure 5.13, the influence of the envelope is studied. Both 200 Hz and 500 Hz signals of each envelope are averaged and plotted. Each data point is plotted with the standard deviation (Mean + σ and Mean - σ).

The square envelopes (P_1 and P_4) present similar behaviour but higher ratings for PQ and HQ-S compared to the single impact. They are worse than the single impact for the HQ-I and ATT. They are the best score in terms of PQ, shared with the cardinal sine envelope. The square envelopes present a better usability and is more stimulating than P_0, but conveys less identity and is considered to be less attractive.

The cardinal sine envelopes (P_2 and P_5) exhibit similar ratings to the square envelopes, but are slightly above for all the other of the categories while still conveying less identity.

The decreasing exponential envelopes (P_3 and P_6) are almost identical to the other patterns in terms of PQ but falls behind on hedonic qualities. They are the second best in terms of pleasantness.

Based on these trends, envelopes with smooth transitions are more likeable than those with abrupt ones. When looking at the overall performances, cardinal sine

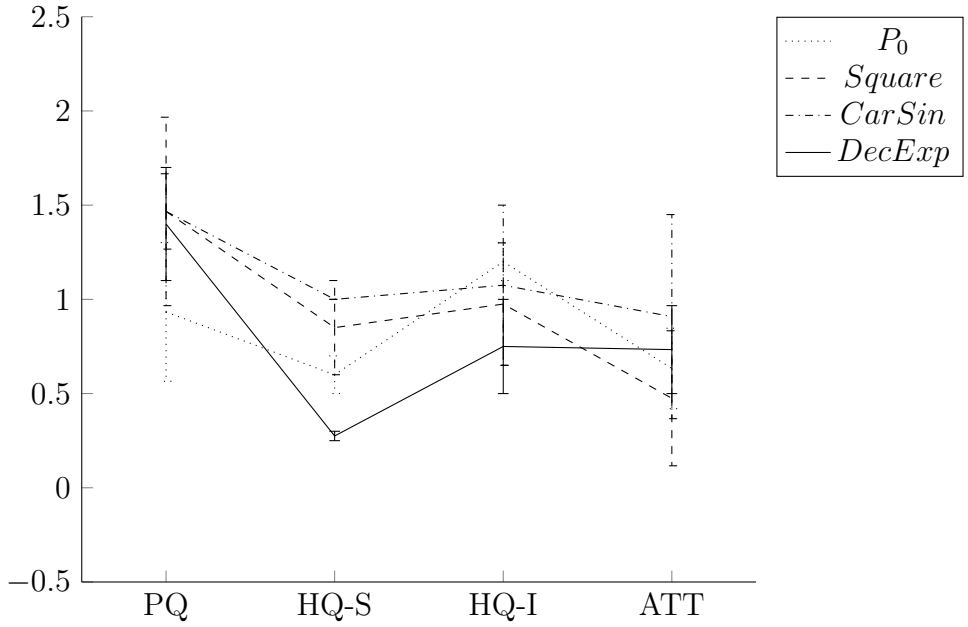

Figure 5.13: AttrakDiff score comparison between the different envelopes, with P_0's score for reference.

envelope would be a preferable choice.

Feedbacks from participants reinforce those trends:

- P_0 : "electrical discharge"
- P_2 : "Pleasant, diffuse, well felt"
- P_2 : "Relatively uniform, so ok : premium feel."
- P_0 : "Very short so less distinguishable."
- P_1 : "Stronger, sharper. Discharge/negative feeling."
- P_2 : "More uniform than P_6, P_4 and P_3, less brief, more surface, larger amplitude in the middle."
- P_5 : "Same as P_2 but larger amplitude in the middle."

5.5 Summary of the results

5.5.1 Applied force effect on the displacement amplitude

In this chapter diffraction losses for a finger pressing up to 2 N are measured at different locations. The location is found to have moderate influence on the diffraction losses. A finger pressing aside the focus point at up to 2 N is found to generate losses up to 6 % of the amplitude peak at the focus point. Losses due to diffraction are however dependent on the surface of the contact. Five fingers pressing on the surface induce a loss of 12 %. A palm laid on the surface results in even greater losses (17 %). Losses due to diffraction increase with the applied force and also with the surface of the contact. When the finger presses directly on the focus point is

the prime source of loss in time reversal. Indeed, when a finger applies a 2 N force at the focus point, the generated amplitude drops by 37 %.

5.5.2 Detection threshold

The detection threshold of different users is measured in this chapter. The results of this preliminary study cannot be extrapolated to a broader population due to the small tested population. A first trend is that the force with which the user presses on the screen seems barely influencing the perception threshold. This study however allows to determine the amplitude level requirement for future experiments. The amplitude of the generated impact should be at minimum 10 µm for a perception rate close to 100 %.

5.5.3 Perception

The study presented in this chapter compares patterns with high (500 Hz) and low (200 Hz) frequency of impact repetition and several envelope shapes. The low frequency (200 Hz) and the smoothness of the cardinal sine envelope are found to be the best in terms of pleasantness. However, in terms of clarity, a 500 Hz square shaped repetition is the best. The cardinal sine is of special interest since it performs well in terms of attractivity. More frequencies should be tested (50 to 450 Hz, in 50 Hz steps for example), to further explore whether there is a frequency at which the usability is maximised. Another study could test other envelopes to determine whether the combination of smooth and sharp transition for example, improves the ratings in the different categories.

Chapter 6

Electrovibration: theory and perception

6.1 Introduction

In the previous chapters, the focus is on static touch feedback. This supposes a user pressing on the screen as the aim is to provide a button-click feedback. This chapter is focusing on dynamic touch feedback. The objective is to provide complimentary haptic feedback while the user moves his finger across the screen. Such stimulation can be used to mimic a texture sensation, from coarse textures, such as the gratings on a volume slider, to fine texture, such as displaying different fabrics on a virtual catalogue. Electrovibration can provide this kind of feedback. It can be easily integrated and offers a wide range of texture possibilities. The working principle is based on an electrostatic force generated between the finger and the explored surface, which attracts the finger towards the surface. The variation of this force in correlation with the movement of the finger generates the electrovibration sensation. Indeed, nothing is felt if the finger is static. However, as the finger moves across the surface, the variation of the attractive force causes the finger to be slowed down. This results in the modification of the apparent friction coefficient between the finger and the surface, which generates a "texture" feeling, as shown in Figure 6.1.

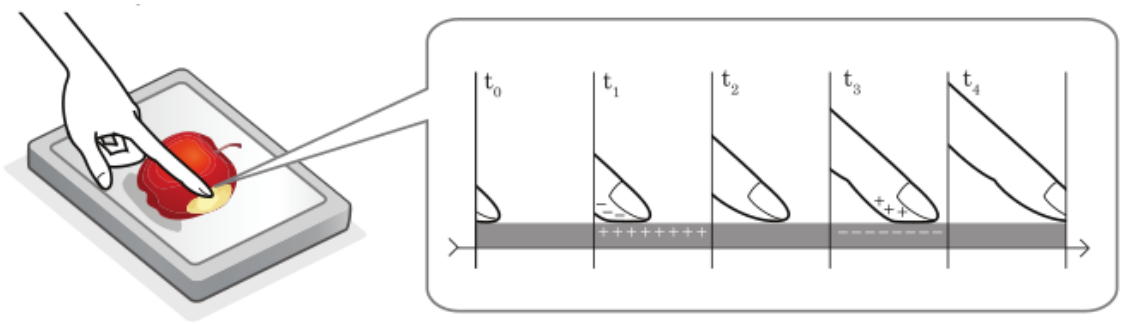

Figure 6.1: As the finger moves across the screen, the electrostatic force is varied according to the targeted texture feedback, from [3].

Figure 6.2 shows the principle of the electrostatic force generation. An electrode is embedded in the screen and electrically linked to a voltage source. A transparent electrode layer can be deposited on the structural layer of the screen, which is made out of glass. The transparent electrode is covered by a thin insulation coating. The finger is in direct contact with this coating. In most cases, the user is grounded by touching an electrode connected to the electrical ground of the circuit.

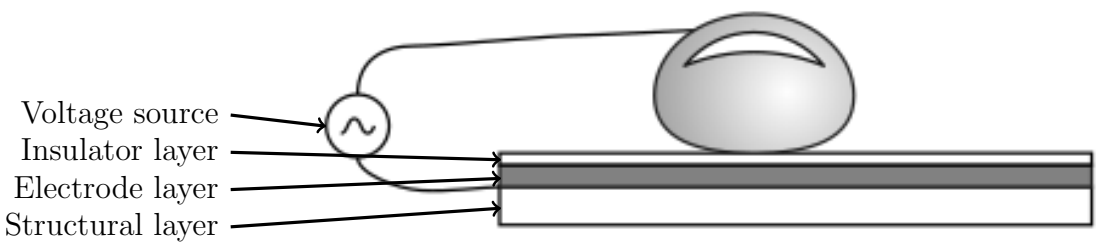

Figure 6.2: Principle of an electrovibration tactile device, from [62].

The texture feeling results from the timely variation of the voltage amplitude fed to the system. Figure 6.3 shows the principle of texture simulation on a surface. In this case, the only signal shape used is sinusoidal. However, different signals such as of the square and sawtooth type can be used. The frequency and amplitude are controlled according to the grayscale level of the texture displayed on the surface. Based on the position x of the finger, a specific signal is applied to the electrovibration system and generates a variable texture feedback.

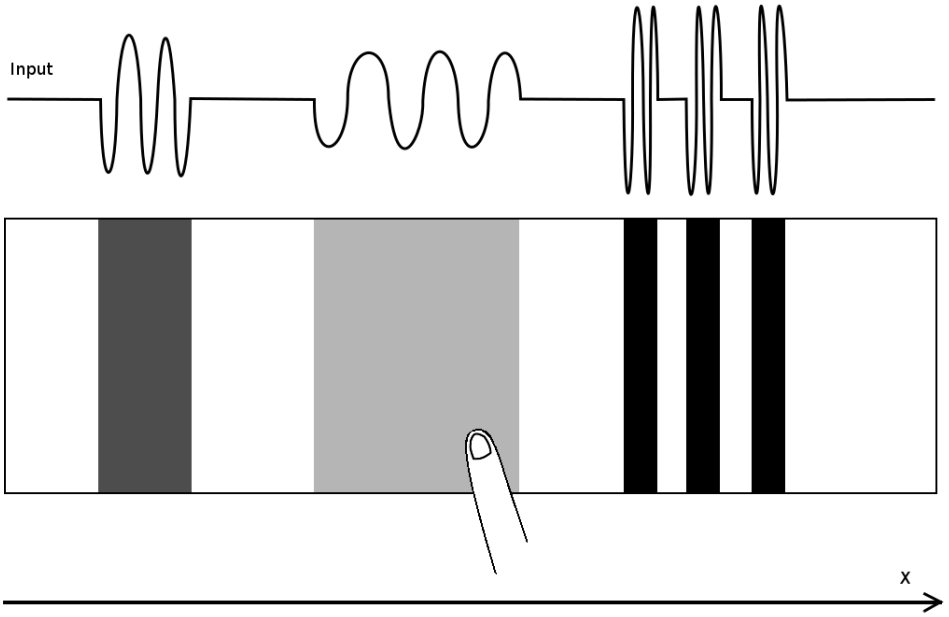

Figure 6.3: Input signal as a function of the finger's position (x) to create different texture sensations on a haptic surface.

The influence of frequency and amplitude of sine signals on the perceived feeling has been studied in [3]. Low frequency stimuli (80 Hz) are perceived as rougher compared to higher frequency (400 Hz). They were often linked to "wood" and "bumpy leather" versus "paper" and "a painted wall" for higher frequency stimuli. At 80 Vpp textures were mostly compared to "cement surface" and "cheap paper", whereas at 115 Vpp they were compared to "paper" or "a painted wall". For high frequency textures (400 Hz) an increase of amplitude increased perceived smoothness of tactile sensations.

In this chapter theoretical background is covered and the influence of the user applied force on the electrovibration perception is studied.

In section 6.2, the principle of generating an electrostatic force between the finger and a surface is explained. A dynamic model for the electrostatic force generation is then presented.

In section 6.3, an experimental set-up is built to test the influence of the applied force on tactile perception thresholds for electrovibration stimuli.

6.2 Fundamentals of electrovibration

A simplified model of the contact between the plate and the fingertip is presented in subsection 6.2.1 to explain the principle of electrostatic force generation. A parallel plate capacitor with no fringe capacitance is considered. The model assumes first the medium between both electrodes to be vacuum. The embedded conductive electrode in the screen is the first plate and the conductive part of the finger's skin is the second plate of the capacitor. Taking into account the fingertip's skin structure and the dielectric layer deposited on top of the screen's electrode lead to a dynamic model of the electrostatic force, which is presented in subsection 6.2.2. The model's prediction are then discussed in subsection 6.2.3.

6.2.1 Electrostatic force generation

An electrostatic force is generated when two electrodes, presenting a voltage differential, are separated by a dielectric medium. This is what happens in a capacitor, where the two electrodes are fixed. If one of the electrodes is mobile, the generated force attracts it towards the other electrode, which is what occurs during an electrovibration stimulation. The fingertip's skin is attracted towards the haptic screen.

A parallel plate capacitor is used, to express the electrostatic force generated between both plates. Two planar electrodes are separated by vacuum, as shown in Figure 6.4.

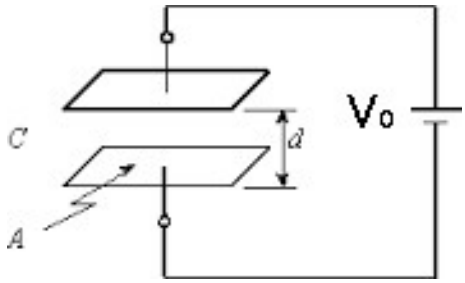

Figure 6.4: Parallel plate capacitor.

The capacitance C_0 between both plates, separated by vacuum, is defined by:

$$C_0 = \frac{\epsilon_0 \cdot A}{d} \tag{6.1}$$

Where ϵ_0 is the relative permittivity of vacuum, A is the plate's area and d is the distance between the two plates. The energy stored, W, is calculated with:

$$W = \frac{1}{2} C_0 \cdot V_0^2 \tag{6.2}$$

Where V_0 is the electrical potential difference between the plates. Finally, the electrostatic force generated between the two plates, F_e is given by:

$$F_e = \frac{W}{d} = \frac{\epsilon_0 \cdot A \cdot V_0^2}{2d^2} \tag{6.3}$$

6.2.2 Electrovibration model

In practice the two plates (the electrode and the conductive part of the fingertip) are not separated by vacuum. The electrode is covered with an insulating material with a thickness d_i and a permittivity ϵ_i. The conductive part of the fingertip is isolated with a skin layer, the stratum corneum. This layer is first considered as a pure insulator of thickness d_{sc} and permittivity ϵ_{sc}. The stacking of both layers is approximated by modelling two stacked capacitors. To compute the equivalent capacity C_e of two stacked capacitors, Equation 6.4 is used:

$$C_e = \frac{1}{C_i} + \frac{1}{C_{sc}} = \frac{1}{\frac{\epsilon_0 \epsilon_i \cdot A}{d_i}} + \frac{1}{\frac{\epsilon_0 \epsilon_{sc} \cdot A}{d_{sc}}} \tag{6.4}$$

The energy stored, from Equation 6.2 is given by:

$$\frac{1}{2} C_0 \cdot V_0^2 = \frac{1}{2} \cdot \frac{1}{\frac{d_{sc}}{\epsilon_{sc}} + \frac{d_i}{\epsilon_i}} \cdot \epsilon_0 \cdot A \cdot V_0^2 \tag{6.5}$$

The electrostatic force, from Equation 6.3, is then:

$$F_e = \frac{W}{d} = \frac{\epsilon_0 \cdot A \cdot V_0^2}{2 \cdot \left(\frac{d_{sc}}{\epsilon_{sc}} + \frac{d_i}{\epsilon_i} \right) \cdot (d_{sc} + d_i)} \tag{6.6}$$

First, the parameters taken into account in the model are defined (see Table 6.1). The considered electrovibration screen here is a 3M touchscreen. Its datasheet mentions the insulating layer thickness and relative permittivity. The generated electrostatic force grows linearly with the contact area, according to Equation 6.6. Measurements showing that the contact area is affected by the applied force by the finger on the screen are carried out (see Appendix B). Using the model from Equation 6.6 with a constant voltage of 50 V, the evolution of the electrostatic force is illustrated in Figure 6.5. The electrostatic force given by this static model matches previous work published in [61] and [80].

Characteristics	Value
Vacuum permittivity, ϵ_0	$8.85 \cdot 10^{-12}$ F/m
Insulator relative permittivity, ϵ_i	3.9
Insulator thickness, T_i	1 µm
Stratum Corneum relative permittivity, ϵ_{sc}	1000
Stratum Corneum thickness, T_{sc}	200 µm
Stratum Corneum resistivity, ρ_{sc}	33 kΩ

Table 6.1: Skin and screen parameters.

Time-dependent behaviour of electrovibration feedback

The structure of the fingertip skin has been extensively studied in biology related research. Measurements of the thickness of the stratum corneum through optical coherence tomography are presented in [23]. It shows that large differences exist: on the right index finger the measured thickness at the center of the fingertip ranges

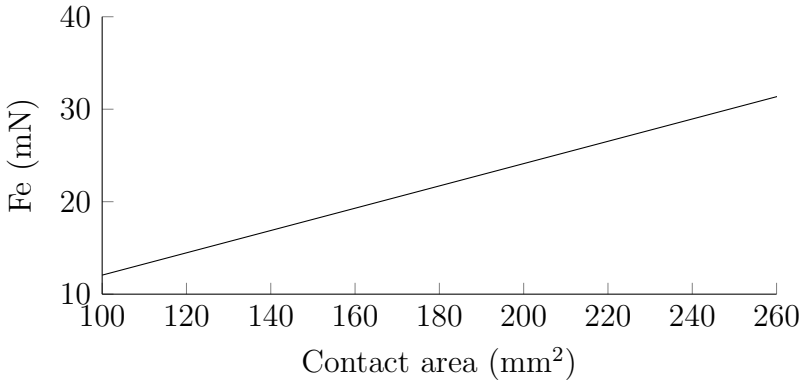

Figure 6.5: Electrostatic force F_e as a function of the contact area A.

from 130 µm to 795 µm. There is an average difference of 51 µm between male and female subjects. As the thickness of the stratum corneum is directly involved in the generation of the electrostatic force, the users may feel strong variations of the stimuli's perception.

Furthermore, it is known that the stratum corneum is not a perfect insulator as some electrical charges can pass through it. It has also been shown that the electrical permittivity of the stratum corneum varies with the frequency of the imposed stimulus. The electrical permittivity of the stratum corneum ϵ_{sc} and its resistivity ρ_{sc} (respectively ϵ_k and ρ_k, in Figure 6.6) as a function of the frequency of the stimulus are measured in [87].

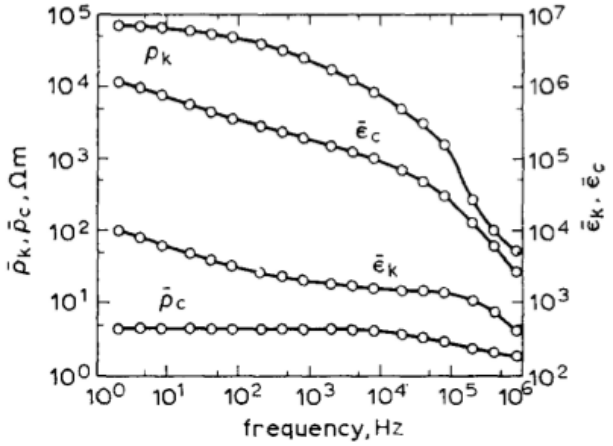

Figure 6.6: Average resistivities ρ_k and ρ_c and dielectric constants ϵ_k and ϵ_c of the stratum corneum and of the deeper skin tissues, from [87].

The loss of electrical charges through the fingertip skin can be modelled as a resistor and a capacitor in parallel ([61], [80]), as shown in Figure 6.7.

The insulator's capacitance C_i, the stratum corneum's capacitance C_{sc} and the stratum corneum's resistance R_{sc} are given by:

$$C_i = \frac{\epsilon_0 \epsilon_i \cdot A}{d_i} \tag{6.7}$$

$$C_{sc} = \frac{\epsilon_0 \epsilon_{sc} \cdot A}{d_{sc}} \tag{6.8}$$

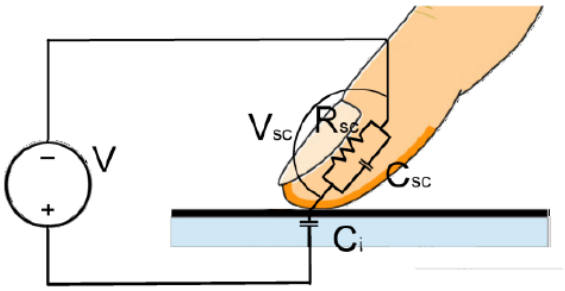

Figure 6.7: Electrovibration model, with the stratum corneum layer modelled as a parallel resistor and capacitor, [80].

$$R_{sc} = \frac{\rho_{sc} \cdot d_{sc}}{A} \tag{6.9}$$

where ρ_{sc} is the resistivity of the stratum corneum. Kirchhoff's law applied to the circuit in Figure 6.7 gives Equation 6.10, with i_i the current flowing through the insulator, $i_{C_{sc}}$ the current flowing through C_{sc} and $i_{R_{sc}}$ the current flowing through R_{sc}.

$$i_i - i_{C_{sc}} - i_{R_{sc}} = 0 \tag{6.10}$$

The relation between the current i and the voltage V in a capacitor of capacitance C is:

$$i = C \cdot \frac{dV}{dt} \tag{6.11}$$

i_i and $i_{C_{sc}}$ can then be expressed:

$$i_i = C_i \cdot \frac{d(V - V_{sc})}{dt}, \tag{6.12}$$

$$i_{C_{sc}} = C_{sc} \cdot \frac{d(V - V_{sc})}{dt} \tag{6.13}$$

and Ohm's law is used to express $i_{R_{sc}}$

$$i_{R_{sc}} = V_{sc}/R_{sc} \tag{6.14}$$

Introducing Equation 6.12 – 6.14 in Equation 6.10 gives

$$\frac{d(V_{sc})}{dt} = -\frac{1}{(C_i + C_{sc})R_{sc}} \cdot V_{sc} + \frac{C_i}{C_i + C_{sc}} \cdot \frac{dV}{dt}. \tag{6.15}$$

The differential equation is solved with Matlab using the ODE45 method, which gives V_{sc}. The result is then used to compute the electrostatic force, F_e. V_{sc} is then introduced in Equation 6.6, replacing V_0. This leads to a time-dependent behaviour of the electrostatic force, which is examined in detail in the next section.

6.2.3 Input signals

In this section the input signal effect on the electrovibration force is presented. Square, trapezoidal and sinusoidal signal shapes are compared using the model presented in the previous section. The evolution of the electrostatic force with the different contact area measured in Appendix B is shown with the dynamic model. Average values for the stratum corneum permittivity ϵ_{sc}, thickness T_{sc} and resistivity ρ_{sc} are used (see Table 6.1). It is worth noting however, that ϵ_{sc}, T_{sc} and ρ_{sc} values exhibit a large person-to-person variability. The skin's condition and humidity also affects those values. For instance, the resistivity ρ_{sc} can easily vary by a factor 1 to 10, impacting V_{sc} (see Equation 6.15), which is squared in the model from Equation 6.6. This leads to variations for the electrostatic force F_e by a factor 1 to 100. It is therefore difficult to give precise values without adjusting the model parameters to measured skin characteristics ϵ_{sc}, T_{sc} and ρ_{sc}. Nevertheless, the objective here is not to determine precise amplitudes of the electrostatic force but rather to study its dynamic behaviour and therefore F_e is presented in the curves with no scale.

Figure 6.8 indicates the electrostatic force profile generated by a step input signal for various contact areas. A constant signal does not induce a continuous force. The force increases quasi instantly with the initial step input and then decreases with an exponential decay. This decrease is the result of the slow loss of charges of the stratum corneum modelled by the RC-part introduced in Equation 6.15. The electrostatic force peak value increases with an increase of the contact area.

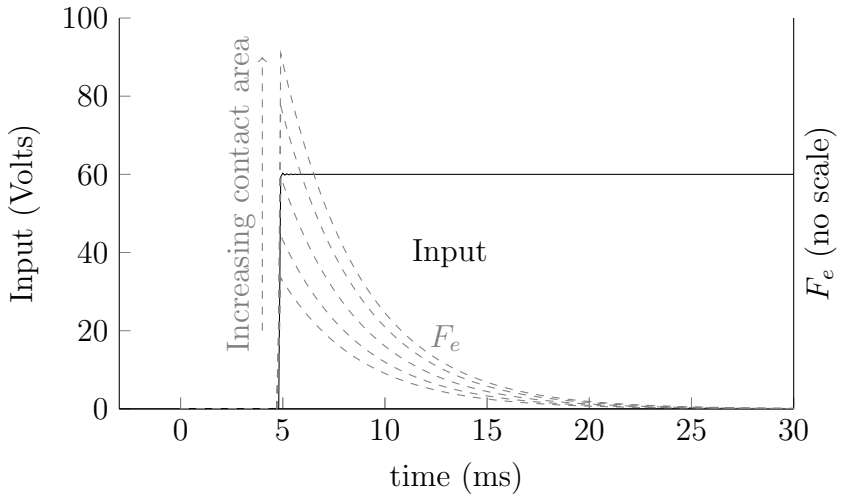

Figure 6.8: Electrostatic force F_e generated by a step input signal for various contact areas.

Figure 6.9 indicates the electrostatic force profile induced by a trapezoidal signal for various contact areas. It shows that for a given linear rising time, the electrostatic force increases rapidly. When the maximum input voltage is reached, the electrostatic force decreases in an inverse exponential decay.

In order to generate a more continuous stimulation, an alternating signal has to be used as discussed in [80]. As F_e varies with the square of V_{sc}, a positive force is generated independently of the voltage sign. Both the positive and negative parts of a 5 Hz sinusoidal input signal are converted into an electrostatic force of 10 Hz. Figure 6.10 indicates this doubling phenomenon for various contact areas.

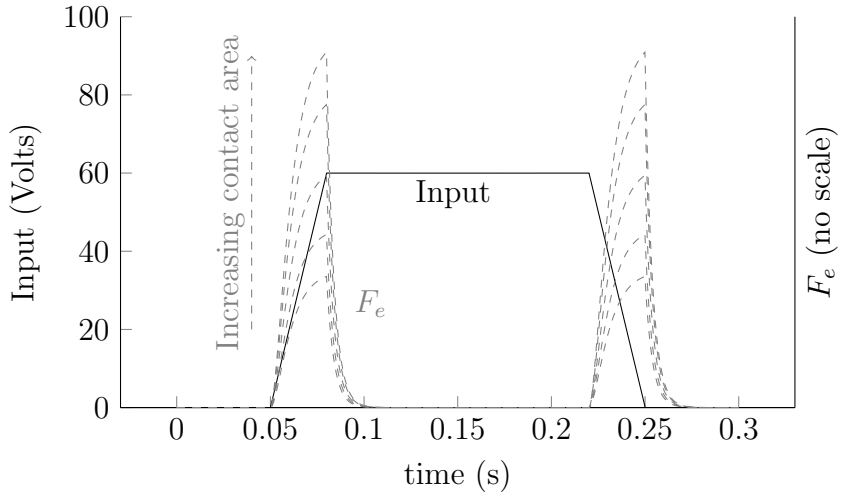

Figure 6.9: Electrostatic force F_e generated by a trapeze input signal for various contact areas.

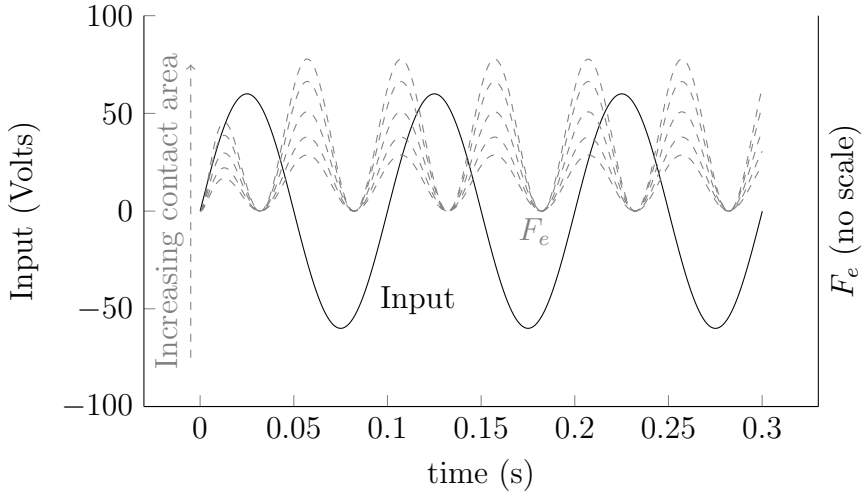

Figure 6.10: Electrostatic force F_e generated by a sine input signal for various contact areas.

As a summary, the model from Equation 6.6, F_e is inversely proportional to $d = d_i + d_{sc}$. As the stratum corneum thickness cannot be modified, the only parameter that can be modified is d_i. If F_e needs to be increased, then d_i should be minimised. It cannot however be reduced to zero, as with a thinner insulator a lower dielectric breakdown voltage occurs. From Equation 6.15, V_{sc} is proportional to dV/dt and C_i. To increase C_i, d_i should be decreased and ϵ_i increased. The model shows that a drop from 80 V to 8 V can be compensated by an increase in ϵ_i from 3.9 to 12. A careful choice in the insulation layer of the screen could either increase the generated electrostatic force or lower the required input voltage.

The electrostatic force F_e depends also on the fingertip area in contact with the screen. In the previous examples of input signals, the relative variation between the smallest and the largest contact area (see Appendix B) corresponds to a factor 2.7. Therefore, in the next section, the influence of applied force on the perception of electrovibration stimuli is investigated.

6.3 Electrovibration and perception

6.3.1 Experimental set-up

A screen providing tactile feedback is built using a commercially available 15.4" 3M touchscreen Figure 6.11. The screen is made of a structural glass layer with a thin layer of Indium-tin oxide (ITO) over the glass and acting as the electrode for electrovibration. An insulating dielectric layer is deposited on the top.

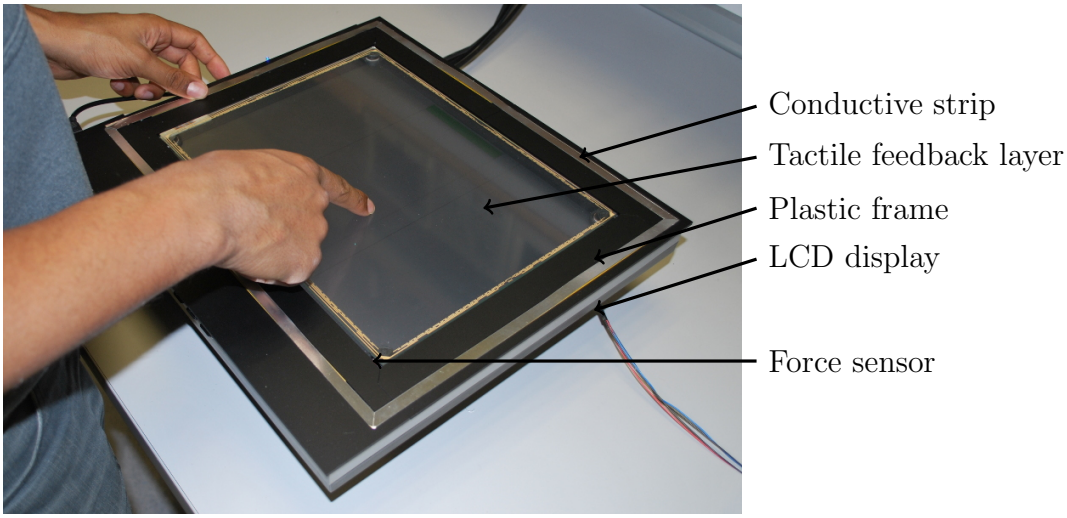

Figure 6.11: A user exploring the electrovibration display.

The control interface is programmed with LabVIEW. The tactile signals are generated with a NI cDAQ-9174 rack equipped with a NI 9264 analogue output module and amplified to ± 25 V with an amplifier (Elbatech T-503). The user is asked to freely touch the screen with his dominant hand in order to feel the electrovibration feedback. A plastic frame with a conductive strip is used around the screen. The user is asked to touch this conductive strip with his second hand in order to ground him to the device. The frame is fixed to a 19" LCD display. The force applied by the user is measured through a Honeywell FSS1500NSB force sensor.

Two studies are undertaken in an attempt to determine whether or not, the applied force when exploring a displayed electrovibration pattern influences the perception thresholds of electrovibration stimuli. In the first study, the applied force while exploring a screen without any tactile feedback is measured. Users are asked to draw a linear trajectory across the screen while applying three different force levels that they estimate to be 'light", "medium" and "high" when exploring a texture or a surface with different rougnesses. The second study aims to determine the absolute perception thresholds for electrovibration stimuli for five different sinusoidal frequencies and three different force levels. The different force levels are based on the results of the first study.

6.3.2 Exploration and force levels

15 participants (12M with one being left-handed, 3F, average age = 37 years) took part in the first study. The screen is placed horizontally on a table. The users

have to stand in front of it during the experiment. The task is to draw a line with the index from their dominant hand on the screen. Instructions are given in the form of two different constraint levels: 1) to follow a cursor moving in a straight line at a constant speed (constrained) and 2) to draw freely a line across the screen (unconstrained). The cursor speed is constant and set at 60 mm/s. The participants are also asked to apply three different force levels: "light", "medium" and "high". A few guidelines are provided, as the first level should be similar to contact, and the last could be relatively hard compared to a normal interaction with touchscreen devices. The main instruction is to be coherent from one trial to another according to the force levels. Every user undergoes the full set of 6 conditions. The presentation of the 2 instructions and 3 force levels are counterbalanced to control for order effects. Each condition is repeated 3 times.

For each trial, the measured force is averaged to obtain a mean applied force value. The mean value for each participant is then averaged for each different condition, as shown in Table 6.2.

	Light	medium	high
Constrained	1.2	2.39	5.16
Unconstrained	1.6	3.05	5.24

Table 6.2: The mean applied force (in N) for each condition.

The first observation is that, in the unconstrained condition, the mean force is always higher than the one in the constrained condition. On the first two force levels the increase is almost 30 %, whereas on the last force level it is only 1.5 %. This might be due to the moving cursor. As soon as pressure is detected, the cursor starts to move at a constant speed. The collected data show that in this case, the participants usually rush to reach the force they want to apply but have to follow the cursor at the same time. This results in a sizeable overshoot on the applied force during the first part of the movement. However, as the cursor continues its movement, they concentrate on following the cursor and adjusted the applied force a bit during the second part of the movement.

Figure 6.12 gives a detailed representation of the measured applied force values for each condition.

A two-way within subjects analysis of variance (ANOVA) reveals that there is a statistically significant effect of the force on the mean applied force values ($F(5, 9) = 11.574; p < 0.002$) while the effect of the trajectory is not statistically significant.

The average of the upper quartile from the "medium" force values and the lower quartile from the "high" force values give the separation between "medium" and "high", see Figure 6.13. The lower boundary of "light" is given by the lower quartile of "light" force value. The upper boundary of the "high" force interval is given by the upper quartile of "high" force. To sum up, the determined intervals are:

- "light", from 0.2 N to 1.5 N
- "medium", from 1.5 N to 3.0 N
- "high", from 3.0 N to 7.0 N

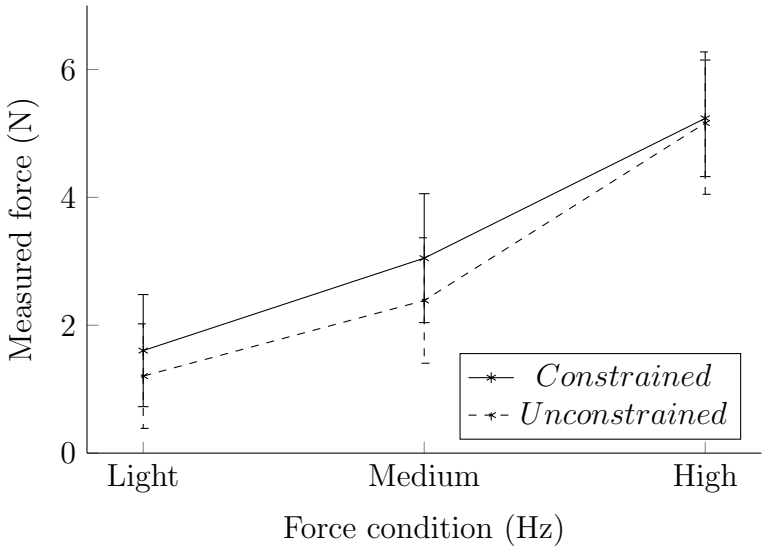

Figure 6.12: Mean applied force values for each condition.

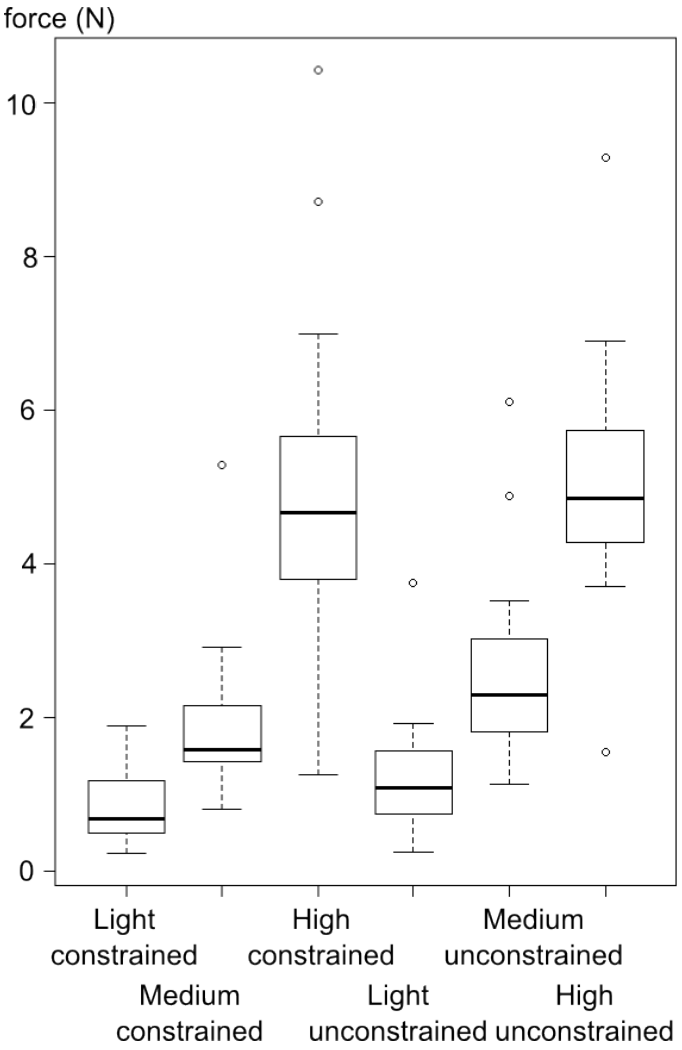

Figure 6.13: The measured applied force values for each condition.

6.3.3 Perception thresholds

10 participants (10M with one being left-handed, average age = 36 years) took part in the second study. Similarly to the first study the screen is placed horizontally on a table and the users have to stand in front of it during the experiment. The participants are asked to follow a moving cursor with the finger while applying a required force level. The cursor is visualised on an LCD display, as shown in Figure 6.14. The exploration distance is approximately 20 cm and the cursor is moving at a constant speed of 60 mm/s. The constant exploration speed enables to compare the detection threshold at different frequencies. Two small circles moving along the cursor inform the user of the required force level (i.e. the force instruction) and the currently applied force (i.e. the measured force). The force is split into 3 intervals: "light", "medium" and "high" indicated by green, yellow and red respectively. These intervals are based on the results of the first study. The path of the cursor is crossing two zones, A and B, while only one randomly chosen zone exhibits a tactile feedback stimulus. The first few centimetres before the zones allows the participants to adjust to the correct amount of required force. The participant has to indicate in which zone the stimulus is displayed.

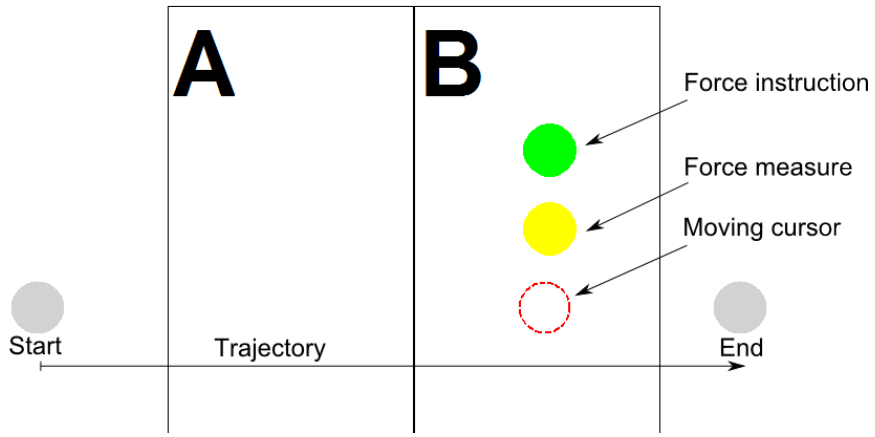

Figure 6.14: The interface with the trajectory, cursor, force indicator and force instruction.

Sinusoidal signals are used as stimuli. Their frequencies are equally spaced on a logarithmic scale. The frequency doubling of the applied voltage induced by the electrovibration phenomenon results in stimuli of perceived frequency of 100 Hz, 160 Hz, 240 Hz, 360 Hz and 540 Hz. The chosen threshold unit is "dB re 1 V peak" which is computed as $20 \cdot log(A)$ where A is the signal amplitude in Volts. Using this unit is a standard practice in psycho-physical experiments due to the linearity of human perception on logarithmic scale [43] and was already used in [3]. A staircase method is used to find the sensitivity threshold of the participant for each condition. After two correct answers, the amplitude decreases by 1 dB, while an incorrect answer increases the amplitude by 1 dB. A series of three changes from correct to incorrect and vice-versa, called a reversal, leads to the reduction of the increase/decrease steps from 1 dB to 0.25 dB. After a total of 9 reversals, the session is completed. The detection threshold is estimated on the basis of the average amplitude of the last 5 intensity values. Before the experiment, there is

a familiarisation phase, during which the participants can adjust the applied force to the required level while following the cursor. They are then presented with the five frequencies of stimuli used, at different levels of intensity in order to become accustomed with the stimuli. This allows to establish different starting intensities for each participant and, thus, reduces the overall amount of trials needed to determine their sensitivity thresholds. It takes between 20 and 50 trials for each condition to find the sensitivity threshold resulting in an average experiment duration of 45 minutes for each user. Between each condition the user is asked to wash his hands and the screen is wiped in order to minimise user variability (perspiration) and environmental factors (dust and grease deposit on the screen).

The last five intensity values given by the staircase method are averaged to obtain the perception thresholds for each condition. These values are then averaged across user and summed up in Table 6.3.

	100 Hz	160 Hz	240 Hz	360 Hz	540 Hz
Light	12.1	8.8	7.9	8.9	11.0
Medium	12.1	8.4	6.7	7.6	8.9
High	11.4	8.5	6.3	8.1	8.9

Table 6.3: Mean perception threshold per frequency and force levels in dB re 1V peak.

Figure 6.15 gives a detailed presentation of the measured perception threshold per frequency and force levels.

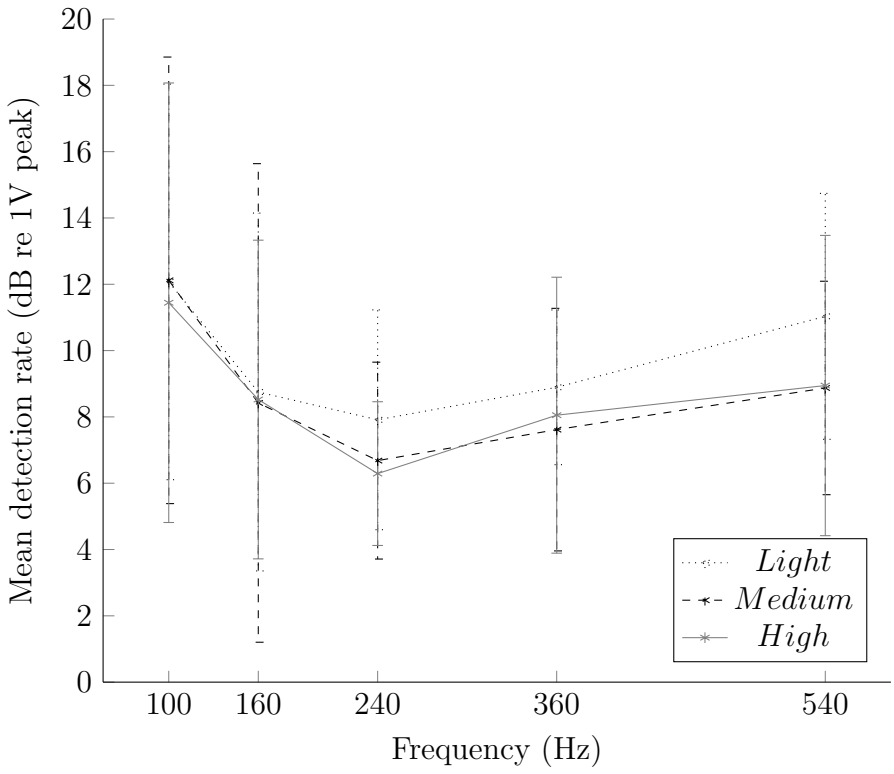

Figure 6.15: Mean detection rate as a function of frequency, for three different force levels.

At "light" force level the determined thresholds are comparable to those determined in [3]. From 100 Hz to 240 Hz the threshold decreases rapidly and attains a minimum at 240 Hz. From 240 Hz to 540 Hz the perception threshold exhibits a slow increases. This evolution is observed for each force level, where the 240 Hz stimulus is the frequency with the lowest perception threshold. This matches the current knowledge in the physiology of touch that the highest fingertip sensitivity to vibration lies around 250 Hz.

For low frequencies (100 Hz and 160 Hz) no effect on the perception threshold was measured for all force levels. With the increase in force from light to medium, the thresholds get lower for higher frequencies (240 Hz, 360 Hz and 540 Hz). With the increase in force, the deformation of the fingertip is larger. This means that a larger surface of the fingertip is in contact with the screen. The effect could be twofold. As the surface increases, the electrostatic force generated by electrovibration is greater as given by the model presented in subsection 6.2.2. As the contact surface increases, the number of mechanoreceptors stimulated by the electrovibration increases, leading to a better perception of the stimulus. However, the surface area tends to saturate when the force is significantly increased (see Appendix B). This can explain the close behaviour observed for medium and high force, which resulted in almost identical sensitivity thresholds.

A two-way within subjects ANOVA reveals that there is a statistically significant effect of the frequency on the perception threshold values ($F(8,1) = 4.613; p < 0.04$) while the effect of the force is not statistically significant.

6.4 Conclusion

In this chapter the electrovibration effect, which generates electrostatic forces between the screen and the finger, is introduced. A model of the effect is presented, which takes into account the dynamic properties of the fingertip's skin.

The influence of the applied force on the perception threshold of tactile feedback is then studied. The haptic feedback screen relies on a touch screen with single touch detection.

In a first study, 15 participants are asked to draw a line, with either a constrained or unconstrained trajectory, while applying different force levels: "light, medium or high". The applied force is measured for each trial. The results of this study provided three force intervals.

In a second study, users are asked to follow a moving cursor displayed on the haptic screen while applying a required amount of force. The experiment is conducted on 10 participants. The linear trajectory of the cursor crosses two zones with one, randomly chosen, exhibiting a tactile stimulus. Five frequency levels are tested: 100 Hz, 160 Hz, 240 Hz, 360 Hz and 540 Hz. The required force is split into three intervals, "light", "medium" and "high" based on the results of the first study. A staircase method is used to find the perception threshold in intensity for each force-frequency combination. The perception threshold reaches a minimum for the 240 Hz stimulus. This variation significance is confirmed by an ANOVA analysis and fits with the peak of tactile sensitivity for human beings.

The mean perception thresholds are similar across the three force intervals for the 100 Hz and 160 Hz stimuli. However, the mean perception thresholds tend to decrease between light and medium force at 240 Hz, 360 Hz and 540 Hz. The

high force exhibits a similar behaviour to the medium force. However the ANOVA analysis concludes to a non-significant effect of the force on the detection threshold for this small population.

For the tested population, a small force effect was measured for higher frequencies. This needs to be confirmed by larger population user tests. Nevertheless, those preliminary results could be valuable for the design of future interfaces with tactile feedback relying on electrovibration. If the feedback should be constant along an exploratory movement, its intensity needs to be adjusted relatively to the variation in applied force. Potential users will explore haptic screens with a great variety of force as hinted by the study in subsection 6.3.2. It seems that giving the exact same level of feedback to different users will require an adjustment of the feedback's intensity according to the applied force.

Chapter 7

General conclusion and outlook

In this work, two haptic approaches with complementary feedback for large surfaces are studied in order to enrich haptic feedback in current devices. Time Reversal of acoustic waves allows to achieve localised vibrations on a surface and is compatible with multi-point simultaneous feedback. Another approach for providing rich tactile interaction is friction control, which is able to provide a "texture" feeling. Electrovibration which has also been addressed in this work can reproduce haptic textures. Combining both technologies on a single interface would provide rich haptic feedback enabled interactions, with a potential multi-point capability.

The fundamentals of time reversal of acoustic waves are first introduced in this work. The initial state of a wave field inside a bounded propagation domain can be reconstructed from temporal measurements of the wave field evolution at discrete locations. Time reversal enables the spatial and temporal focusing of mechanical waves using a set of remote transducers in a reverberating, dispersive, and even scattering medium, as long as it is stationary. A model of the focus point's width, which is the spatial resolution of the system, is proposed based on Kirchhoff's wave propagation theory. The main parameters influencing the spatial resolution are the driving signals' mean frequency and the plate's geometry and material. The low frequency bands of the driving signals amplify the displacement amplitude. However noise in the audible range is increased. The targeted spatial resolution for tactile stimulation is 5 mm. This requires a mean frequency of about 65 kHz for the driving signals. As for the focus point's displacement amplitude, it increases with a reduction of the plate's thickness. A wider frequency band and a larger number of actuators allow to produce a higher displacement amplitude and a better contrast ratio. It however requires a more complex driving electronics. To design a haptic interface based on time reversal, design guidelines are provided in this thesis. Parameters such as the area, thickness and material characteristics of the plate are considered as input. The targeted spatial resolution defines the mean frequency of the driving signal, based on the model introduced in this work. The plate dimensions and material set the characteristic time T_c of the plate. The maximum contrast that can be achieved depends on T_c and the signal bandwidth B. The plate attenuation constant τ can then be determined through experimental measurements. Finally the reversal time T and the repetition time T_r should satisfy $\tau \leq T \leq T_r$.

Based on the proposed design guidelines, a novel prototype using time reversal is designed. Compromises are made between the necessity of mechanical robustness, i.e. a thicker surface, and large deformations, which means a thinner surface. The

proposed tactile display is made of glass, has a surface area of 300 by 200 mm^2 and is 1.1 mm thick. 32 piezoelectric circular transducers (ϕ 10 mm) are glued on the four sides. Electronics based on the class-D amplifier principle is used to drive the transducers. Different driving signals are tested and compared including filtered and unfiltered driving signals either quantified on one bit or Sigma-Delta modulated. Filtering the audible frequencies out of the driving signals proved to be an interesting approach as it results in lower noise while maintaining an acceptable generated amplitude. The Sigma-Delta modulation is then compared to quantification on one bit. While Sigma-Delta modulation is an efficient approach to reduce noise emission, it does not result in large amplitudes. Moreover, modulating the driving signals increases the energy consumption as compared to signals quantified on one bit. The best choice in terms of driving signals is therefore signals quantified on one bit with audible frequencies filtered out. No substantial impact or direct correlation between the focus point location and the transducers location is found. This conclusion can lead to better integrated designs. The 32 actuators could be located on only one side of the plate without deteriorating the focalisation process. Both the spatial resolution and the amplitudes are almost constant and homogeneous all over the display surface.

Furthermore, the performance of time reversal method has been evaluated through user experiments. The loss in focalisation amplitude is investigated as a function of applied force by the user. On the one hand, diffraction losses resulting from a finger applying a 2 N force at a location other than the focusing point does not exceed 6% of the amplitude loss. On the other hand, an applied force of 2 N at focus can result in a decrease of up to 30% of the impact's amplitude. The detection threshold is measured in a user study. It is found that the applied force has little influence on the perception threshold. An amplitude of 10 µm appears to be the minimum amplitude that is well detected by all the users. While a single impact demonstrates the feasibility of time reversal, a repetition of impacts modulated in amplitude can provide a variety of key-click feedback. A study comparing different patterns with higher (500 Hz) and lower (200 Hz) frequencies and several types of envelopes using the AttrakDiff questionnaire is proposed. Lower frequencies are preferred (200 Hz) and the smoothness of the cardinal sine envelope is found to be the best in terms of pleasantness.

Electrovibration is able to generate a "texture" feedback. The working principle relies on the application of an electrostatic force between the finger and the screen. This force modifies the apparent friction coefficient of the surface when a finger dynamically explores a surface. The electrostatic force depends on the fingertip skin's thickness which varies from person to person and the contact area that depends on the applied force. Moreover, mechanoreceptors are known to have frequency dependent detection thresholds. For these reasons, a user study on the influence of the applied force on the perception threshold is presented. Users are asked to follow a moving cursor displayed on a haptic screen while applying three different force levels. Five signals with different frequencies, 100 Hz, 160 Hz, 240 Hz, 360 Hz and 540 Hz respectively, are tested. The applied forces are divided into three intervals, "light", "medium" and "high" based on the results of a first study. For all the force intervals, the perception threshold reaches a minimum at the 240 Hz stimulus. This frequency dependence is confirmed to be significant by an analysis of variance (ANOVA) and fits well with the human tactile sensitivity peak. However,

the effect of the force with an ANOVA concludes to a non significant effect. The mean perception thresholds are similar across the three force intervals for the lower frequencies (100 Hz to 240 Hz). Above the 240 Hz frequency, the mean perception thresholds tend to decrease with the increase in force. Further user studies are still required in order to confirm these results.

7.1 Future work

Future work on time reversal should focus on modelling, noise emission, power consumption and optimised patterns. The proposed design guidelines in this work enable to design a time reversal haptic interface. One limitation however is the need to experimentally measure the attenuation constant of the plate. Proposing a model that is able to predict the attenuation constant τ for different boundary conditions would represent a significant contribution to the design guidelines. In addition, another valuable predictive model would be the estimation of the displacement amplitude for different plate materials and thicknesses. Another important challenge for the integration of time reversal in handheld devices is noise reduction. Improving the driving electronics and the input signals as well as optimising the boundary conditions will allow to reduce the noise emission. The piezoelectric transducers can also be further optimised in terms of geometry and materials. A microfabrication process allowing to depose piezoelectric material in thin layers should lead to better coupling and reduced power consumption. Further studies on haptic patterns with different envelopes and a broader population should lead to clear and pleasant feedback patterns. A real-time control of the envelope shape as a function of the applied force might lead to haptic feedback with enhanced performance.

While it has been demonstrated that electrovibration feedback emulates different surface roughnesses, more research on the specific signals, varying frequencies and amplitudes is still needed to reproduce "realistic" textures. Moreover, further optimisation of insulating material with higher electrical permittivity and lower thicknesses will reduce the driving voltage and make it compatible with mobile electronics requirements. Multi-point feedback based on electrovibration remains a challenge. By designing specific electrode patterns and developing tailored fabrication processes, a localised electrovibration stimulus could be achieved.

Finally, the combination of the presented feedback approaches should provide simultaneous key-click and texture feedback. Due to the different physical phenomena involved in time reversal and electrovibration, no cross-talk is expected when both are stacked in a single display. This unique combination should lead to high quality haptic feedback.

Appendix A

Pattern study detailed results

Figure A.1 details the scores of pattern 0 (single impact). It is considered the second least in terms of simplicity (0.9), straightforwardness (1.4), predictability (0.5) and clarity (1.2). It is considered averagely inventive (0.5) and captivating (0.7). It fares better than average in terms of novelty (0.6), stylishness (1.1), premium feeling (1.3) and presentability (1.5). It is least pleasant than average (0.5). It is average in attractive (0.9), likeable (0.8), appealing (0.5) and good (0.8). It is the second least inviting (0.3) and motivating pattern (0). A strong single impact represents a quite clear and straightforward signal as one could expect. But it not very pleasant. And it is clearly not inviting.

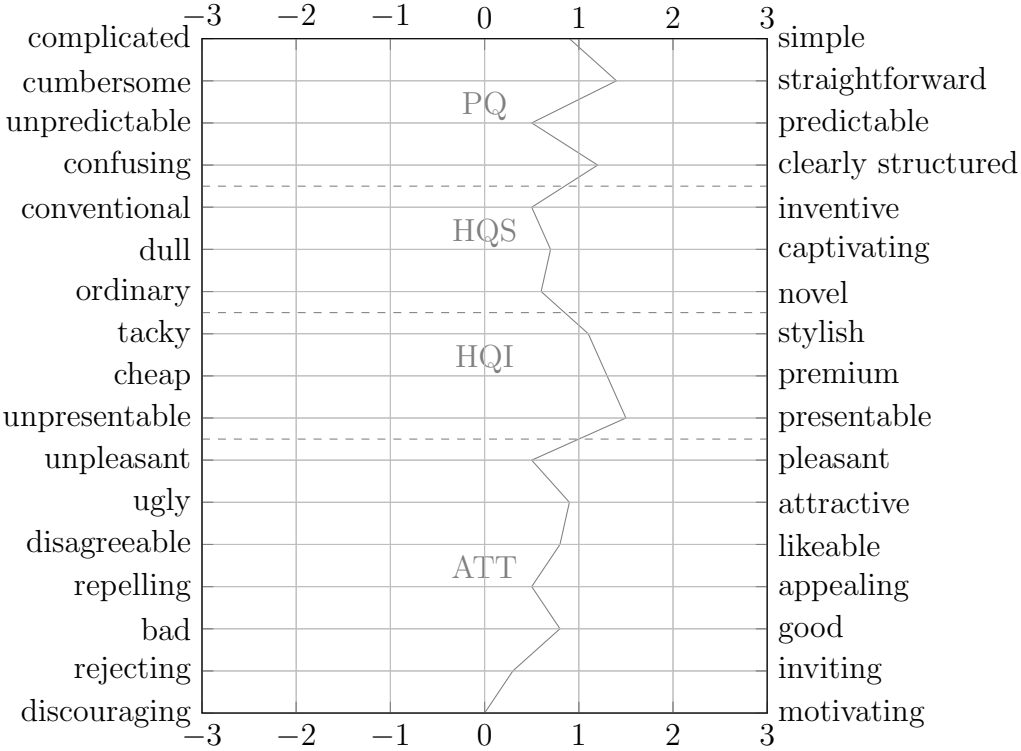

Figure A.1: Pattern P_0 - score on the AttrakDiff inspired scale.

Figure A.2 details the scores of pattern 1 (square, 200 Hz). It is the least simple (0.5) and predictable (0.4) of the patterns. It scores above average in terms of straightforwardness (2) and inventiveness (0.8). It is only average in clarity (1.3)

and novelty (0.4). It is however the most captivating pattern (1.4). It is second in terms of stylishness (1.2) and premium feel (1.4). It is average in presentable (1), pleasant (0.8), attractive (0.9). It is second in likeable (0.7), appealing (0.9), good (0.9) and inviting (0.8). It is averagely motivating (0.1). The square envelope at low frequency is the most captivating pattern. It fares rather good in terms of premium feeling, appealing but only average in pleasantness.

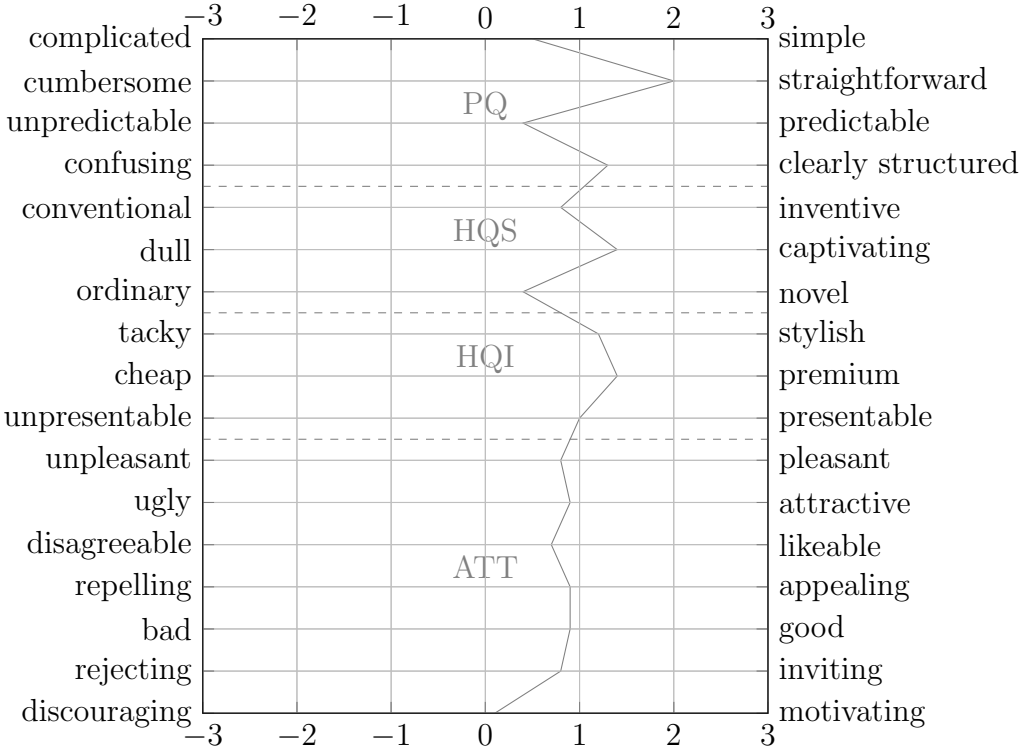

Figure A.2: Pattern P_1 - score on the AttrakDiff inspired scale.

Figure A.3 details the scores of pattern 2 (Cardinal sinus, 200 Hz). It is averagely simple (1.4). It is above average in terms of predictability (1.5) and captivating (1). It is second in straightforwardness (2.1). It ranks first in every other category : clearly structured (1.8), inventive (1), novel (0.8), stylish (1.5), premium (1.5), presentable (1.9), pleasant (1.4), attractive (1.8), likeable (1.5), appealing (1.2), good (1.5), inviting (1.3) and motivating (0.9). The cardinal sinus envelope at low frequency leads clearly in terms of pleasantness and clarity but lacks a bit in simplicity.

Figure A.4 details the scores of pattern 3 (Decreasing exponential, 200 Hz). It is the least straightforward (0.4) and captivating (0.2). It is second in pleasant (1.2), attractive (1.1), likeable (1.2), good (0.9) and motivating (0.6). It is average in every other category : simple (1.6), predictable (1.3), clearly structured (1.4), inventive (0.4), novel (0.2), stylish (0.8), premium (1.2), presentable (1.2), appealing (0.8) and inviting (0.6). The decreasing exponential envelope at low frequency is clearly not straightforward or captivating and only average in the other categories.

Figure A.5 details the scores of pattern 4 (square, 500 Hz). It is the second simplest (1.8) pattern. With a 2.4 score in straightforwardness, P_4 is considered as the most easy to comprehend pattern. It is also the most predictable (1.7) and clear (1.8). It is however the least pleasant (0.1), the second least attractive

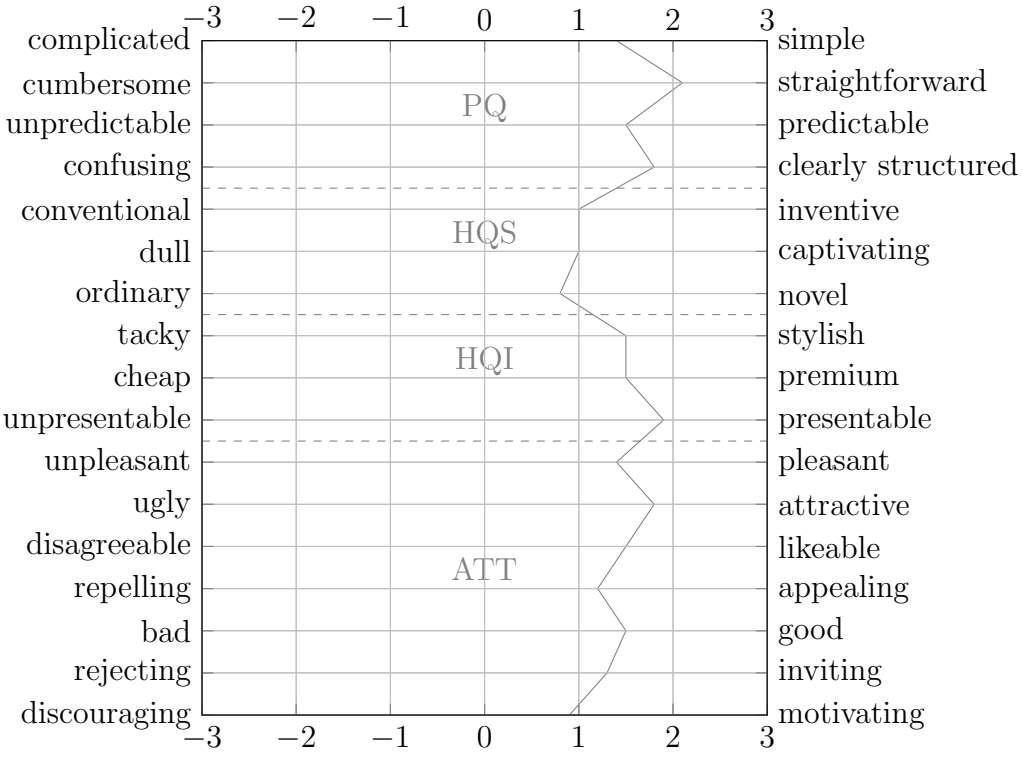

Figure A.3: Pattern P_2 - score on the AttrakDiff inspired scale.

(0.4) and the least likeable (0), appealing (-0.2), good (0.5), inviting (-0.1) and motivating (-0.3) altogether. It seems that efficiency and pleasantness are opposed optimums. Its other characteristics are average compared to the other patterns : inventive (0.4), captivating (0.8), novel (0.1), stylish (0.5), premium (0.8) and presentable (1.3). The square envelope at high frequency results in higher simplicity and straightforwardness scores than its low frequency counterpart. But its ranking in terms of pleasantness or appeal fall behind.

Figure A.6 details the scores of pattern 5 (Cardinal sinus, 500 Hz). It is the second in the category clearly structured (1.6), captivating (1.2) and novel (0.6). It is the least good (0.4). It is the second least premium (0.6), pleasant (0.2) and likeable (0.3) and inviting (0.3). It fares average in the remaining categories : simple (1.1), straightforward (1.9), predictable (0.8), inventive (0.8), stylish (0.7), presentable (1.7), attractive (0.5), appealing (0.5) and motivating (0.6). The cardinal sinus envelope at high frequency follows similar ratings in terms of straightforwardness or clarity compared to its lower frequency counterpart but lower. It seems to follow a trend in the rest of the categories similar to P_4.

Figure A.7 details the scores of pattern 6 (Decreasing exponential, 500 Hz). It is rated the most simple (2) pattern. It is the second most predictable (1.6). It is the least clearly structured (0.6), inventive (-0.3), novel (-0.3), premium (0.4), presentable (0.8), attractive (0.2) and good (0.4). It is the second least in stylish (0.6) and likeable (0.4). It fares averagely in the other categories : straightforward (1.5), captivating (0.8), pleasant (0.7), appealing (0.4), inviting (0.4) and motivating (0.2). The decreasing exponential at high frequency follows similar but better ratings in simplicity and straightforwardness compared to its lower frequency counterpart. But in the rest of the categories it has lower ratings.

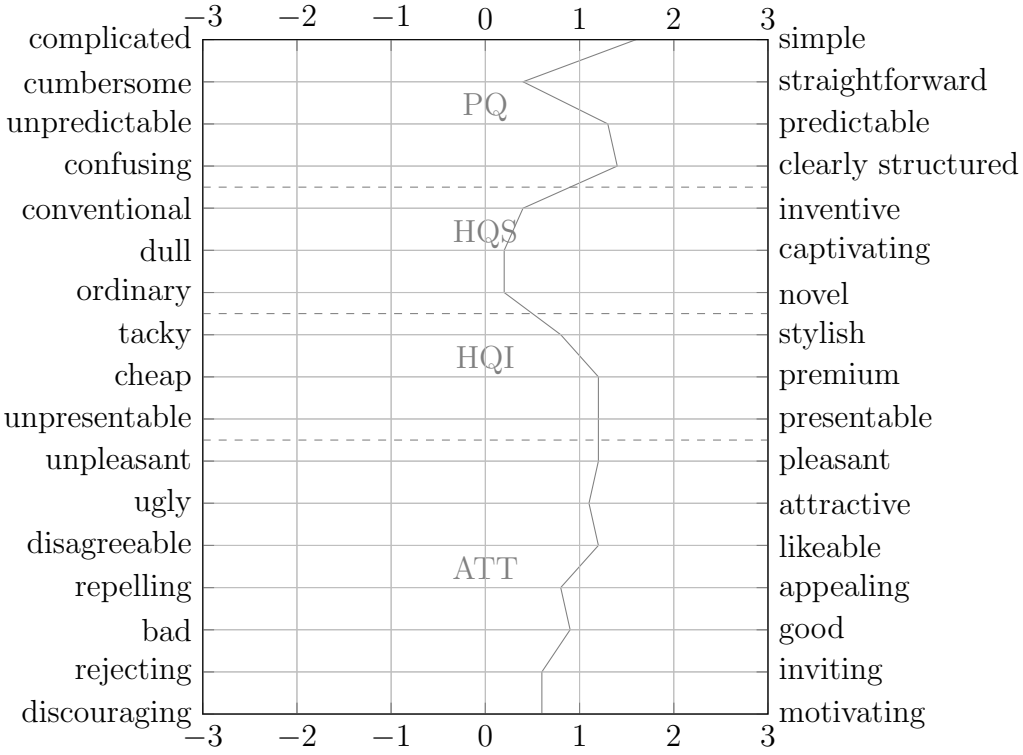

Figure A.4: Pattern P_3 - score on the AttrakDiff inspired scale.

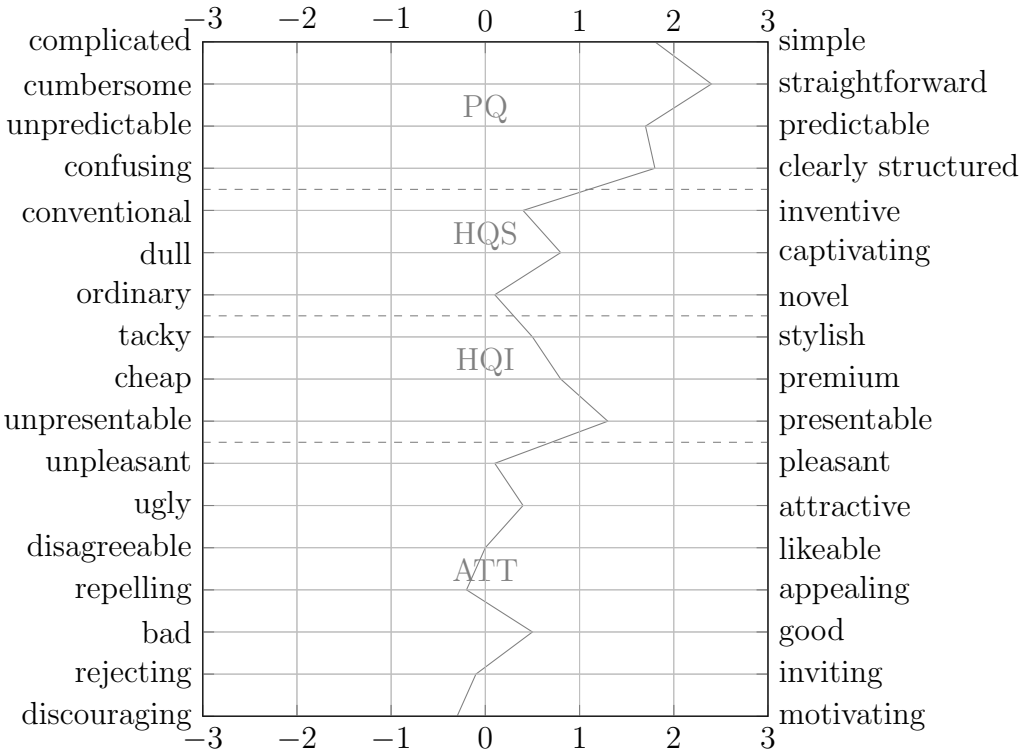

Figure A.5: Pattern P_4 - score on the AttrakDiff inspired scale.

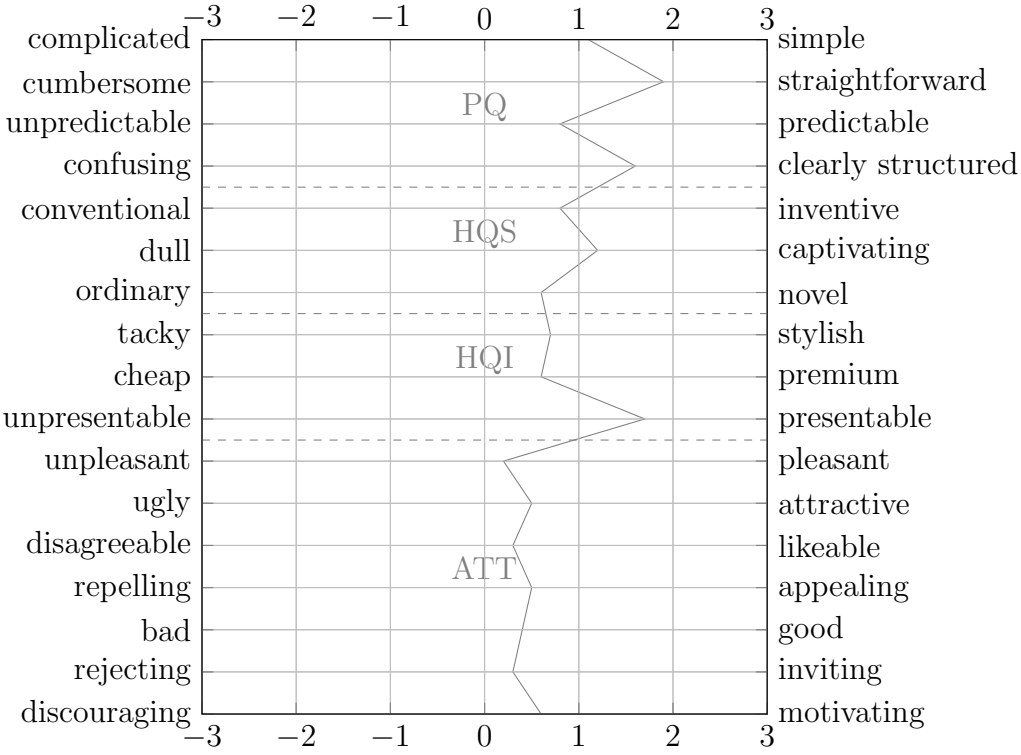

Figure A.6: Pattern P_5 - score on the AttrakDiff inspired scale.

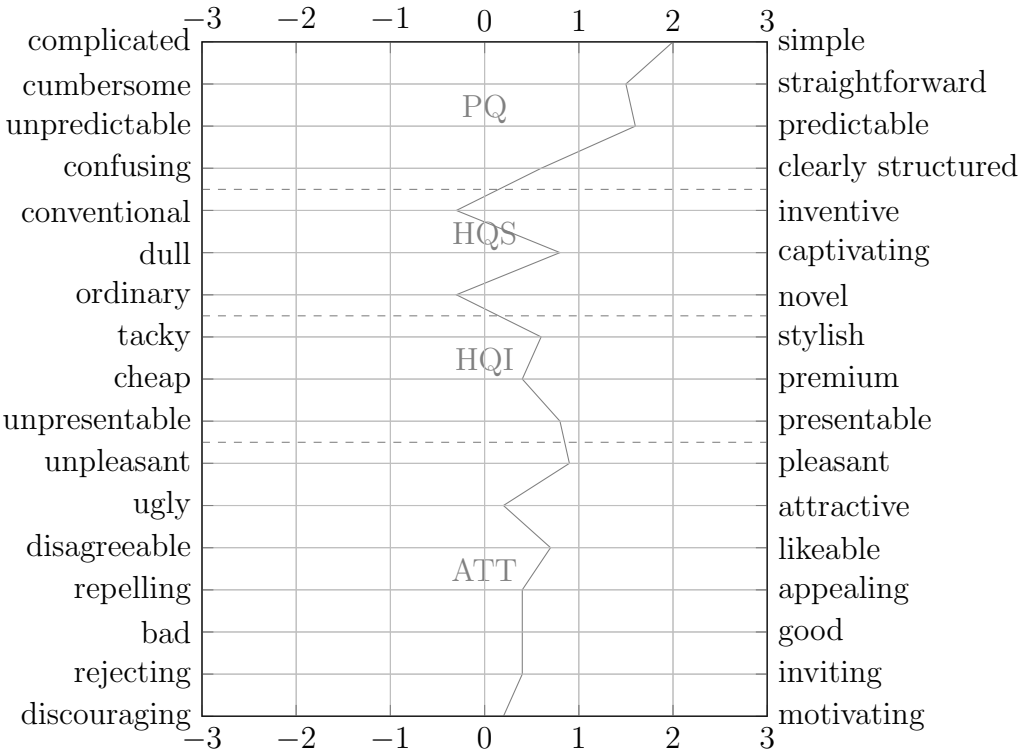

Figure A.7: Pattern P_6 - score on the AttrakDiff inspired scale.

Appendix B

Finger contact surface estimation

In this section, experimental measurements are carried out to determine the influence of applied force on the contact surface of the fingertip.

B.1 Experimental set-up

To estimate the finger's surface of contact as a function of applied force the following experiment is carried out. A paper is laid on a force sensor. A finger is inked and then presses the paper. Measurements are carried out for the range of forces used in chapter 6 (0.2 N, 1.5 N, 3.0 N and 7.0 N). Figure B.1 presents the inks marks obtained.

Figure B.1: Inked surface of paper as a function of applied force (from left to right, 0.2 N, 1.5 N, 3.0 N and 7.0 N).

The different inked surfaces are measured by assimilating them to elipsoids. The lengths of the semi-major and semi-minor axis (respectively a_M and a_m, see Figure B.2) are measured on the inked paper and the surface is given by:

$$S_{ellipse} = \pi \cdot a_M \cdot a_m \tag{B.1}$$

B.2 Results

The measurements are presented in Figure B.3. For the measured forces, the contact surface of the finger increases with the applied force. The increase is regular from 0.2 N ($S_{contact}$=132 mm^2) to 3.0 N ($S_{contact}$=231 mm^2). For higher forces the surface still increases but slower and reaches 271 mm^2 for a 7.0 N force.

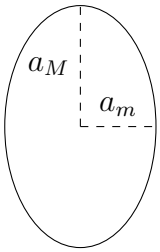

Figure B.2: Surface of an ellipse.

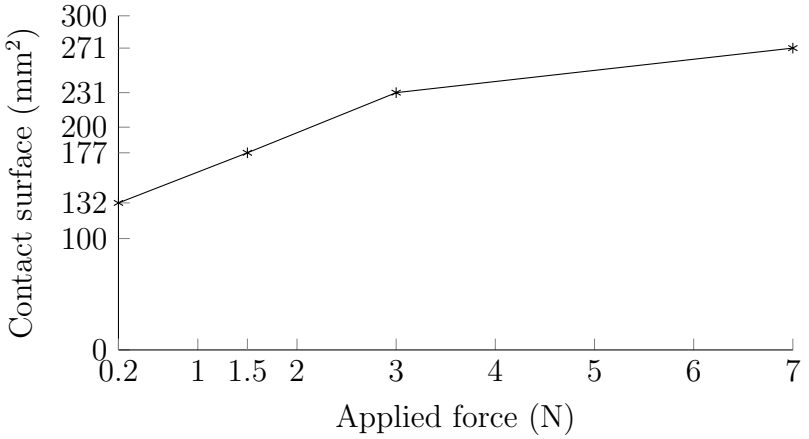

Figure B.3: Contact surface of the finger as a function of applied force.

This experiment presents measurements of the variation of contact area between the fingertip and the haptic screen as a function of applied force. It shows that applied pressure increases the contact area. The variation is non linear. From the light force level to the medium force level the variation in contact area is higher than from the medium force level to the high force level. An increase in contact area results in an increase in generated electrostatic force. This could explain to a certain degree the previously measured variation of perception threshold as a function of applied force. The perception thresholds tend to decrease with the increase from light applied force to medium applied force. The increase in generated electrostatic force due to the increase in contact surface could be the reason of the perception threshold decrease. For high forces, the increase in generated electrostatic force is low enough to not be noticeable in the perception threshold variation.

Bibliography

[1] Keiiti Aki. Space and time spectra of stationary stochastic waves, with special reference to microtremors. *Bulletin Earthquake Research Institut*, 35, 01 1957.

[2] Olivier Bau and Ivan Poupyrev. Revel: tactile feedback technology for augmented reality. *ACM Trans. Graph.*, 31(4):89:1–89:11, jul 2012.

[3] Olivier Bau, Ivan Poupyrev, Ali Israr, and Chris Harrison. Teslatouch: electrovibration for touch surfaces. In *Proceedings of the 23nd annual ACM symposium on User interface software and technology*, UIST '10, pages 283–292, New York, NY, USA, 2010. ACM.

[4] Mohamed Benali-Khoudja, Moustapha Hafez, and Abderrahmane Kheddar. Vital: An electromagnetic integrated tactile display. *Displays*, 28(3):133–144, 2007.

[5] Lapo Boschi, Cornelis Weemstra, Julie Verbeke, Göran Ekström, Andrea Zunino, and Domenico Giardini. On measuring surface wave phase velocity from station-station cross-correlation of ambient signal. *Geophysical Journal International*, 192:346–358, 2013.

[6] W Brenner, S Mitic, A Vujanic, and G Popovic. Micro-actuation principles for high-resolution graphic tactile displays. In *Proceedings of Eurohaptics*, 2001.

[7] Lorna Margaret Brown. *Tactons: structured vibrotactile messages for non-visual information display.* 2007.

[8] Marie-Ange Bueno, Betty Lemaire-Semail, Michel Amberg, and Frédéric Giraud. A simulation from a tactile device to render the touch of textile fabrics: a preliminary study on velvet. *Textile Research Journal*, 0:1–13, 2014.

[9] Géry Casiez, Nicolas Roussel, Romuald Vanbelleghem, and Frédéric Giraud. Surfpad: riding towards targets on a squeeze film effect. In *Proceedings of the SIGCHI Conference on Human Factors in Computing Systems*, CHI '11, pages 2491–2500, New York, NY, USA, 2011. ACM.

[10] D. Cassereau and M. Fink. Time-reversal of ultrasonic fields. iii. theory of the closed time-reversal cavity. *Ultrasonics, Ferroelectrics, and Frequency Control, IEEE Transactions on*, 39(5):579–592, Sept 1992.

[11] Hsiang-Yu Chen, Jaeyoung Park, S. Dai, and H.Z. Tan. Design and evaluation of identifiable key-click signals for mobile devices. *Haptics, IEEE Transactions on*, 4(4):229–241, 2011.

[12] Cherry. Cherry Mx. `http://cherryamericas.com/product/mx-series-2/`. Accessed: 2017-02-21.

[13] Edward J. Colgate, Michael Peshkin, Xiaowei Dai, John Ware, and Nicholas Marchuk. Touch interface device and method for applying lateral forces on a human appendage, December 2012.

[14] Corning. Corning Gorilla Glass 5. `https://www.corning.com/microsites/csm/gorillaglass/PI_Sheets/Corning%20Gorilla%20Glass%205%20PI%20Sheet.pdf`. Accessed: 2017-02-21.

[15] Xiaowei Dai, J.E. Colgate, and M.A. Peshkin. Lateralpad: A surface-haptic device that produces lateral forces on a bare finger. In *Haptics Symposium (HAPTICS), 2012 IEEE*, pages 7–14, 2012.

[16] Xiaowei Dai, Jiawei Gu, Xiang Cao, J. Edward Colgate, and Hong Tan. Slickfeel: sliding and clicking haptic feedback on a touchscreen. In *Adjunct proceedings of the 25th annual ACM symposium on User interface software and technology*, UIST Adjunct Proceedings '12, pages 21–22, New York, NY, USA, 2012. ACM.

[17] Arnaud Derode, Arnaud Tourin, and Mathias Fink. Ultrasonic pulse compression with one-bit time reversal through multiple scattering. *Journal of applied physics*, 85(9):6343–6352, 1999.

[18] Arnaud Derode, Arnaud Tourin, and Mathias Fink. Limits of time-reversal focusing through multiple scattering: Long-range correlation. *The Journal of the Acoustical Society of America*, 107(6):2987–2998, 2000.

[19] Carsten Draeger, Jean-Christian Aime, and Mathias Fink. One-channel time-reversal in chaotic cavities: Experimental results. *The Journal of the Acoustical Society of America*, 105(2):618–625, 1999.

[20] Ferroperm. Ferroperm Piezoelectric material datasheet. `http://www.ferroperm-piezo.com/files/files/Ferroperm%20MatData.xls`. Accessed: 2017-02-21.

[21] M. Fink. Time reversal of ultrasonic fields. i. basic principles. *Ultrasonics, Ferroelectrics, and Frequency Control, IEEE Transactions on*, 39(5):555–566, Sept 1992.

[22] Sean Follmer, Daniel Leithinger, Alex Olwal, Akimitsu Hogge, and Hiroshi Ishii. inform: dynamic physical affordances and constraints through shape and object actuation. In *Proceedings of the 26th annual ACM symposium on User interface software and technology*, pages 417–426. ACM, 2013.

[23] H. Fruhstorfer, U. Abel, C.-D. Garthe, and A. KnÃŒttel. Thickness of the stratum corneum of the volar fingertips. *Clinical Anatomy*, 13(6):429–433, 2000.

[24] T. Fukuda, H. Morita, F. Arai, H. Ishihara, and H. Matsuura. Micro resonator using electromagnetic actuator for tactile display. In *1997 International Symposium on Micromechanics and Human Science (Cat. No.97TH8311)*, pages 143–148, 1997.

[25] Esther P Gardner and John H Martin. Coding of sensory information. *Principles of neural science*, 4:411–429, 2000.

[26] George A. Gescheider, Stanley J. Bolanowski, Jennifer V. Pope, and Ronald T. Verrillo. A four-channel analysis of the tactile sensitivity of the fingertip: frequency selectivity, spatial summation, and temporal summation. *Somatosensory & Motor Research*, 19(2):114–124, 2002.

[27] S. Ghenna, F. Giraud, C. Giraud-Audine, M. Amberg, and B. Lemaire-Semail. Preliminary design of a multi-touch ultrasonic tactile stimulator. In *World Haptics Conference (WHC), 2015 IEEE*, pages 31–36, June 2015.

[28] F. Giraud, M. Amberg, B. Lemaire-Semail, and G. Casiez. Design of a transparent tactile stimulator. In *Haptics Symposium (HAPTICS), 2012 IEEE*, pages 485–489, 2012.

[29] Frederic Giraud, Michel Amberg, and Betty Lemaire-Semail. Merging two tactile stimulation principles: electrovibration and squeeze film effect. In *World Haptics Conference (WHC), 2013*, pages 199–203, 2013.

[30] Franck Gonzalez, Florian Gosselin, and Wael Bachta. Analysis of hand contact areas and interaction capabilities during manipulation and exploration. *IEEE transactions on haptics*, 7(4):415–429, 2014.

[31] S. Grimnes. Electrovibration, cutaneous sensation of microampere current. *Acta Physiologica Scandinavica*, 118(1):19–25, May 1983.

[32] Hiroshi Haga, Kazuhide Yoshinaga, Jiro Yanase, Daisuke Sugimoto, Kenichi Takatori, and Hideki Asada. Electrostatic tactile display using beat phenomenon for stimulus localization. *IEICE Transactions on Electronics*, E98.C(11):1008–1014, 2015.

[33] Chris Harrison and Scott E. Hudson. Providing dynamically changeable physical buttons on a visual display. In *Proceedings of the SIGCHI Conference on Human Factors in Computing Systems*, CHI '09, pages 299–308, New York, NY, USA, 2009. ACM.

[34] Marc Hassenzahl, Michael Burmester, and Franz Koller. *AttrakDiff: Ein Fragebogen zur Messung wahrgenommener hedonischer und pragmatischer Qualität*, pages 187–196. Vieweg+Teubner Verlag, Wiesbaden, 2003.

[35] Eve Hoggan, Stephen A. Brewster, and Jody Johnston. Investigating the effectiveness of tactile feedback for mobile touchscreens. In *Proceedings of the SIGCHI Conference on Human Factors in Computing Systems*, CHI '08, pages 1573–1582, New York, NY, USA, 2008. ACM.

[36] Mark Hollins, SJ Bensmaıa, and EA Roy. Vibrotaction and texture perception. *Behavioural brain research*, 135(1):51–56, 2002.

[37] Mark Hollins and S.Ryan Risner. Evidence for the duplex theory of tactile texture perception. *Perception & Psychophysics*, 62(4):695–705, 2000.

[38] C. Hudin, J. Lozada, and V. Hayward. Localized tactile stimulation by time-reversal of flexural waves: Case study with a thin sheet of glass. In *Proceedings of the IEEE World Haptics Conference 2013*, pages 67–72, 2013.

[39] C. Hudin, J. Lozada, and V. Hayward. Localized tactile feedback on a transparent surface through time-reversal wave focusing. *IEEE Transactions on Haptics*, 8(2):188–198, April 2015.

[40] Charles Hudin. *Time reversal focusing in thin plates : application to tactile stimulation*. Theses, Université Pierre et Marie Curie - Paris VI, March 2014.

[41] Charles Hudin, José Lozada, Michael Wiertlewski, and Vincent Hayward. Tradeoffs in the application of time-reversed acoustics to tactile stimulation. In Poika Isokoski and Jukka Springare, editors, *Haptics: Perception, Devices, Mobility, and Communication*, volume 7282 of *Lecture Notes in Computer Science*, pages 218–226. Springer Berlin Heidelberg, 2012.

[42] Humanware. Humanware Braille display. `http://store.humanware.com/france/brailliant-bi-32-new-generation.html`. Accessed: 2017-02-16.

[43] A. Israr, Seungmoon Choi, and H.Z. Tan. Detection threshold and mechanical impedance of the hand in a pen-hold posture. In *Intelligent Robots and Systems, 2006 IEEE/RSJ International Conference on*, pages 472–477, Oct 2006.

[44] Yvonne Jansen, Thorsten Karrer, and Jan Borchers. Mudpad: tactile feedback and haptic texture overlay for touch surfaces. In *ACM International Conference on Interactive Tabletops and Surfaces*, ITS '10, pages 11–14, New York, NY, USA, 2010. ACM.

[45] Roland S Johansson and Åke B Vallbo. Tactile sensory coding in the glabrous skin of the human hand. *Trends in neurosciences*, 6:27–32, 1983.

[46] Kenneth O Johnson. The roles and functions of cutaneous mechanoreceptors. *Current opinion in neurobiology*, 11(4):455–461, 2001.

[47] Kenneth O Johnson, Takashi Yoshioka, and Francisco Vega-Bermudez. Tactile functions of mechanoreceptive afferents innervating the hand. *Journal of Clinical Neurophysiology*, 17(6):539–558, 2000.

[48] T. Kaaresoja and J. Linjama. Perception of short tactile pulses generated by a vibration motor in a mobile phone. In *First Joint Eurohaptics Conference and Symposium on Haptic Interfaces for Virtual Environment and Teleoperator Systems. World Haptics Conference*, pages 471–472, March 2005.

[49] K.A. Kaczmarek, K. Nammi, A.K. Agarwal, M.E. Tyler, S.J. Haase, and D.J. Beebe. Polarity effect in electrovibration for tactile display. *Biomedical Engineering, IEEE Transactions on*, 53(10):2047–2054, 2006.

[50] H. Kajimoto. Electrotactile display with real-time impedance feedback using pulse width modulation. *Haptics, IEEE Transactions on*, 5(2):184–188, 2012.

[51] Hiroyuki Kajimoto. Skeletouch: Transparent electro-tactile display for mobile surfaces. In *SIGGRAPH Asia 2012 Emerging Technologies*, SA '12, pages 21:1–21:3, New York, NY, USA, 2012. ACM.

[52] James Robert Karamath, Christopher James Brown, Sergio Garcia Castillo, and Harry Garth Walton. Touchscreen device including tactile feedback actuator, November 2013.

[53] Sang-Youn Kim, Jae-Oh Kim, and Kyu Kim. Traveling vibrotactile wave - a new vibrotactile rendering method for mobile devices. *Consumer Electronics, IEEE Transactions on*, 55(3):1032–1038, 2009.

[54] Seung-Chan Kim, Ali Israr, and Ivan Poupyrev. Tactile rendering of 3d features on touch surfaces. In *Proceedings of the 26th annual ACM symposium on User interface software and technology*, UIST '13, pages 531–538, New York, NY, USA, 2013. ACM.

[55] Sunjun Kim and Geehyuk Lee. Haptic feedback design for a virtual button along force-displacement curves. In *Proceedings of the 26th annual ACM symposium on User interface software and technology*, UIST '13, pages 91–96, New York, NY, USA, 2013. ACM.

[56] Hiroyuki Kotani, Masaya Takasaki, and Takeshi Mizuno. Friction measurement on a glass substrate using surface acoustic wave. *Physics Procedia*, 3(1):1067–1073, 2010. International Congress on Ultrasonics, Santiago de Chile, January 2009.

[57] Ki-Uk Kyung, Jong-uk Lee, Suntak Park, Harsha Prahlad, and Philip Guggenberg. Flexible visio-haptic display. In Poika Isokoski and Jukka Springare, editors, *Haptics: Perception, Devices, Mobility, and Communication*, volume 7283 of *Lecture Notes in Computer Science*, pages 206–209. Springer Berlin Heidelberg, 2012.

[58] Vincent Levesque, Louise Oram, Karon MacLean, Andy Cockburn, Nicholas D. Marchuk, Dan Johnson, J. Edward Colgate, and Michael A. Peshkin. Enhancing physicality in touch interaction with programmable friction. In *Proceedings of the SIGCHI Conference on Human Factors in Computing Systems*, CHI '11, pages 2481–2490, New York, NY, USA, 2011. ACM.

[59] Edward Mallinckrodt, A. L. Hughes, and William Sleator. Perception by the skin of electrically induced vibrations. *Science*, 118(3062):277–278, 1953.

[60] N.D. Marchuk, J.E. Colgate, and M.A. Peshkin. Friction measurements on a large area tpad. In *Haptics Symposium, 2010 IEEE*, pages 317–320, 2010.

[61] David J. Meyer, Michael A. Peshkin, and J.Edward Colgate. Fingertip friction modulation due to electrostatic attraction. In *World Haptics Conference (WHC), 2013*, pages 43–48, 2013.

[62] D.J. Meyer, M. Wiertlewski, M.A. Peshkin, and J.E. Colgate. Dynamics of ultrasonic and electrostatic friction modulation for rendering texture on haptic surfaces. In *Haptics Symposium (HAPTICS), 2014 IEEE*, pages 63–67, Feb 2014.

[63] J. Mullenbach, D. Johnson, J.E. Colgate, and M.A. Peshkin. Activepad surface haptic device. In *Haptics Symposium (HAPTICS), 2012 IEEE*, pages 407–414, 2012.

[64] Taku Nakamura and Akio Yamamoto. Multi-finger electrostatic passive haptic feedback on a visual display. In *World Haptics Conference (WHC), 2013*, pages 37–42, 2013.

[65] Knight Optical. Knight Optical - Schott B270. `https://psec.uchicago.edu/glass/Schott%20B270%20Properties%20-%20Knight%20Optical.pdf`. Accessed: 2017-02-21.

[66] Jérôme Pasquero and Vincent Hayward. Stress: A practical tactile display system with one millimeter spatial resolution and 700 hz refresh rate. In *in Proc. Eurohaptics 2003*, pages 94–110, 2003.

[67] Ivan Poupyrev, Shigeaki Maruyama, and Jun Rekimoto. Ambient touch: designing tactile interfaces for handheld devices. In *Proceedings of the 15th annual ACM symposium on User interface software and technology*, UIST '02, pages 51–60, New York, NY, USA, 2002. ACM.

[68] GB) Radivojevic, Zoran (Cambridge, GB) Beecher, Paul (Cambridge, GB) Bower, Chris (Ely, and GB) Andrew, Piers (Cambridge. Surface texture recording with microphone, September 2012.

[69] Guillemette Ribay, Stefan Catheline, Dominique Clorennec, R Kiri Ing, Nicolas Quieffin, and Mathias Fink. Acoustic impact localization in plates: properties and stability to temperature variation. *IEEE transactions on ultrasonics, ferroelectrics, and frequency control*, 54(2):378–385, 2007.

[70] Gabriel Robles-De-La-Torre and Vincent Hayward. Force can overcome object geometry in the perception of shape through active touch. *Nature*, 412(6845):445–448, jul 2001.

[71] Satoshi Saga and Ramesh Raskar. Simultaneous geometry and texture display based on lateral force for touchscreen. In *World Haptics Conference (WHC), 2013*, pages 437–442, 2013.

[72] Ping Sheng. Introduction to wave scattering, localization, and mesoscopic phenomena. *Academic Press*, 1995.

[73] Andrew A. Stanley, James C. Gwilliam, and Allison M. Okamura. Haptic jamming: A deformable geometry, variable stiffness tactile display using pneumatics and particle jamming. In *World Haptics Conference (WHC), 2013*, pages 25–30, 2013.

[74] R.M. Strong and D. Troxel. An electrotactile display. *Man-Machine Systems, IEEE Transactions on*, 11(1):72–79, 1970.

[75] Ian R Summers. *Tactile aids for the hearing impaired*. Whurr Publishers London, 1992.

[76] Tactus. Tactus tactile overlay. `http://www.tactustechnology.com`. Accessed: 2014-03-20.

[77] P.M. Taylor, D.M. Pollet, A. Hosseini-Sianaki, and C.J. Varley. Advances in an electrorheological fluid based tactile array. *Displays*, 18(3):135–141, 1998.

[78] R. Velazquez, E. Pissaloux, J. Szewczyk, and M. Hafez. Miniature shape memory alloy actuator for tactile binary information display. In *Robotics and Automation, 2005. ICRA 2005. Proceedings of the 2005 IEEE International Conference on*, pages 1344–1349, 2005.

[79] Ronald T Verrillo. Vibrotactile thresholds measured at the finger. *Perception & Psychophysics*, 9(4):329–330, 1971.

[80] Eric Vezzoli, Michel Amberg, Frédéric Giraud, and Betty Lemaire-Semail. Electrovibration modeling analysis. In Malika Auvray and Christian Duriez, editors, *Haptics: Neuroscience, Devices, Modeling, and Applications*, Lecture Notes in Computer Science, pages 369–376. Springer Berlin Heidelberg, 2014.

[81] Fernando Vidal-Verdu, Rafael Navas-Gonzalez, and Maria José Barquerro. Thermal modelling of a thermopneumatic actuator. In *Integrated Sensors and Mems coonference*, 2003.

[82] Christopher R Wagner, Susan J Lederman, and Robert D Howe. A tactile shape display using rc servomotors. In *Haptic Interfaces for Virtual Environment and Teleoperator Systems, 2002. HAPTICS 2002. Proceedings. 10th Symposium on*, pages 354–355. IEEE, 2002.

[83] Michael Wiertlewski, J. Lozada, and V. Hayward. The spatial spectrum of tangential skin displacement can encode tactual texture. *Robotics, IEEE Transactions on*, 27(3):461–472, 2011.

[84] Markus Wiesendanger. Squeeze film air bearings using piezoelectric bending elements. *Ecole Polytechnique Fdrale de Lausanne, Lausanne: EPFL*, 2001.

[85] L. Winfield, J. Glassmire, J.E. Colgate, and M. Peshkin. T-pad: Tactile pattern display through variable friction reduction. In *EuroHaptics Conference, 2007 and Symposium on Haptic Interfaces for Virtual Environment and Teleoperator Systems. World Haptics 2007. Second Joint*, pages 421–426, 2007.

[86] A. Yamamoto, S. Nagasawa, H. Yamamoto, and T. Higuchi. Electrostatic tactile display with thin film slider and its application to tactile telepresentation systems. *Visualization and Computer Graphics, IEEE Transactions on*, 12(2):168–177, 2006.

[87] Tatsuma Yamamoto and Yoshitake Yamamoto. Electrical properties of the epidermal stratum corneum. *Medical and biological engineering*, 14(2):151–158, 1976.

[88] Yi Yang, Yuru Zhang, Zhu Hou, ZhongYuan Chen, and B. Lemaire-Semail. Fingviewer: A new multi-touch force feedback touch screen. In *Consumer Electronics (ICCE), 2011 IEEE International Conference on*, pages 837–838, 2011.

université PARIS-SACLAY
ÉCOLE DOCTORALE
INTERFACES
Approches Interdisciplinaires : Fondements, Applications et Innovation

Titre : Retour tactile statique et dynamique utilisant le retournement temporel et l'electrovibration

Mots clefs : Interaction haptique, Retournement temporel, Retour vibrotactile localisé, Electrovibration, Contrôle de la friction

Résumé : Le retour haptique disponible dans les produits grand public est d'un intérêt limité pour les interactions tactiles, est moins efficace que l'utilisation d'un clavier physique pour la saisie de texte et reste limité à un retour tactile unique. Ce travail vise à développer un retour tactile statique et dynamique sur grande surface. Deux types de retour complémentaires ont été identifiés afin d'enrichir le retour haptique. Le retournement temporel des ondes de flexions dans les plaques, retour statique, est étudié afin de simuler des boutons et l'électrovibration, retour dynamique, est analysée afin de simuler des textures. Un modèle analytique de la résolution spatiale du retournement temporel ainsi que des règles de conception sont élaborés et utilisés pour le développement d'un nouveau prototype. Différents signaux de commande sont étudiés en terme d'amplitude et d'émissions sonores. L'effet de la force d'appui du doigt sur l'amplitude est étudiée. Le seuil de détection n'est pas influencé par la force d'appui de l'utilisateur sur l'écran. La répétition de focalisations modulées en amplitude offre la possibilité de simuler le clic d'un bouton. D'un autre côté, l'électrovibration produit des stimuli capables de donner une sensation de texture, en modifiant le coefficient de friction entre le doigt et la surface à explorer. Une étude utilisateur a été conduite dans le but de déterminer l'influence de la force d'appui sur le seuil de détection d'une stimulation par electrovibration. La combinaison des deux approches offrira un retour tactile riche et multi-point pour des boutons et des textures.

Title : Static and dynamic haptic feedback using time reversal and electrovibration stimulations

Keywords : Haptic interaction, Time reversed acoustics, Localized vibrotactile feedback, Electrovibration, Friction control

Abstract : The current haptic feedback in end user products provides limited tactile interactions, is less efficient than physical keyboards for typing activities and remain limited to a single point feedback. This work aims to develop static and dynamic haptic feedback on large surfaces. Two types of feedback with complimentary performance are identified as necessary to enrich tactile interactions. Time reversal, as a static feedback technology, is studied to simulate a button press. Electrovibration, as a dynamic feedback, is investigated to simulate tactile textures. An analytical model of the spatial resolution of time reversal as well as design guidelines are elaborated and used to develop a new time reversal enabled screen. Driving signal alternatives are investigated in terms of amplitude and noise emission. The effect of the fingertip pressure on the amplitude vibration is studied. The detection threshold is not influenced by the applied force. A repetition of impacts varying in amplitude offers the possibility to generate key-clicks. On the other hand, electrovibration stimulations are able to create a texture feedback by modifying the apparent friction coefficient between the fingertip and the surface. A user study on the influence of the applied force on the perception threshold of tactile feedback is presented. The combination of both stimulations will offer a rich multi-point tactile feedback, both for static buttons and dynamic textures.

Université Paris-Saclay
Espace Technologique / Immeuble Discovery
Route de l'Orme aux Merisiers RD 128 / 91190 Saint-Aubin, France